KU LEUVEN

ARENBERG DOCTORAL SCHOOL
FACULTY OF SCIENCE

Development of Bimodal Contrast Agents for MRI and Optical Imaging

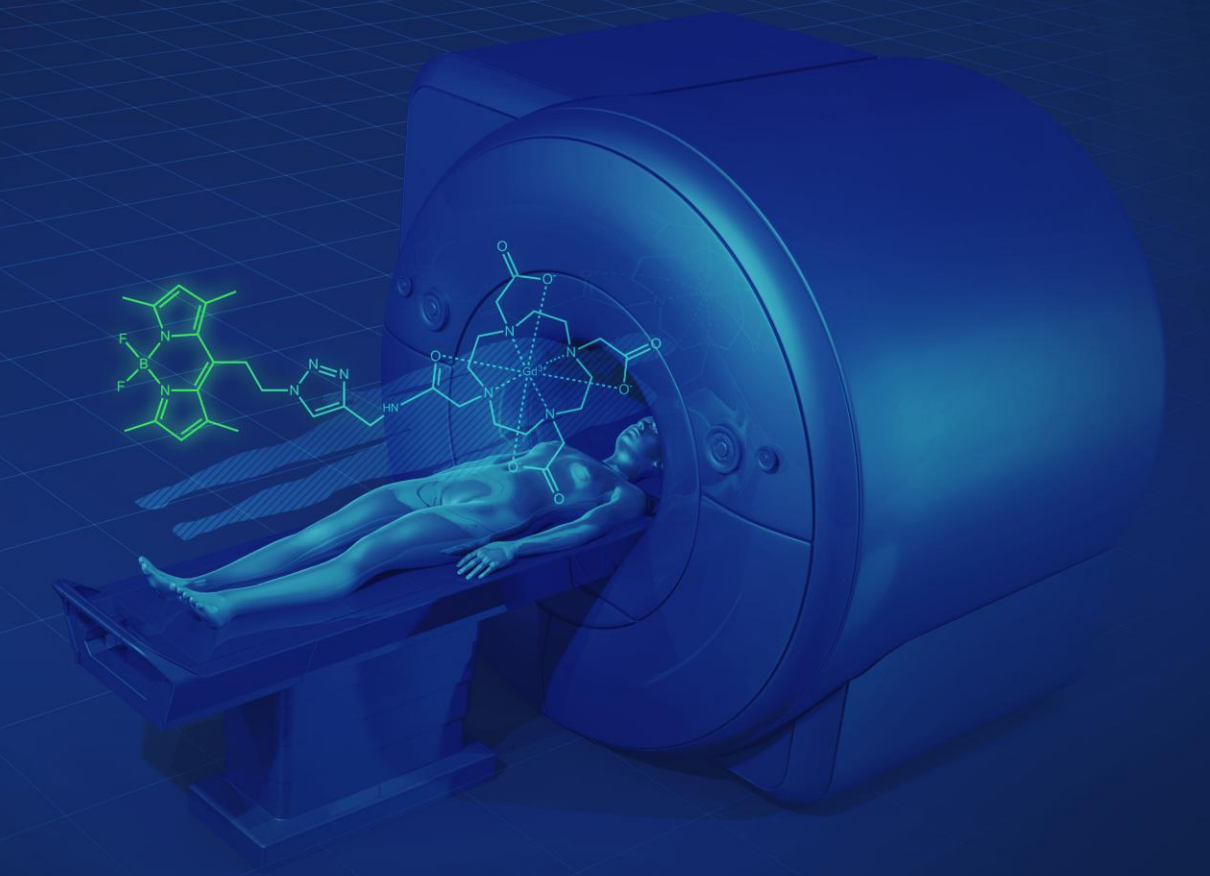

Matthias Ceulemans

January 2016

Development of Bimodal Contrast Agents for MRI and Optical Imaging

Matthias CEULEMANS

Supervisors:
Prof. Tatjana N. Parac-Vogt
Prof. Wim M. De Borggraeve

Members of the Examination Committee:
Prof. Tatjana N. Parac-Vogt
Prof. Wim M. De Borggraeve
Prof. Koen Binnemans
Prof. Wim Dehaen
Prof. Guy Koeckelberghs
Prof. Thierry Verbiest
Prof. Luce Vander Elst (Université de Mons)

Dissertation prepared in partial fulfillment of the requirements for the degree of PhD in Science

January 2016

ACKNOWLEDGEMENT

The book you're holding right now is the product of four years with a lot of successful experiments, but also many failed ones. Perseverance, persistence and the help of many people have let to this final result. I would like to take this opportunity to thank everyone who helped me mentally and/or contributed scientifically. And let's be honest, this will be the only part you are really going to read.

"Quit now and cake will be served immediately."

- GLaDOS

In the beginning I didn't know doing a PhD would be my thing. Firstly, I would like to thank my promoter, *Prof. Tatjana N. Parac-Vogt*, who convinced me during my internship that a PhD would suit me and for giving me the opportunity to embark on this interesting journey that was my PhD in the group of Laboratory of Bioinorganic Chemistry. Furthermore, I would like to thank her for the scientific input and many discussions about the results.

Secondly, I would like to thank my co-promoter *Prof. Wim M. De Borggraeve*, whose door was always open when I needed any help whenever I got stuck during my synthetic work or discuss some strange results. I would also like to thank my assessors *Prof. Koen Binnemans* and *Prof. Wim Dehaen* for providing me with extra insight during the course of my PhD.

Thirdly, I would like to thank all the members of the jury, *Prof. Koen Binnemans, Prof. Wim Dehaen, Prof. Guy Koeckelberghs, Prof. Luce Vander Elst, Prof. Thierry Verbiest, Prof. Wim M. De Borggraeve* and *Prof. Tatjana N. Parac-Vogt*, who took the time out of their busy schedules to read this dissertation and provide me with comments and remarks, greatly improving this work. I would like to

thank *Prof. Luce Vander Elst* for the nice collaboration and providing me with the important relaxometric data.

I would like to thank *Koen Nuyts* and *Maarten Bloemen* with whom very fruitful collaborations were done. I had a great time working with you two. Furthermore I would like to thank *Miguel*, my Spanish Erasmus student, who delivered some nice results. I would also like to thank the people "behind the scene": *Rita*, who kept everything running financially and administratively. *Dirk* and *Paul* who kept a steady supply of chemicals running for me to squander in my quest for results.

A PhD in Chemistry does not only consist of lab work. The past four years have been an extraordinary and fascinating experience both scientifically and personally. I was lucky to end up in a happy bunch, used to be called COC. *Aan de oude garde*, thank you for showing me the ropes on working in a lab, but especially teaching me the party side after work. I would like to thank my lab-buddy *Elke Debroye* in particular. *Elke*, dank u dat je mijn mentor was tijdens mijn masterthesis, waarbij ik altijd terecht kon voor eens goed te lachen of de broodnodige babbel. Mijn bureaucompanion, *Sophie Claxon*, dank u voor de stille momenten te doorbreken tijdens die vijf jaar dat ik een bureau met je deelde. I would like to thank my newer office mates, *Michael* and *Biju*, who have tipped the testosterone balance. *Stef, QT* en *Vinnie* waarbij menig koffiepauzes eindigden in buldergelach waarna we haast elke keer een verontschuldiging tegenover Laura tegoed hadden. Dank u *Laura* om onze humor te willen aanhoren en ze te leren verdragen. Ook een bedankje aan *Sapke*, die dit buldergelach ook heeft moeten accepteren. I would also like to thank *Giang* and *Kim Nga* for the nice talks in the office. To my friends down the hall, *Sniekers, Sven* and the rest of *LIC*, who kept a nice atmosphere during our lunch breaks and for the fun lab activities.

Dan zijn er nog mijn studiegenoten die mijn studententijd geweldig maakten. De leuke mensen van de allerbeste lolploeg *Mercury*, waarmee ik super fijne evenementen heb mogen organiseren. *Bart, Lybaert, Jeffrey en Birte* die zo gastvrij zijn en waar ik vaak mocht plaatsnemen in de rode zetel. *Berny, Sofie, Griet* en - partner in crime - *Vinnie* wil ik bedanken voor de verschillende mooie

momenten in binnen- en buitenland en de vele (al dan niet zelfbereide) gerechten. *Jan* en *Lotte*, met de noemenswaardige Nieuwjaar waar we het epische gerecht Turducken serveerde. *Dr. Eez* en *Kaat* die na een lekker avondmaal nog bereid zijn om gezelschapspelen te spelen.

Ook een bedankje voor de mensen die ervoor zorgen dat mijn weekends goed gevuld blijven. *Ben, Gesso* en *Noyen*, bedankt voor de vele "filosofische" gesprekken in de vele "literaire café's" zoals de stille genieter, of de verre reizen die voor altijd in mijn geheugen staan gegrift. Nog een extra bedankje aan de Codeur *Ben*, die de fantastische cover van mijn thesis heeft ontworpen. Verder zijn er nog *Dries, Niels* en *Pieter* voor de vele leuke avonden. De mensen van *nsa* waar ik me uren mee kan amuseren zowel online als offline. Ook aan de mensen die ik vergeten ben te vernomen een dankjewel.

"*The cake is a lie*"

- The internet

Verder zou ik nog enkele belangrijke personen willen bedanken in mijn leven: mijn ouders *Monique* en *Marc*. Mama, papa, ik zeg het veel te weinig, maar dank u voor alle steun die jullie mij geven. De vele trips van en naar Leuven, het altijd geïnteresseerd zijn in mijn studies en het werk, en zoveel meer. Ook zou ik nog mijn broer *Maxim* willen bedanken die samen met *Silke* een super duo vormt.

Tenslotte wil ik mijn vriendin *Charlotte* nog bedanken om mijn thesis na te lezen en te verbeteren. Graag ga ik met je op pad om Sven te "dwarsbomen". Dank u om mijn (soms) kort temperament te verdragen, met mij opgezadeld te willen zitten en me dagelijks op te vrolijken. Of met die zuchtende "Oh schat", een glimlach op mijn gezicht te toveren als ik weer wat stoms heb gezegd. Om me af en toe die spreekwoordelijke, maar broodnodige schop onder mijn kont te geven door te zeggen: "zou je niet beter wat schrijven?". Kortom, je bent geweldig!

TABLE OF CONTENTS

ABSTRACT

Magnetic resonance imaging is a viable medical imaging tool with a very good spatial resolution, but with a relatively low sensitivity. By coupling MRI to another very sensitive technique such as optical imaging, complementary information could be obtained. This manuscript covers the development of different multimodal contrast agents for the use in optical and magnetic resonance imaging.

In a first approach to develop these bimodal contrast agents, the synthesis and characterization of two DTPA based heteropolymetallic lanthanide metallostar complexes with the general formula $(GdL^1)_3Ln$, $(GdL^2)_3Ln$ and $(GdL^3)_3Ln$ are described. The synthesis uses a novel synthetic approach, recently developed in our group, towards the selective incorporation of gadolinium(III) and a luminescent lanthanide ion into a bitopic ligand, resulting into a highly paramagnetic and luminescent metallostar complex. Due to the higher excited state of L^1, a better sensitization was observed in all $(GdL^1)_3Ln$ complexes as compared to $(GdL^2)_3Ln$. A large increase of the quantum yield from 1.5% to 9.8% was observed for the $(GdL^1)_3Eu$ complex compared to $(GdL^2)_3Eu$, while the $(GdL^1)_3Tb$ complex exhibited a quantum yield of 30.9%, compared to 15.3% observed for $(GdL^2)_3Tb$. A slight increase of the quantum yield from 0.8% to 1.2% was observed for the Dy(III) complex when switching from ligand L^2 to L^1. The NMRD measurements of the $(GdL^2)_3Ln$ complexes (Eu(III), Dy(III), Tb(III)) showed longitudinal relaxivity values r_1 of 24.27, 22.80 and 21.72 $s^{-1}mM^{-1}$ respectively per metallostar complex at 310 K and 20 MHz.

In a second approach small monodisperse multimodal iron oxide nanoparticles were functionalized with three novel boron-dipyrromethene (BODIPY) derivatives, which are covalently attached to the nanoparticles surface *via* thiolene

click chemistry. Luminescent properties and cell viability studies of the nanoparticles have been evaluated. Bright fluorescence at 538, 594 and 661 nm is observed for nanoparticles with BDP1, BDP2 and BDP3 respectively. Cell viability studies on rat tumor (AR42J) and human ovarian cancer (SKOV3) cells showed no significant cytotoxicity up to a concentration of 200 µg/ml. Human hepatic stellate (GRX) cells were only significantly affected by the NPs at the highest concentrations.

In a third approach a novel gadolinium(III) DOTA complex functionalized with a BODIPY dye obtained *via* copper mediated cycloaddition is reported. The assembly of the complex relies on azide diazotransfer chemistry in a copper tube flow reactor. The azide thus formed is coupled directly with an alkyne *via* copper mediated cycloaddition, resulting into a paramagnetic and luminescent gadolinium(III) complex. The complex displays a bright emission at 523 nm with an absorption maximum of 507 nm with a high quantum yield of 83% in water. The proton relaxivity of the complex measured at 310 K and at frequencies of 20 and 60 MHz had the values of 3.9 and 3.6 $s^{-1}mM^{-1}$, respectively.

In a last approach peptide chemistry is used to synthesize a novel DOTA-BODIPY derivative. Unfortunately, a final complex could not be obtained, as the BODIPY core was destroyed during a deprotection step. The synthesis and characterization of two La-DOTA chelates with BODIPY derivatives, La-DOTA-BDP4 and La-DOTA-BDP5, is also highlighted. The azide containing BODIPY derivatives are reproduced from literature and coupled to a La-DOTA complex *via* copper mediated cycloaddition. The resulting complexes are water-soluble and exhibit good fluorescent properties. Upon ligand excitation a bright emission in water was observed at 508 and 510 nm with quantum yields of 39% and 64% for La-DOTA-BDP4 and La-DOTA-BDP5 respectively. Gadolinium(III) containing derivatives should be synthesized to measure the relaxometric properties. Due to the similar size, it is expected that the relaxivity of these compounds will be in the range of previously reported values for Gd-DOTA complexes.

SAMENVATTING

Magnetic Resonance Imaging is de laatste drie decennia een gevestigde waarde in de medische beeldvorming en diagnostiek geworden door zijn hoge resolutie en contrast. De relatief lage gevoeligheid is echter een groot nadeel. Het is mogelijk om complementaire informatie te bekomen wanneer MRI wordt gekoppeld met een veel gevoeligere techniek zoals optische beeldvorming. In deze verhandeling worden nieuwe multimodale contrast reagentia voor optische beeldvorming en beeldvorming door magnetische resonantie.

Ten eerste worden de synthese en karakterisatie van twee DTPA gebaseerde heteropolymetallische *metallostar*-complexen toegelicht met de algemene formules $(GdL^1)_3Ln$, $(GdL^2)_3Ln$ en $(GdL^3)_3Ln$. De synthese maakt gebruik van een recent ontwikkelde methode binnen onze groep om twee verschillende lanthanide(III)-ionen in een ditopisch ligand te complexeren. Hierbij zullen zowel gadolinium(III)-ionen, die nodig zijn voor het MRI contrast, en luminescerende lanthanide(III)-ionen worden gebruikt, met als resultaat een sterk paramagnetisch en luminescerend complex. Door de hogere energie van de aangeslagen toestand van L^1 is dit ligand beter in staat om zijn energie naar het lanthanide ion over te brengen dan L^2. Hierdoor zijn er lagere kwantumopbrengsten voor $(GdL^2)_3Ln$ gemeten, 1.5%, 15.3%, en 0.8%, in vergelijking met de waarden voor $(GdL^1)_3Ln$ 9.8%, 30.9% en 1.2% voor respectievelijk Ln = Eu(III), Tb(III), Dy(III). NMRD metingen op het $(GdL^2)_3Ln$ (Ln = Eu(III), Tb(III), Dy(III)) vertonen respectievelijke relaxiviteitswaarden (r_1) van 24.27, 22.80 en 21.72 $s^{-1}mM^{-1}$ per *metallostar*-complex bij 310 K en 20 MHz.

In een tweede aanpak worden de oppervlaktes van kleine monodisperse ijzeroxide nanopartikels covalent gebonden met nieuwe BODIPY derivaten door middel van

thiolene click-chemie gefunctionaliseerd. De fluorescentie-eigenschappen en levensvatbaarheid van cellen van de gemaakte nanopartikels werd bestudeerd. Sterke fluorescentie in water werd gemeten bij 538, 594 en 661 nm voor ijzeroxide nanopartikels met respectievelijk BDP1, BDP2 en BDP3. Uit de levensvatbaarheidstudies op verschillende cellijnen, rattumorcellen (AR42J) en menselijke eierstokkankercellen (SKOV3), werd geen acute toxiciteit waargenomen bij de gebruikte concentraties. De menselijke levercellen (GRX) werden enkel bij de hoogste concentraties (200 µg/ml) significant aangetast.

Bij een derde aanpak werd een gadolinium(III)-DOTA complex gekoppeld aan een amino-BODIPY derivaat door middel van een cycloadditie gekatalyseerd door koper(I). Het amine wordt gesubstitueerd door een diazotransferreagens in een koperen buis door middel van een *flow*-reactie. Het gevormde azide wordt rechtstreeks gekoppeld met een alkyn aan het gadolinium(III)-DOTA in het bijzijn van natrium ascorbaat. Het resulterende complex bevat zowel een paramagnetische kern voor MRI en een sterk fluorescerende eenheid met het BODIPY-derivaat. Het gesynthetiseerde wateroplosbare complex geeft een intens emissiesignaal op 523 nm en absorptiemaximum bevindt zich bij 507 nm. De *quantum yield* in water van het complex bedraagt 83% en relaxiviteit gemeten bij 310 K geeft 3.9 en 3.6 $s^{-1}mM^{-1}$ respectievelijk bij 20 en 60 MHz.

In een laatste methode werd peptidechemie gebruikt om nieuwe DOTA-BODIPY derivaten te maken. Helaas werd het finaal product vernietigd bij het ontschermingsproces. Verder werd de synthese van twee La-DOTA chelaten met BODIPY-derivaten beschreven. De azide bevattende BODIPY-derivaten werden gereproduceerd uit de literatuur en door middel van koper(I)-gekatalyseerde cycloadditie aan La-DOTA-complex gekoppeld ter vorming van La-DOTA-BDP4 en La-DOTA-BDP5. Deze wateroplosbare complexen vertonen fluorescentie bij 508 en 510 nm respectievelijk met een kwantumopbrengst van 39% en 64%. De relaxiviteit van de complexen wordt geacht hetzelfde te zijn als overeenkomstige Gd-DOTA complexen.

LIST OF SYMBOLS AND ABBREVIATIONS

μ_B	Bohr magneton
r_1	Longitudinal water relaxation rate (= $1/T_1$)
r_2	Transverse water relaxation rate (= $1/T_2$)
r_i^{IS}	Inner sphere relaxivity
r_i^{OS}	Outer sphere relaxivity
γ_I	Nuclear gyromagnetic ratio
τ_D	Diffusional correlation time
τ_M	Water residence time
τ_R	Rotational correlation time
τ_{S0}	Electronic relaxation time
μ	Magnetic moment
η	Viscosity
ω	Larmor frequency
3D	Three Dimensional
5-ALA	5-Aminolevulinic acid
a	Molecular radius
AAZTA	6-Amino-6-methylperhydro-1,4-diazepinetetraacetic acid
ACN	Acetonitrile
$A_{MD,0}$	Einstein coefficient
B_0	External magnetic field vector
BODIPY	Boron dipyrromethene
CA	Contrast agent
Cbz	Carboxybenzyl
CCD	Charged coupled device
CM	Confocal microscopy
CN	Coordination number
CSF	Cerebrospinal fluid
CT	Computed tomography
D	Relative diffusion coefficient
DCC	N,N'-Dicyclohexylcarbodiimide
DCM	Dichloromethane

DIPEA	Diisopropyl ethyl amine
DMF	Dimethylformamide
DMPAP	2,2-Dimethoxy-2-phenylacetophenone
DOTA	1,4,7,10-tetraazacyclododecane-1,4,7,10-tetraacetic acid
DPA	Dipicolinic acid
DTPA	Diethylenetriaminepentaacetic acid
DTTA	Diethylenetriaminetetraacetic acid
EI-MS	Electron ionization mass spectrometry
ESI-MS	Electrospray ionisation mass spectrometry
EtOAc	Ethyl acetate
EtOH	Ethanol
FDA	Food and drug administration
FID	Free induction decay
FLIM	Fluorescence lifetime imaging microscopy
g	Electron g factor
HATU	1-[Bis(dimethylamino)methylene]-1H-1,2,3-triazolo[4,5-b]pyridinium 3-oxid hexafluorophosphate
HOPO	Hydroxypyridinonate
HPLC	High-performance liquid chromatography
HSA	Human serum albumin
I	Spin quantum number
IONP	Iron oxide nanoparticle
ISA	Imidazole-1-sulfonyl azide
ISA·H_2SO_4	Imidazole-1-sulfonyl azide hydrogen sulfate salt
ISC	Inter systemcrossing
Ln	Lanthanide
M	Net magnetization vector
MD	Magnetic dipole
MeOH	Methanol
MFM	Multiphoton fluorescence microscopy
MR	Magnetic resonance
MRI	Magnetic resonance imaging
NHS	N-Hydroxysuccinimide
NIR	Near infrared
NMR	Nuclear magnetic resonance
NMRD	Nuclear magnetic relaxation dispersion
NP	Nanoparticle
NSF	Nephrogenic systemic fibrosis
OCT	Optical coherence tomography

OI	Optical imaging
PET	Positron emission tomography
PMT	Photomultiplier tube
q	Hydration number
QD	Quantum dot
QY	Quantum yield
RF	Radio frequency
S	Spin quantum number
SBM	Solomon, Bloembergen, and Morgan (theory)
SPECT	Single-photon emission computed tomography
SPIO	Superparamagnetic iron oxide
T_1	Longitudinal relaxation time
T_2	Transverse relaxation time
TBTU	N,N,N′,N′-Tetramethyl-O-(benzotriazol-1-yl)uronium tetrafluoroborate
*t*Bu	*Tert*-butyl
T_E	Echo time
TFA	Trifluoroacetic acid
THF	Tetrahydrofuran
T_R	Repetition time
TXRF	Total x-ray reflection fluorescence
USPIO	Ultrasmall superparamagnetic iron oxide
UV	Ultraviolet
VIS	Visible
x-ray	Röntgen radiation

PREFACE

Most medical imaging techniques make use of specifically designed contrast agents (CAs) to optimize the recorded images. The combination of two medical imaging techniques would increase the information gained from an image but requires the development of new diagnostic modalities. This multimodal approach has already been successfully implemented in modern medical imaging. MRI excels in its spatial resolution but suffers from low sensitivity. Optical imaging (OI) on the other hand is a very sensitive technique, but lacks the tissue penetration and high spatial resolution. These techniques are especially interesting as they are both non-invasive and non-ionizing. Combination of two probes for both optical and magnetic resonance imaging into one molecule assures the same biodistribution and reduces the exposure of the body by two separate drugs. The design of the new contrast agents will incorporate an optical probe for OI and a paramagnetic centre for MRI in a single probe.

In this PhD thesis the development of new bimodal MRI contrast agents *via* different approaches is highlighted and builds further on existing, commercially used CAs. Clinically used paramagnetic chelates of gadolinium(III) act as positive contrast agents, brightening the water rich regions of the image, thus enhancing the contrast. The reverse is true for negative contrast agents. Iron oxide nanoparticles are the clinically approved contributor to the latter group. New MRI instruments tend to operate at higher magnetic field as this improves the image quality and sensitivity. Current commercially available (positive) contrast agents lose their relaxivity efficiency at these higher fields, while negative contrast agents generally operate much better. By increasing the molecular weight, the increase of relaxivity at higher magnetic field strengths can be obtained. Another important factor to take into account is the emission wavelength of the optical probe. The best resolution in a human body is obtained between 665–900 nm, the optical

window of the body. Lanthanide(III) based systems are interesting as most of the ions emit within this region. In addition, the luminescent lifetimes of these ions are very long, which improves the signal to noise ratio. A promising class of organic luminophores are Boron-DIPYrromethene (BODIPY) dyes. These are small organic molecules with generally very high extinction coefficients, fairly sharp fluorescence peaks and high quantum yields. Furthermore the emission wavelength is tuneable by adding substituents on the BODIPY core.

In this work the different approaches towards designing bimodal contrast agents are described. The first two chapters are introductory: *chapter 1* presents the magnetic resonance and optical imaging, while *chapter* 2 goes deeper into the contrast agents used for MRI and describes also the scope of the PhD thesis. The compounds described in *chapter 3* are potential bimodal positive contrast agents consisting of self-assembled metallostar complexes with an *f*-block element core and three peripheral Gd-DTPA moieties. The complexes contain aromatic organic structures which will act as an antenna for *f*-block luminescence and provides rigidity to effectively increase the rotational correlation time. In a second approach iron oxide nanoparticles (IONPs) are used as potential high field bimodal negative MRI CAs. Therefore three new BODIPY dyes are synthesized and covalently bound onto the IONPs surface. The design, fluorescent data and MRI response are highlighted in *chapter 4.* In a final approach, different BODIPY analogues are coupled to Gd-DOTA to obtain potential positive bimodal contrast agents. Different azide containing BODIPYs are synthesized and coupled *via* click chemistry. In *chapter 5* the azide formation in a copper tube *via* a diazotransfer reaction is described. With the subsequent copper-mediated cycloaddition a new potential positive contrast agent is developed and its fluorescent and relaxometric data have been examined. Other methods for BODIPY synthesis, azide formation and coupling to a DOTA moiety are presented in *chapter 6*.

CHAPTER 1

Medical Imaging

1 History of medical imaging

In late 1895, Wilhelm Conrad Roentgen experimented with a special tube and noticed a “new type of electromagnetic radiation”, now known as x-rays. This radiation could expose a film even when it was optically shielded. Not soon after, he took a picture of his wife’s hand and published the first medical image. In early 1896 the clinical use of x-rays was established and since then a wide variety of different methods of radiography has been developed. In 1972 the first computed tomography (CT) scanner was produced by Godfrey Hounsfield. This technique uses mathematical methods to reconstruct an image.

When Antoine Henri Becquerel discovered radioactivity in 1896, radionuclides were first used in cancer therapy. It was not until 1923, when George de Hevesy used radiotracers to study chemical processes. These molecules were radioactively labeled drugs that mimic biological compounds. In these early studies non-imaging radiation detectors were used and only a rough idea of the amount of radiation could be obtained. The first imaging cameras were developed in 1949. The modern Anger scintillation camera was introduced by Hal Anger in 1952 and uses a collimator, a special absorbing crystal, and a series of photomultiplier tubes (PMTs).

Not all medical imaging techniques use high energy radiation, other techniques such as ultrasonography and nuclear magnetic resonance use ultrasound or radio waves respectively. The former technique has its beginnings in World War I when navy sonar technology was being developed to detect submarines. The basic principle of ultrasonic imaging is fairly simple: a propagating wave partially reflects at the surface between different tissues. These reflections can be measured in function of time. When the velocity in these tissues is known, information about the position of the tissue is provided. Magnetic resonance imaging (MRI) is based on nuclear magnetic resonance (NMR) technique. The physical phenomenon of NMR has been reported by Bloch, Hansen, and Packard in 1946,[1,2] but the application in medical imaging was realized by Lauterbur in 1973 when he made the first NMR image.[3] P. Lauterbur and P. Mansfield received the Nobel Prize in medicine in 2003 for their discoveries concerning magnetic resonance imaging.[4,5]

2 Magnetic Resonance Imaging

Magnetic resonance imaging does not make use of high energy radiation, which might be harmful to the human body. Basically, MRI measures the magnetic property of different tissues and provides a viable tool in diagnostics of the brain, torn ligaments and different types of cancers, to name a few. About 60% of the human's body weight consists of water, and therefore the strongest MRI signal comes from water protons. The patient is put in a strong three-dimensional magnetic field, which is generated by a superconducting magnet that consists of wire coils through which a current is passed. The radio frequency (RF) coils will transmit and receive radio frequency waves into the patient's body. (Figure 1.1) To ensure superconductivity, the coils are constantly cooled in liquid helium (T = 4 K). Three smaller gradient magnets are used to generate a magnetic field gradient, so anatomical information can be obtained for every region of the human body.

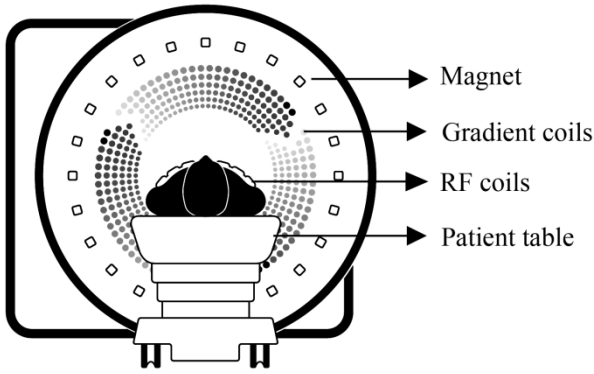

Figure 1.1. A schematic representation of the inside of an MRI scanner. The magnet with its gradient coils will ensure a gradient magnetic field around the patient. The RF coils are needed to transmit and receive radio frequency waves. †

The differences between the intensities of tissues are due to variations in water density, proton relaxation times and water diffusion rates. Cancer cells generally have a higher water density than healthy cells. Another approach is making use of faster proton relaxation rates in fat than in bulk water. The image contrast can be

increased by the use of contrast agents, paramagnetic compounds which will increase the relaxation rates. The first contrast agents made use of the paramagnetic manganese(II) ion as its chloride salt or its complex with dipyridoxyl diphosphate.[6,7] In the late 1990's two Mn(II) contrast agents were approved for medical use, but are nowadays discontinued.[8,9] The first contrast agent for medical use based on gadolinium(III) ion was approved in 1988. Nowadays Gd(III) type of probes are routinely used in MRI investigations.[10,11] Another type of existing medical contrast agent consists of superparamagnetic iron oxide nanoparticles (SPIONPs).[12]

2.1 Magnetic Resonance Imaging: theory

The next part will highlight some theoretical aspects of NMR to get an understanding on how an MRI machine works. In a first part a brief explanation of nuclear spin is presented and how it interacts with a magnetic field. Then the process of relaxivity is discussed, followed by the transformation from the signals into an image.

Atoms consist of a positively charged nucleus surrounded by one or more electrons. This positive nucleus rotates around its axis, creating a magnetic dipole with a magnetic moment (μ). The angular moment of this magnetic moment can be represented by spin vector. In quantum physics this spin angular momentum is described by a spin quantum number (I). When an external magnetic field (B_0) is applied to the nuclei, bulk magnetization is developed in the sample.

The ^{1}H atom (proton) has a natural abundance of 99.9885% and a spin quantum number of ½.Without an external field the spins are randomly oriented (Figure 1.2A) and no net magnetization is observed. Whenever these nuclei are put in a magnetic field they will align preferably towards the external magnetic field vector (B_0) and a net magnetization vector (M) along the external field is observed. In a magnetic field the spin will start to make a precessing motion around the magnetic field vector with a specific angular frequency, called the Larmor frequency (Figure 1.2B).

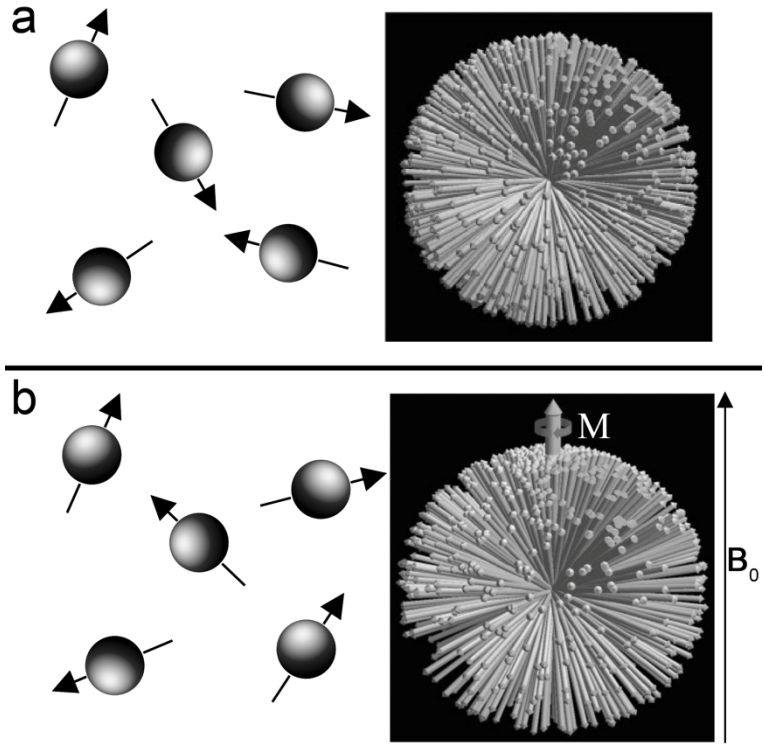

Figure 1.2. A) Proton vectors in the absence of a magnetic field are pointing in a random position. B) Proton vectors in the presence of a magnetic field B_0 have a preference to align towards the external field, forming a net magnetization vector (M) along the external field (large arrow). All spins have a precessing motion around the external magnetic field (figure based on ref 13).

When in addition to the magnetic field a 90° radio frequency pulse is applied, the net magnetization vector will be perturbed into the xy-plane and all protons will precess in phase. After the RF pulse two different processes will take place simultaneously. The longitudinal relaxation process comprises the recovery of the net magnetization vector along the direction of the external magnetic field (Figure 1.3), and the energy is released to the surroundings or the lattice. It is therefore called longitudinal or spin-lattice relaxation and is characterized by the longitudinal relaxation time (T_1). The inverse is called the relaxation rate R_1.

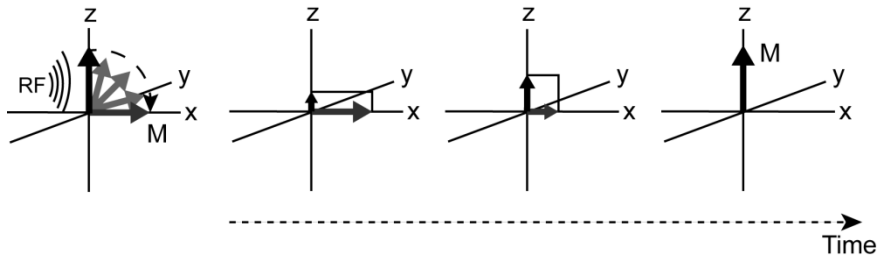

Figure 1.3. Longitudinal relaxation process: after the 90° RF pulse stops, the net magnetization vector (M) returns back along the external magnetic field (z-axis).

The transverse relaxation process describes the loss of phase coherence. In other words, the protons will no longer precess together due to small differences in Larmor frequencies (Figure 1.4). Another factor is energy exchange between two spins. No energy is lost during this transition, but dephasing of spins will take place. The exponential decay of the signal in time is called **free induction decay** (FID). The process is characterized by the transverse relaxation time (T_2) and its inverse is the transverse relaxation rate R_2.

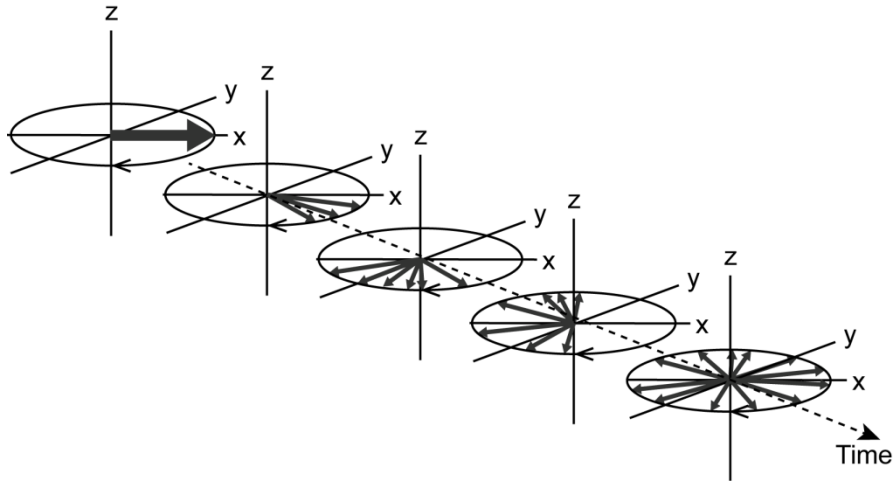

Figure 1.4. Transverse relaxation process: the different spin vectors will rotate around the z-axis in the xy-plane at different speeds due to inhomogeneities in the local magnetic field. Therefore they will start to dephase and in the end no spin vector will point in the same direction.

All contrast agents have an effect on both longitudinal and transverse relaxation processes. The effect that is influenced the most is used to classify the CAs into categories. Contrast agents containing gadolinium(III) will affect the longitudinal relaxation time (T_1) more. These CAs will increase the intensity of water containing parts of the body and are called positive contrast agents. A darkening of the image is also possible and is caused by negative contrast agents. They decrease the transverse relaxation time (T_2). Iron oxide nanoparticles are part of this category. They introduce a large inhomogeneity in the local magnetic field which increases the loss of phase coherence, and decrease the signal intensity.

2.2 Magnetic Resonance Imaging: practice

The following segment gives insight in how the signals are processed into a 3D image. We get an understanding of the spin behavior and its time dependency from the relaxation processes. A simple pulse program used in MRI is spin echo sequence (Figure 1.5). After the 90° pulse, a second 180° pulse is applied to restore the phase coherence between the spins and an echo is observed. The time between the 90° pulse and the spin echo is called the **echo time** (T_E). It is a parameter which can be altered depending on the 180° pulse. The timing will have an effect on the spin echo signal, thus the image. The time between consecutive 90° pulses is called the **repetition time** (T_R).

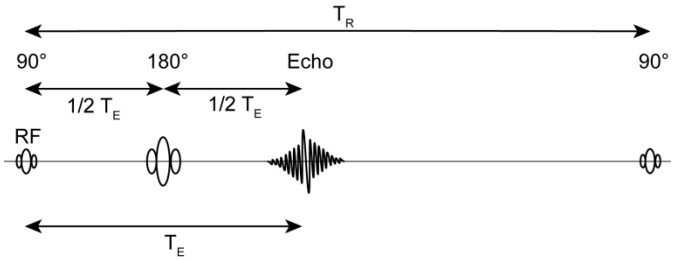

Figure 1.5. Spin echo sequence with the time between the 90° pulse and the spin echo, T_E, and the time between 90° pulses, T_R, two important parameters to obtain a 3D MRI image.[14]

By changing the parameters T_E and T_R, the MRI operator can choose three different types of images: proton density, T_1- and T_2-weighted (Figure 1.6). In general a **proton density** weighted images are obtained by a long T_R and either no

or a small T_E. It will generate an image with clear bright spots where proton rich tissues are located, because one would get a maximum signal from tissues with a minimum in transverse decay. In a **T_1-weighted** measurement both T_E and T_R will be relative small. The same reason for a short T_E applies here as well, minimizing transverse relaxivity. T_R is reasonably short to get a tissue effect. For example, take two different tissues from the brain with respectively a short and a long T_1: fat and cerebrospinal fluid (CSF). At the T_R, the net magnetization of fat will have a much higher value than CSF. Thus the contribution of M being flipped into the xy-plane of CSF at T_R is small, therefore the overall signal will be small and the image appears dark. The reverse is true for fat tissue, which will appear bright. Mostly the T_R will be chosen to be approximately the T_1 value of the tissue with the smallest T_1. The image contrast becomes dependents on the T_1 relaxation process of the tissues. **T_2-weighted** images generally have a long T_R to avoid T_1 effects, and relative long T_E to ensure dephasing. Generally, the T_E value will more or less be equal to the T_2 of the examined tissues.

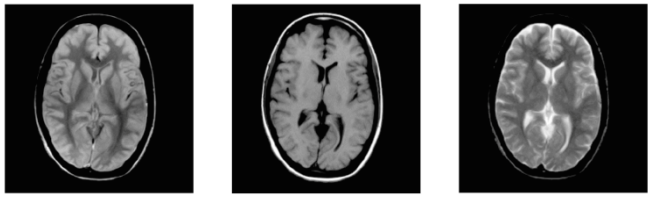

Figure 1.6. The MRI operator can choose the contrast of the different tissues observed in the image by changing the echo time (T_E) and repetition time (T_R). The different images are classified as: proton density (PD), T_1-weighted, and T_2-weighted.[14]

As mentioned above, to obtain a 3D image, MRI uses three gradient magnetic fields to give extra information to the NMR signal. The gradient along the patient's body (z-axis) is used for the **slice selection**. The other gradients are **frequency encoding** (x-axis) and **phase encoding** (y-axis) gradients which spatially separate the signals within the slice. With this information, a computer can calculate a 3D image. MRI is a very strong technique which can give

anatomical and pathological information about the whole human body as is shown in Figure 1.7.

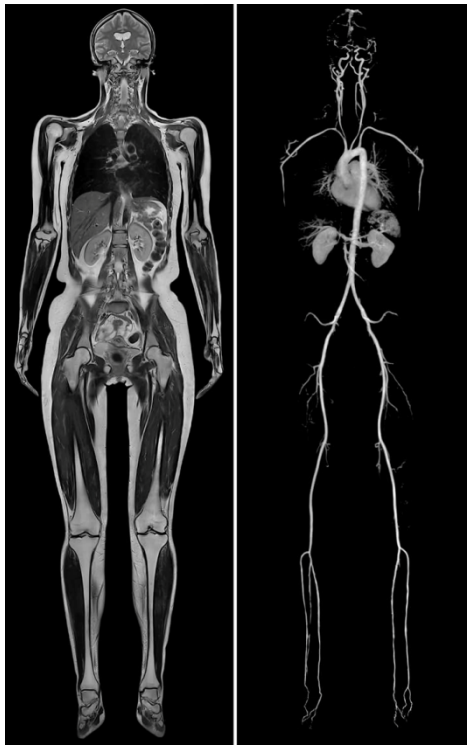

Figure 1.7. A full body MRI scan (right) and angiography (right) taken with a 3T apparatus. †

3 Optical imaging

In the last decades numerous attempts have been made to design optical imaging applications for medical diagnostics. A first attempt was done by Cutler in 1929, who illuminated a female breast with a bright light source in a darkened room. Despite attempts to improve the illumination by employing NIR sources and detectors, clinical utility remained severely limited.[15] Although the high sensitivity of the technique makes it very interesting, major drawbacks in penetration depth and image reconstruction due to scattering, reflectance, absorbance and fluorescence of photons by the biological tissues are encountered.[16] Only a few optical modalities are currently used in medicine.[17,18]

Clinical or pathological information could be obtained from tissue diagnostics while limiting the problem of tissue penetration such as “optical biopsy”. In these samples reflectance and fluorescence lifetime imaging microscopy (FLIM) can provide functional information, confocal microscopy (CM) and multiphoton fluorescence microscopy (MFM) resolves cellular morphology, optical coherence tomography (OCT) provides highly resolved cross-sectional imaging within the tissue.[19]

Fluorescence lifetime microscopy can reduce the scattering effect as it measures the lifetime of the fluorophores signal rather than the intensity. The setup consists of a pulsed diode laser and the decay is measured by a detector. FLIM is an interesting technique to use for imaging of the brain, as the brain scatters light strongly.

Optical coherence tomography works similar to echography, but the image is reconstructed from scattered light instead of ultrasound waves. Due to the shorter wavelength of light, high resolution images ($\leq$ µm) are possible. A typical setup contains a light source which illuminates a sample, usually a diode, and a detector which collects the scattered light. OCT can be compared to a microscope without the need to dissect the sample and reveals subsurface (~ mm) information. OCT finds its uses in retina malfunctions and diagnostics of nerve, vein and heart problems.

Confocal microscopy offers an improved spatial resolution compared to conventional microscopy. The light source, usually a laser, is focused at a specific point within the tissue. This focal point can be scanned by a mirror system and is imaged onto a pinhole in front of the detection system (Figure 1.8). The pinhole rejects photons originating from outside the focal plane thus improving the spatial resolution. The two main *in vivo* clinical applications are in dermatology and ophthalmology. The contrast of melanin is used to distinguish between normal and abnormal tissue. A wide range of corneal diseases can be detected using this technique.

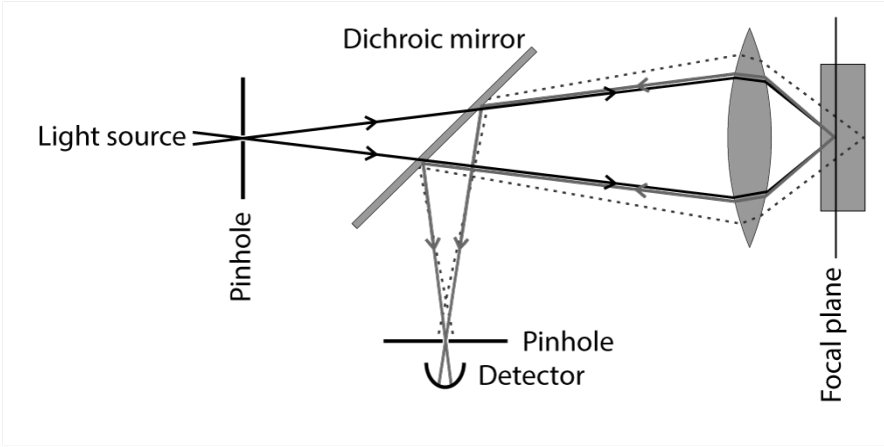

Figure 1.8. Confocal microscopy. The pinhole is scanned sideways, up and down to gather images from different focal planes resulting in a three-dimensional image of the specimen. Out-of-focus light rays are blocked to improve the spatial resolution.

Multiphoton fluorescence microscopy is similar to confocal microscopy.[20] The generated images of both techniques come from focused laser beams which scan in a raster pattern. Both have an optical sectioning effect, where a suitably designed microscope can produce images of focal planes deep within a thick sample. Unlike confocal microscopes, a multiphoton microscope does not contain pinhole apertures. It uses a pulsed long-wavelength laser to excite fluorophores within the specimen which absorb the energy from two long-wavelength photons that arrive simultaneously to excite an electron into a higher energy state. These longer wavelengths, typically in the infra-red region, are well-suited to use *in vivo* as they cause less damage and have greater penetration depths than short-wavelength lasers.

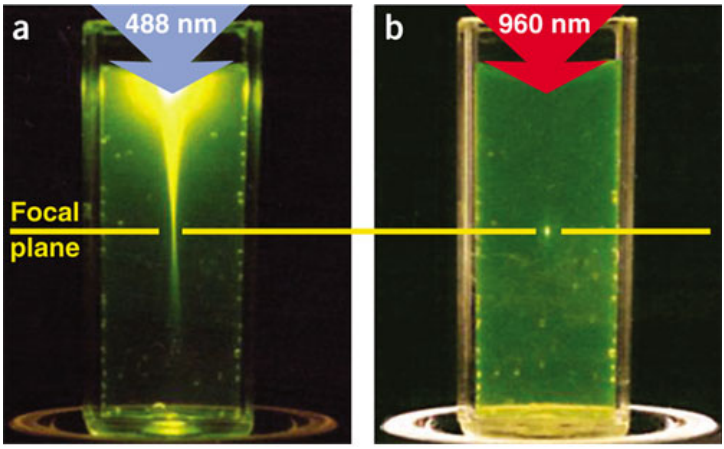

Figure 1.9. (a) Single-photon excitation of fluorescein (488 nm). (b) Two-photon excitation using focused femtosecond pulses (960 nm).[20]

Next to the mentioned techniques, optical imaging can be a viable tool during surgery. A metabolic precursor can be injected into the patient prior to surgery. 5-ALA is known to accumulate fluorescent porphyrins in malignant glioma tissues.[21] During the operation, the surgeon can switch between conventional to violet-blue illumination (Figure 1.10). Necrotic tumor displays no or only inhomogeneous red fluorescence, viable tumor tissue is distinguished by its deep red fluorescence (solid) and pink fluorescence is encountered between the fluorescent tumor and non-fluorescent blue brain tissue (vague).[22]

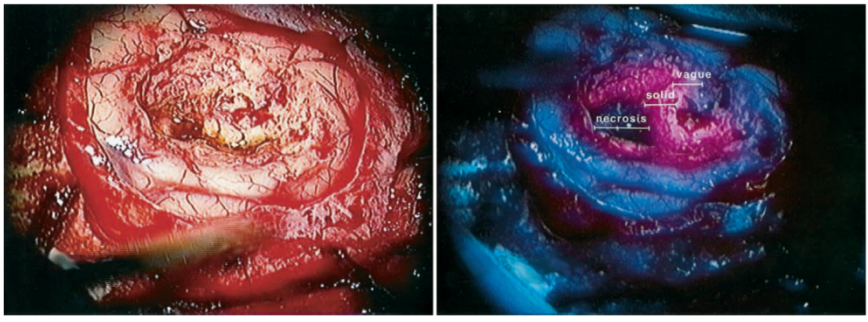

Figure 1.10. Necrotic tumor displayes no red fluorescence (necrosis), viable tumor tissue has deep red fluorescence (solid) and between fluorescent tumor and non-fluorescent blue brain tissue a pink fluorescence was encountered (vague).[22]

4 References

(1) Bloch, F. *Phys. Rev.* **1946**, *70* (7-8), 460–474.
(2) Bloch, F.; Hansen, W. W.; Packard, M. *Phys. Rev.* **1946**, *70* (7-8), 474–485.
(3) Lauterbur, P. C. *Nature* **1973**, *242* (5394), 190–191.
(4) Suetens, P. *Fundamentals of Medical Imaging, 2nd Edition*; Cambridge University Press: Cambridge, 2009.
(5) Prince, J. L.; Links, J. M. *Medical Imaging Signals and Systems*; Pearson Prentice Hall: Old Tappan, 2014.
(6) Goldman, M. R.; Brady, T. J.; Pykett, I. L.; Burt, C. T.; Buonanno, F. S.; Kistler, J. P.; Newhouse, J. H.; Hinshaw, W. S.; Pohost, G. M. *Circulation* **1982**, *66* (5), 1012–1016.
(7) Pan, D.; Schmieder, A. H.; Wickline, S. A.; Lanza, G. M. *Tetrahedron* **2011**, *67* (44), 8431–8444.
(8) European Medicines Agency. Find Medicine - Teslascan http://www.ema.europa.eu/ema/index.jsp?curl=pages/medicines/human/medicines/000137/human_med_001088.jsp&mid=WC0b01ac058001d124 (accessed Sep 8, 2015).
(9) Drugs@FDA. FDA Approved Drug Products - LumenHance http://www.accessdata.fda.gov/scripts/cder/drugsatfda/index.cfm?fuseaction=Search.DrugDetails (accessed Sep 8, 2015).
(10) Caravan, P.; Ellison, J. J.; McMurry, T. J.; Lauffer, R. B. *Chem. Rev.* **1999**, *99* (9), 2293–2352.
(11) Caravan, P. *Chem. Soc. Rev.* **2006**, *35* (6), 512.
(12) Laurent, S.; Forge, D.; Port, M.; Roch, A.; Robic, C.; Vander Elst, L.; Muller, R. N. *Chem. Rev.* **2008**, *108* (6), 2064–2110.
(13) Hanson, L. G. *Concepts Magn. Reson. Part A* **2008**, *32A* (5), 329–340.
(14) Blink, E. J. Basic MRI Physics http://www.mri-physics.net.
(15) Hebden, J. C.; Arridge, S. R.; Delpy, D. T. *Phys. Med. Biol.* **1997**, *42* (5), 825–840.
(16) Brovko, L. *Bioluminescence and Fluorescence for In Vivo Imaging*; SPIE Press: Bellingham, 2010.
(17) Merali, Z. *Nature* **2015**, *518* (7538), 158–160.
(18) Johansson, H.; Pedersen, D. S. *European J. Org. Chem.* **2012**, *2012* (23), 4267–4281.
(19) Johansson, A.; Kromer, K.; Sroka, R.; Stepp, H. *Med. Laser Appl.* **2008**, *23* (4), 155–174.
(20) Zipfel, W. R.; Williams, R. M.; Webb, W. W. *Nat. Biotechnol.* **2003**, *21* (11), 1369–1377.
(21) Stummer, W.; Stocker, S.; Wagner, S.; Stepp, H.; Fritsch, C.; Goetz, C.; Goetz, A. E.; Kiefmann, R.; Reulen, H. J. *Neurosurgery* **1998**, *42* (3), 518–526.
(22) Stummer, W.; Novotny, A.; Stepp, H.; Goetz, C.; Bise, K.; Reulen, H. J. *J. Neurosurg.* **2000**, *93* (6), 1003–1013.

† Illustrations courtesy of Siemens Healthcare GmbH and can be found in their product brochures of MAGNETOM series MRI instruments or their website: http://www.healthcare.siemens.com/magnetic-resonance-imaging

CHAPTER 2

Contrast Agents for Magnetic Resonance Imaging

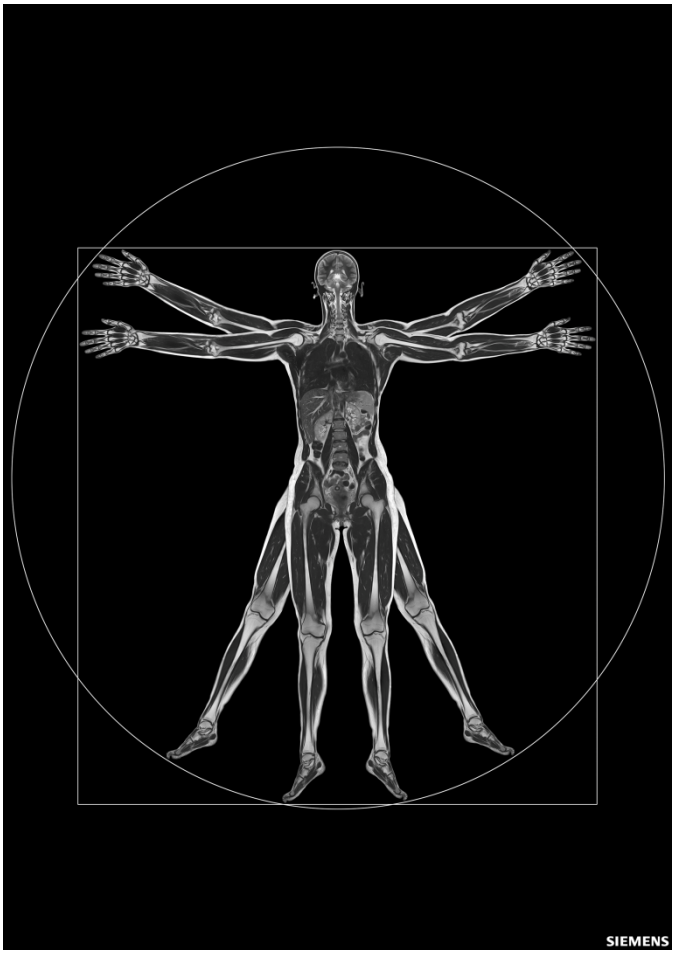

1 Relaxivity

As MRI is based on proton relaxation, an important attribute of all contrast agents is its *relaxivity*. Relaxivity is defined as the ability of a 1 mM concentration of a contrast agent (CA) to enhance the water relaxation rate. Already in the middle of the twentieth century the physical phenomenon of relaxivity was explored, leading to the Solomon, Bloembergen, and Morgan (SBM) theory.[1–4]

Both the longitudinal ($1/T_1$) and transverse ($1/T_2$) relaxation rates increase when introducing a paramagnetic nucleus to a solvent. The observed relaxation rate ($1/T_{i,obs}$) is defined as the sum of a diamagnetic term ($1/T_{i,d}$), corresponding to the relaxation rate of the solvent in absence of a paramagnetic centre, and a paramagnetic term ($1/T_{i,p}$), which is the enhancement of the relaxation rate caused by the paramagnetic centre:[5]

$$\frac{1}{T_{i,obs}} = \frac{1}{T_{i,d}} + \frac{1}{T_{i,p}} \qquad (i = 1, 2) \qquad \text{(eq. 2.1)}$$

The paramagnetic contribution is linearly proportional to the concentration of the added contrast agent (in [Gd]). Substitution in eq. 2.1 gives:

$$\frac{1}{T_{i,obs}} = \frac{1}{T_{i,d}} + r_i[Gd] \qquad (i = 1, 2) \qquad \text{(eq. 2.2)}$$

The parameter r_i is called the proton relaxivity expressed in its unity $s^{-1}mM^{-1}$. It is a factor referring to the efficiency of a contrast agent to enhance the relaxation rate of water molecules.

A dipole-dipole interaction between the proton spins and the fluctuating local field caused by the unpaired electrons of the Gd(III) is the source of the enhanced water proton relaxation. The paramagnetic enhancement can be split into two main contributors. The first type is inner sphere contribution, resulting from water molecules bound in the first coordination sphere of the gadolinium(III) centre which are in constant exchange with the bulk solvent molecules. A second type is the outer sphere contribution which is due to random translational diffusion of the

bulk water molecules that will experience a paramagnetic effect. Water molecules bound *via* a hydrogen bond are taken into account as second sphere effects.[6] The total paramagnetic relaxation can be described by eq. 2.3, or expressed in term of relaxivities by eq. 2.4.

$$\frac{1}{T_{i,p}} = \left(\frac{1}{T_{i,p}}\right)^{IS} + \left(\frac{1}{T_{i,p}}\right)^{OS} \qquad (i = 1, 2) \qquad \text{(eq. 2.3)}$$

$$r_i = r_i^{IS} + r_i^{OS} \qquad (i = 1, 2) \qquad \text{(eq. 2.4)}$$

The design of new contrast agents mainly focuses on alteration of the inner sphere longitudinal relaxivity, as they are well studied and more easily altered than the outer sphere parameters.

2 Inner sphere proton relaxivity

The longitudinal relaxation rate of the bulk solvent nuclei is given by eq. 2.5:[7]

$$\left(\frac{1}{T_1}\right)^{IS} = \frac{q \times P_m}{T_{1m} + \tau_M} \qquad \text{(eq. 2.5)}$$

Where q is the amount of water molecules bound directly to the paramagnetic centre, P_m the mole fraction of bound solvent molecules, $1/T_{1m}$ the relaxation rate of the coordinated water molecule and τ_M the residence time ($= 1/k_{ex}$) of solvent molecules in the complex. If the water exchange is fast ($\tau_M << T_{1m}$), the enhancement of relaxivity is proportional to the relaxation rate of the bound nuclei.[8]

According to the modified Solomon-Bloembergen equations, the relaxation mechanism of the inner sphere molecules can be subdivided in a dipole-dipole (DD) and a scalar (SC) mechanism:

$$\frac{1}{T_{i,p}} = \frac{1}{T_i^{DD}} + \frac{1}{T_i^{SC}} \qquad (i = 1, 2) \qquad \text{(eq. 2.6)}$$

The dipole-dipole interactions are considered a 'through space' contribution and are determined by the reorientation of the nuclear spin – electron spin vector. Scalar interactions are considered 'through bound' contributions and only depend on the electron spin relaxation and the water exchange rate. As the contribution of the scalar term is considerable smaller (~ 6 times) than the dipole-dipole interactions, this term is mostly neglected in the optimization of the relaxivity. The dipole-dipole term can be considered:

$$\frac{1}{T_i^{DD}} = \frac{2}{15}\frac{\gamma_I^2 g^2 \mu_B^2 S(S+1)}{r^6}\left(\frac{3\tau_{c1}}{1+\omega_I^2\tau_{c1}^2} + \frac{7\tau_{c2}}{1+\omega_S^2\tau_{c2}^2}\right) \qquad \text{(eq. 2.7)}$$

where γ_I is the nuclear gyromagnetic ratio (42.57 MHz/T for ^{1}H), g is the electron g factor, μ_B is the Bohr magneton, S is the spin quantum number (S=7/2 for Gd^{3+}), r is the distance between the paramagnetic centre and the coordinated water molecules, ω_I and ω_S the nuclear and electron Larmor frequencies respectively, and τ_{ci} the dipole-dipole correlation times. From eq. 2.7 it is clear that the distance to the paramagnetic centre has a large impact on the proton relaxation. The correlation times τ_{ci} are characteristic for the relaxation process and are depicted as:

$$\frac{1}{\tau_{ci}} = \frac{1}{\tau_R} + \frac{1}{\tau_M} + \frac{1}{T_{ie}} \qquad (i = 1, 2) \qquad \text{(eq. 2.8)}$$

where τ_R is the rotational correlation time, or more precisely, the reorientation correlation time of the metal to proton vector. The τ_M is the residence time of the water molecules bound to the paramagnetic centre, and T_{ie} is the electron spin relaxation of the metal ion.

The important factors for a good ligand design are depicted in Figure 2.1. From eq. 2.5 it is shown that if the overall correlation time τ_{ci} increases, the longitudinal relaxation time ($1/T_1$) will be enhanced. If the residence time of the water molecules is rather long ($T_{1m} << \tau_M$), this parameter will be the limiting factor for proton relaxivity. In the reverse case ($\tau_M << T_{1m}$), the overall correlation time will depend on the relaxation rate of the coordinated water molecules (T_{1m}), which is

determined by τ_R, τ_M, and T_{ie}. The challenge in order to obtain the highest relaxivity is that all factors, τ_R, τ_M, and T_{ie}, must be simultaneously optimized.

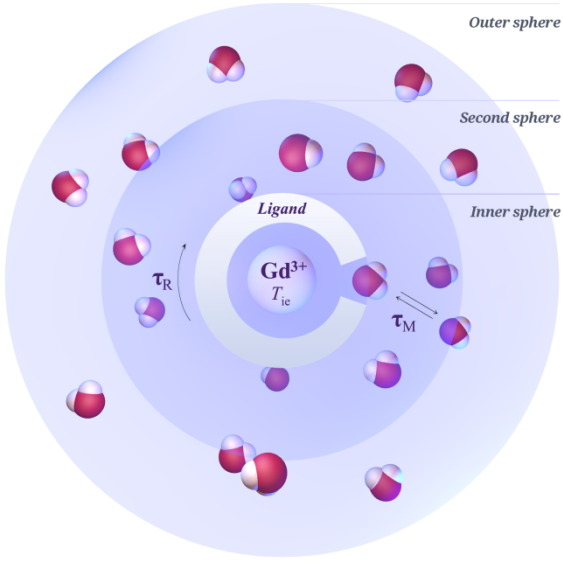

Figure 2.1. Schematic representation of the different physical parameters influencing the relaxation efficiency of MRI contrast agents.

2.1 Positive contrast agents

The positive contrast agents are mainly governed by gadolinium containing chelates. Gadolinium is a chemical element with atomic number 64 and part of the lanthanide series in the periodic table of the elements. The lanthanide series have high coordination numbers (CN), descending from ten or nine for the light ions, to eight or seven for the heavy trivalent metal ions. Gadolinium has a CN = 8-9, adopts the +3 oxidation state, has seven unpaired electrons and a large magnetic moment (7.94 μB). Gadolinium(III) has relatively long electron relaxation times due to its symmetric $^8S_{7/2}$ ground state.[5] Free gadolinium(III) ions are toxic to living animals (LD_{50} = 0.2 mmol·kg^{-1} in mice[a]).[7] As the general dose of CA administered is 0.1-0.3 mmol per kg body weight, highly thermodynamically

[a] LD_{50} is a standard measurement of acute toxicity representing the individual dose required to kill 50% of a population of test animals.

stable and high kinetically inert chelates are necessary.[9] Two most commonly used ligands are the acyclic diethylenetriaminepentaacetic acid (DTPA) and the cyclic 1,4,7,10-tetraazacyclododecane-1,4,7,10-tetraacetic acid (DOTA). These ligands are eight-fold coordinated to gadolinium(III), ensuring a stable complex of log K = 22.5 and 25.3 for DTPA and DOTA respectively.[8] In the past decades, a couple of their analogues have been also approved for medical use (Figure 2.2).[10] All commercially available CAs have an 8-fold coordination with their ligand, allowing binding of one water molecule directly to the metallic centre while assuring stable complexes.

The gadolinium(III) based CAs passively distribute in the extracellular space and exhibit no specific tissue accumulation, do not penetrate the blood-brain barrier, and are completely and quickly excreted via the kidneys. Multihance® and to a lesser extend Eovist®, are taken up by the hepatocytes in the liver and excreted into the bile. This uptake allows for organ specific diagnosis of a variety of liver lesions and provides an additional excretion pathway. Ablavar® is a blood pool agent due to the strong but reversible binding to serum albumin, a common protein in the blood, which leads to a very slow but complete renal elimination.[11]

2.2 Negative contrast agents

Within the group of negative contrast agents, iron oxide NPs are the main contributor. Two groups exist: the superparamagnetic iron oxide (SPIO) and the ultrasmall superparamagnetic iron oxide (USPIO). They are superparamagnetic and induce inhomogeneities in the local magnetic field, increasing the transverse relaxation time (T_2), thus decreasing the intensity of the MR signal. The iron oxide NPs are generally coated with organic molecules, such as dextran, carboxydextran, or citrate, to increase their dispersibility and biocompatibility in solution. In the past, several iron oxide NPs were commercially and clinically investigated, including: ferumoxides (Endorem®/Feridex®), ferrumoxtran-10 (Sineram®/Combidex®), ferucarbotran (Resovist®/Cliavist®) and ferumoxsil (Lumirem®/GastroMARK®). All but the latter are currently discontinued for a variety of reasons, one of which is to many false positives.[12]

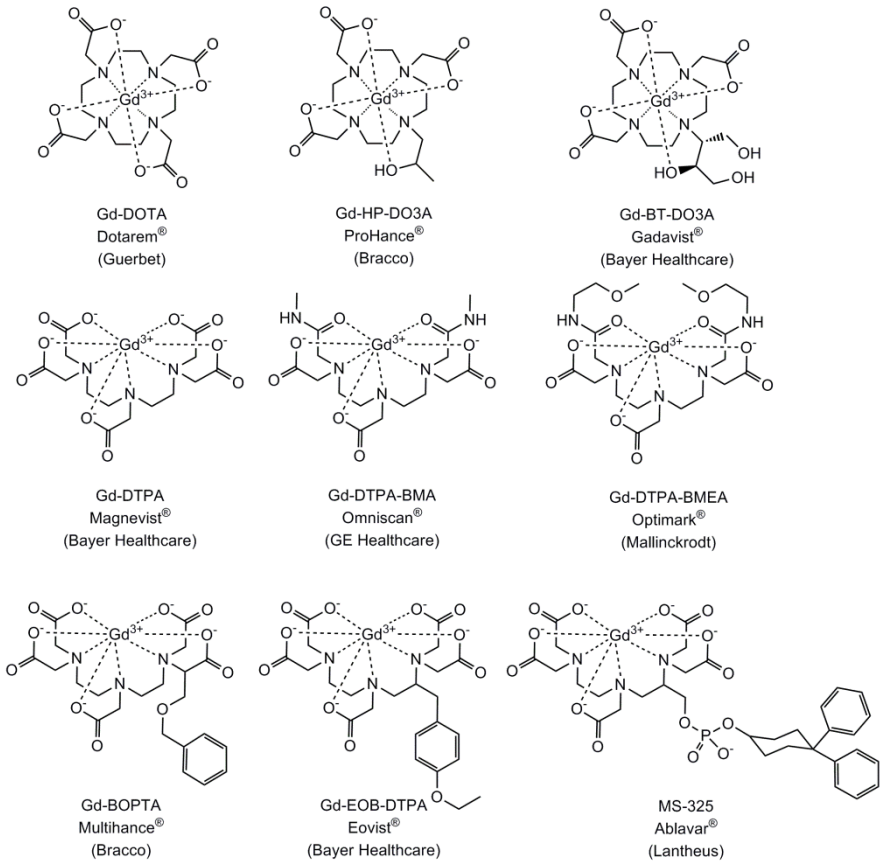

Figure 2.2. Clinically approved gadolinium(III) contrast agents. The water molecule is omitted for clarity. (figure based on ref. 8)

3 Optimization of positive contrast agents

Due to extensive research, a lot of insight is gained into the parameters governing relaxivity of contrast agents.[8,13–20] In the next part these parameters are discussed into more detail.

3.1 Hydration number, q

Increasing the amount of water molecules directly bound to the paramagnetic centre will drastically increase the overall proton relaxivity. However, all commercial contrast agents based on DTPA or DOTA have a hydration number of one (q = 1). Although removing an acetic acid arm from DOTA would free up an extra space for an additional water molecule, the thermodynamic stability of the complex will decrease by several orders.[21] Furthermore, the relaxivity is easily quenched by substitution of water by small molecules like carboxylic or amino acids, thus decreasing the efficiency of the CA.[22] The latter problem can be circumvented by using ligands such as DTTA,[23] AAZTA[24] or HOPO[25] (Figure 2.3). These ligands have the ability to form Gd(III) complexes with two water molecules in the first coordination sphere, but are less affected by small molecules in solution. Although these ligands will form thermodynamically stable chelates with gadolinium(III), they suffer from low kinetic stability. Generally, increasing hydration number is not considered a viable way to increase the relaxivity.

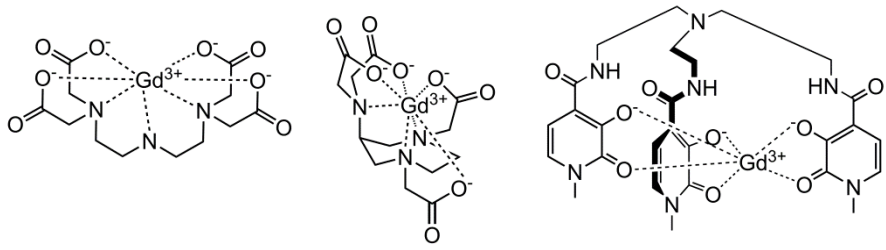

Figure 2.3. Structures of DTTA, AAZTA and HOPO ligand with a hydration number with q = 2. The water molecules are omitted for clarity.

3.2 Residence time of the water molecule, τ_M

Another important factor is the residence time of the water molecules in the complex, τ_M, as it defines the efficiency in transmitting the relaxivity to the bulk solvent. Ideally the water exchange should be fast (10-30 ns) to increase relaxivities of the contrast agents at present magnetic fields (60 MHz or 1.5 T).[26] However, at higher magnetic field strengths shorter values of τ_M are necessary (1-10 ns). The value of τ_M mainly depends on the charge, solvent accessibility, steric hindrance around the binding site, and mechanism of water exchange of the complex. Negatively charged species will force water molecules to leave and shorter τ_M (~ 50-300 ns) are obtained in comparison to neutral and positive charged species. Transformation of a carboxylic acid group of both DTPA and DOTA like ligands into an amide functionality will increase τ_M, as the amide-oxygen distance is longer and induces less sterical hindrance. Alteration of the binding side, such as adding hydrophilic or hydrophobic groups, can influence the access of bulk water molecules to the binding site and thus change τ_M.[27] For example adding a bulkier group such as phosphorus containing side arms will decrease the residence time of water.[28,29] According to the SBM theory the optimal value for τ_M is closely related to the rotational correlation time τ_R.

3.3 Rotational correlation time, τ_R

The molecular tumbling rate or rotational correlation time τ_R is the easiest parameter to adjust and this approach is applied in most cases to increase the relaxivity, especially at higher magnetic field strengths. For spherical particles an idea of the rotational correlation time can be given by the Debye-Stokes equation:

$$\tau_R = \frac{4\pi\eta a^3}{3k_bT} \qquad \text{(eq. 2.9)}$$

From eq. 2.9 it is clear that if the molecular radius *a* and the viscosity η are known the correlation time can be calculated. τ_R of commercial contrast agents is in the range of 0.1 ns. Relaxivity of these small complexes is efficient at lower magnetic field strengths and decreases at higher magnetic field strengths. To increase the signal to noise ratio of images, novel generation of MRI instruments will likely

operate at higher magnetic fields (Figure 2.4). For such purposes new contrast agents should be developed, because commercial CAs lose their efficacy at higher fields. The different employed strategies are all conceptually the same and rely on increasing the molecular weight, thus increasing the rotational correlation time. Up to now, a lot of effort has already been done to increase this parameter.[18,19]

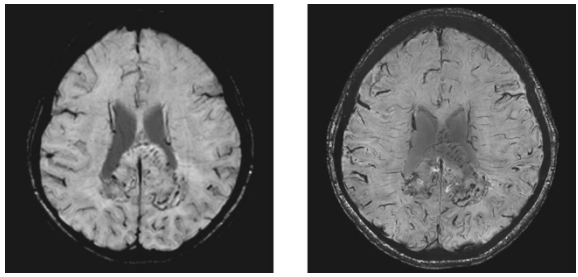

Figure 2.4. The difference between an image taken by a 3 Tesla (left) and a 7 Tesla (right) MRI apparatus. †

A first approach is **non-covalent binding to proteins**, such as the blood pool abundant human serum albumin (HSA) protein. Contrast agents for angiography, such as Ablavar®, have an apolar tail which reversibly interacts with HSA.[30–34] Several other reported CAs can interact with different types of proteins.[14,35] Blood pool contrast agents show an increased relaxivity by effectively increasing τ_R.[36]

The molecular weight of monomeric Gd(III) chelates can also be increased by **conjugation to macromolecules**. Hyperbranched polymers are well suited for the application, as the rotational dynamics is in between linear polymers (fast rotation) and star polymers (poor water accessibility).[37] Dendrimers are well-suited scaffolds for CAs with their well-defined architectures, multivalent surfaces, and nanoscale sizes. Numerous types have already been synthesized and reported.[38] Different applications can be selected when using different generations of dendrimers. In general, a size range of 3–6 nm could potentially be suitable for functional renal imaging, while those with a size range of 7–12 nm could be used for blood pool contrast enhancement.[39,40]

A third approach incorporates long alkyl chains into the CAs structure to form **micelles or liposomes**. These aggregates form due to hydrophobic interactions of

the lipid tails, while the hydrophilic parts will face towards the bulky water. To obtain monodisperse and stable structures, cholesterol or phospholipids are added. Several such structures have been successfully synthesized during the last decade.[41–43] Most recently the focus has shifted towards adding two alkyl chains to the CAs scaffold, which locks the Gd(III) chelate in place, limiting internal movement and increasing the overall relaxivity.[44–46]

High relaxivities can be obtained by increasing the amount of Gd(III) per volume, for instance by fixating the paramagnetic ion onto **nanoparticles**. Gold nanoparticles can easily be coated with thiol containing moieties, examples of 2-3 nm sized NPs with DTPA[47,48] and DTTA are known.[49] Possible CAs can be obtained by encapsulating Gd(III) ions in zeolites, such as GdNaY. Unfortunately the efficiency of these zeolites is low due to the slow diffusion of water molecules.[50] Alternatives are silica based mesoporous nanoparticles, which show relaxivities as high as 11000 $s^{-1}mM^{-1}$ per nanoparticle.[51] Another approach is ultra small nanocrystals made out of Gd_2O_3 capped with diethylene glycol for stability.[52,53]

A subtle approach to increase τ_R is the self assembly of rigid **heterometallic or metallostar complexes**.[54] This supramolecular approach has already been explored by our group. *In vivo* evaluation of a tetrametallic self-assembled complex of three phenantroline-substituted Gd-DTPA moieties present around one iron(II) ion, indicated potential enhancement in organs such as the liver.[55] A linear relationship between the relaxivity and the molecular mass of a copper metallocrown complex with a gadolinium complex derived from alpha-aminohydroxamic acid could be observed.[56]

Despite the efforts of increasing the rotational correlation time of the CA, the theoretical maximum has not yet been achieved.[13] The main cause is the local motion of gadolinium(III) chelates. Careful attention should be paid in regards to the flexibility of linker groups. By better fixation of the paramagnetic ion to the targets, the internal rotation can be reduced, for example by multilocus binding to micelles, liposomes or proteins.

3.4 Other parameters

Theoretically one could increase the relaxivity by decreasing the **distance between the bound water and the paramagnetic centre**, because of the $1/r^6$ relationship of the dipole-dipole interaction. Practically the distance for 8- to 9-coordinated Gd(III) complexes ranges between 3.0 and 3.2 Å, and is difficult to alter.[57] This distance can be measured by neutron diffraction on single crystals or by isotopic exchange.

According to eq. 2.3 the overall relaxivity is given by inner and **outer sphere contributions**. The latter arises from random movement of the bulk solvent molecules around the paramagnetic centre. When the gadolinium(III) complex and water molecules are considered as hard spheres, the interaction between the Gd(III) electron spin and the proton nuclear spins can be described as a dipolar intermolecular interaction. At the magnetic fields of interest, the outer sphere contribution depends primarily on the distance of closest approach between the paramagnetic centre and the water proton (a), and the relative diffusion coefficient of solute and solvent (D).[6] The diffusional correlation time can be expressed as $\tau_D = a^2/D$. Change of the outer sphere term is difficult as the distance of the closest approach remains the same (3.5–3.6 Å). The relative translational diffusion is set at a value close to the water diffusion rate ($\sim 3 \cdot 10^{-9}$ $m^2 s^{-1}$), which remains unchanged as well.[58] **Second sphere contributions** can be enforced by interaction of bulk water molecules to functional groups. This effect is generally not considered separately, but included in the outer sphere term.

The **electron relaxation** (T_{ie}) for gadolinium(III) complexes is a magnetic field-dependent phenomenon. Relative long relaxation times are observed for symmetric complexes such as Gd-DOTA. At low fields (< 0.1 Tesla) the electronic relaxation is fast and contributes to τ_c (eq. 2.8). The effect decreases at higher field strengths, when the rotational correlation time τ_R becomes the dominant factor. Usually the electron relaxation is not considered when designing new contrast agents.

3.5 NMRD profiles

The magnetic field dependency of the longitudinal relaxivity r_1 of a contrast agent can be determined by a technique called nuclear magnetic resonance dispersion (NMRD) and is measured by a fast field cycling NMR relaxometer. In this technique the magnetic field strength is adjusted from 0.25 mT to 1 T and the relaxivity increase is expressed as a logarithmic scale of units in Tesla or proton Larmor frequency (0.01–40 MHz). Assuming the SBM equations are valid the experimental data can be fitted to gain insight into the physicochemical parameters. The fitting of the data remains challenging as there are several parameters to be calculated simultaneously. Some of the parameters are fixed by measuring them *via* other techniques, such as τ_M, which can be estimated by ^{17}O-NMR, lifetime measurements which allows determination of the hydration number, or are based on literature values.[7] Depending on the structure, inner-, outer-, and second-sphere contributions can have large effects on the relaxivity. Only the inner- and outer-sphere are mostly considered for monomeric gadolinium(III) complexes. The relaxivity of negative contrast agents, such as SPIO and USPIO particles, only depends on outer-sphere relaxivity and are governed by different parameters.[59,60]

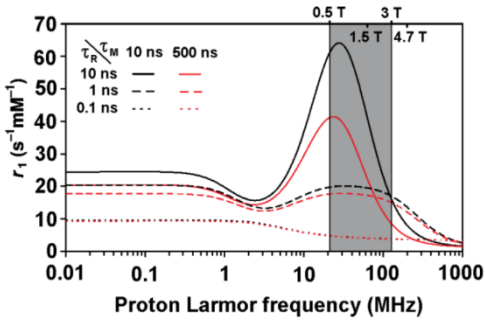

Figure 2.5. ^{1}H NMRD plot of simulations of relaxivity as a function of proton Larmor frequency. The gray area shows the range of magnetic fields currently used for medical imaging.[8]

3.6 Safety of contrast agents

A first parameter which is important when designing CAs is thermodynamical stability. The eight-fold coordination of gadolinium(III) of the commercial chelates ensure thermodynamically stable complexes, although modifications of the pendant arms can have a huge effect on this stability. Introducing two amide bonds in the DTPA scaffold (Omniscan®) results in less stable complexes (log K = 15-19).[9] As free gadolinium(III) is very toxic, high stability is necessary.

Although complexes can be very thermodynamically stable, the metal ion can still be replaced by a different metal ion, resulting in a process that is called transmetallation. A second parameter in CA safety is therefore the kinetic stability of the Gd(III) complexes, which is related to the ability to withstand transmetallation by other metal ions, foremost Cu(II) and Zn(II). These metals are present in the human blood serum in sufficiently high concentrations and are able to compete with lanthanide binding in DTPA and DOTA. To test the kinetic stability, the relaxivity of an aqueous solution of Gd(III) complex in a phosphate buffer is examined. If Gd(III) would be released, insoluble $GdPO_4$ salt will form resulting in relaxivity decrease. DOTA complexes are generally less affected by transmetallation than the acyclic DTPA derivatives.[8]

Although the contrast agents that are currently in clinical use are considered safe, in 1997 cases of nephrogenic systemic fibrosis (NSF) were found in some patients with kidney failure. This is a severe condition which forms fibrosis, formation of excess connective tissue of skin, joints, eyes, and internal organs. In 2006 the link with Gd(III)-containing CA was discovered,[61] and consequently the European Medicines Agency has issued some regulations to minimize the risk of NSF.[62]

4 Multimodal approach to contrast agents

MRI is known for its high spatial resolution and high tissue penetration. Unfortunately this technique suffers from a low sensitivity. Sensitivity and image quality could be improved by operating at higher magnetic field strengths. More information from an image can also be obtained by coupling a complementary technique to MRI. Such a viable technique could be optical imaging (OI), as this technique excels at its sensitivity and offers fairly good resolution, but suffers from low tissue penetration. A tradeoff between tissue penetration and image resolution for *in vivo* imaging can be made in the optical imaging window from 665 to 900 nm.[63] In this region the extinction coefficients of the main sources of absorption, hemoglobin, deoxyhemoglobin, and water, are at their minimum. Combining two probes into one molecule would assure the same biodistribution. Choosing the right optical probe is paramount and many fluorescent probes have already been suggested.[64] The luminescent probes vary from fluorescent macromolecules such as proteins or dendrimers, to organic dyes, fluorescent nanoparticles and d- or f-block elements.

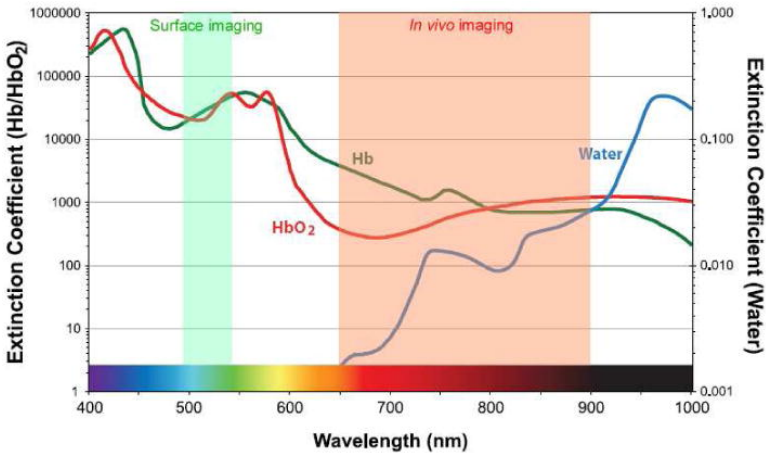

Figure 2.6. An optical window for *in vivo* imaging: an optimal tradeoff between image resolution and tissue penetration between 665 and 900 nm is found.[65]

4.1 Fluorescent macromolecules

Numerous types of fluorescent **dendrimers** have been synthesized and reported.[38,39] The tree-like dendrimers with a well-defined three-dimensional architecture have surface functional groups which can be modified with a variety of fluorescent probes enabling many different biological applications.[38] Various kinds of bright **luminescent proteins** have been developed and have been used excessively in the visualization of functional processes inside animals and plants.[66,67] Recently fluorescent NIR emitting **conjugated polymers** have been reported.[68]

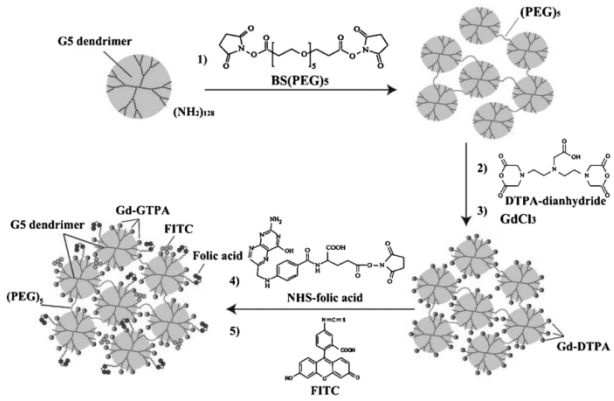

Figure 2.7. Fifth generation dendrimers are crosslinkeded with PEG chains. These dendrimeric nanoclusters are further functionalized with Gd-DTPA, fluorescent dye and folic acid.[38]

4.2 Fluorescent nanoparticles

Spherical nanosized semiconductors called **quantum dots** (QDs) are photochemical stable nanoclusters of 2–10 nm. They exhibit a narrow symmetrical fluorescence spectrum and very broad excitation spectra suitable for simultaneous multicolor detection.[69] QDs are used *in vivo* for biological and biochemical research. The main concern is their toxicity, because most QDs consist of a Cd/Se core – ZnS shell or Cd/Te core-only clusters. The cytotoxic cadmium can leak out of the nanocrystal. Potentially less toxic alternatives are InP, InGaP, $CuInS_2$ and $AgInS_2$.[70]

Upconverting NPs are inorganic nanoparticles doped with f-elements in which a continuous absorption of two low-energy photons leads to the emission of a higher-energy photon.[71] As this is a nonlinear process, the autofluorescence in bio-imaging is eliminated. The core nanoparticle could consist of a $NaGdF_4$ core doped with a small amount of Yb(III) and Tm(III) synthesized *via* thermal decomposition. Bright luminescence of 800 nm is obtained when illuminating the samples with a low intense NIR diode laser. Coating the surface with Gd(III) chelates a potential bimodal contrast agent can be formed.[72]

4.3 Organic dyes

A rather straightforward approach to develop bimodal contrast agents is the covalent attachment of organic fluorophores. Well-known groups of dyes which emit beyond 500 nm are fluoresceins, rhodamines, cyanines and 4,4-difluoro-4-bora-3a,4a-diaza-s-indacene (BODIPY).[73] These organic dyes can be altered to emit in the NIR region to obtain a better *in vivo* image quality.

The name BODIPY is derived from BOron DIPYrromethene and the first BODIPY was synthesized by Treibs and Kreuzer in 1968.[74] It was only until the 90's that the BODIPY dyes began to attract the attention of biochemists and biologists as a new candidate for fluorescence markers.

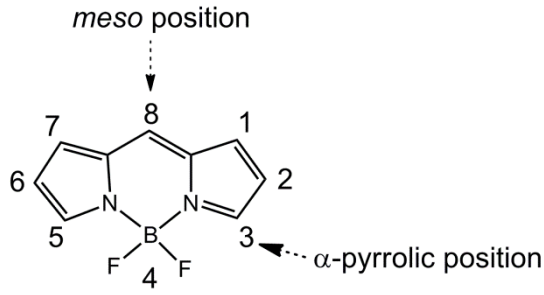

Figure 2.8. The general structure of the BODIPY-core.

The BODIPY dyes are currently used in a variety of applications such as biological labels and probes,[75–77] fluorescent probes,[78] laser dyes,[79,80] light emitting diodes,[81] solar cells,[82,83] and potential sensitizers in photodynamic

therapy.[84,85] The main characteristics of this class of organic dyes are very high extinction coefficients, fairly sharp fluorescence peaks, negligible triplet-state formation, and high quantum yields, even in water. The core is fairly stable under physiological conditions and relatively insensitive to the environment. The emission wavelength is tunable by modification of the BODIPY core.[86,87] The 8-substituted BODIPY dyes can easily be synthesized *via* condensation of acyl chlorides with pyrroles, followed by complexation with $BF_3 \cdot Et_2O$ in the presence of a base. In 2010 Bernhard *et al.* synthesized the first BODIPY-DOTA derivative to be used as a bimodal contrast agent for MRI-PET.[88] Although BODIPYs are versatile compounds with good optical properties, their use in developing bimodal contrast agents remain scarce.[88–91] The main disadvantage for biological applications is the hydrophobic nature of the BODIPY core.

4.4 Metal containing luminophores

Ditopic ligands with an affinity to transition metals can form self-assembled luminescent heteropolymetallic complexes. If one moiety is coordinated with gadolinium(III) these assemblies can be used as bimodal contrast agents for MRI and optical imaging. This approach was used by Faulkner *et al.*, [92] who reported a Gd-DOTA coupled to rhenium(I) complex emitting a red luminescence. Alternatively, Gd-DTPA with a variety of metal assemblies are known. Some examples are titanium(IV) catecholate[93] or aluminium(III) 8-hydroquinoline[94] cores for green emission. Red emission can be achieved by a ruthenium(II) 1,10-phenantroline centre (Figure 2.9).[95,96] These assemblies exhibit broad emission bands with a relative short luminescence lifetime, which is less favorable for *in vivo* imaging. A significant improvement in excited state lifetimes (milliseconds range) and sharp emission bands can be obtained by using metals of the lanthanide series. Appropriate care of the chelating ligand is necessary as the *f-f* transitions are Laporte forbidden and the luminescence must be triggered by an effect called ‘sensitization’.

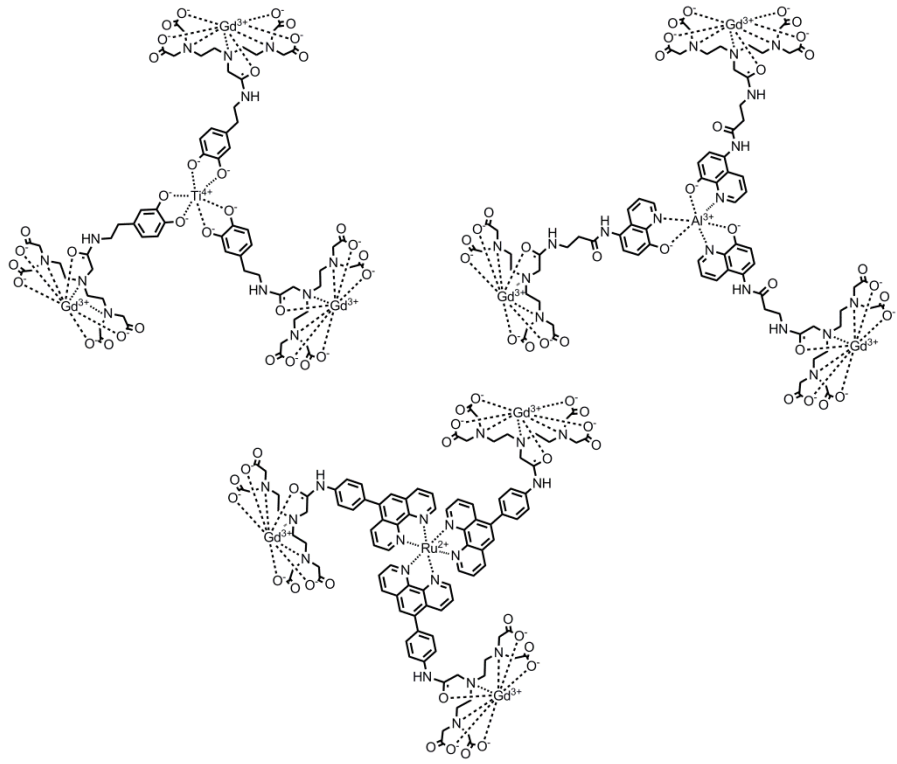

Figure 2.9. Gd(III)-DTPA with a variety of metal assemblies are known. The green emitting titanium(IV) catecholate or aluminium(III) 8-hydroquinoline cores and the red emitting ruthenium(II) 1,10-phenantroline centre.[93–95]

5 Luminescence

Upon absorption of light of a certain wavelength, a ligand or dye is excited to the singlet excited state (S_1). The captured energy can be released in the form of a photon (ligand fluorescence) or transferred into the triplet state *via* an intersystem crossing (ISC), then released as a photon (ligand phosphorescence). This mechanism is characteristic for most organic dyes. As stated above, the *f-f* transitions of lanthanide ions are Laporte forbidden. Direct excitation of the lanthanide ions is possible but they have small absorption cross-sections. To obtain good luminescence a sensitization process is necessary and is depicted in Figure 2.10A. Generally, an organic molecule with a high molecular absorption coefficient is used as an energy absorber and transfers this energy towards the lanthanide. Energy from the ligand's triplet state can be transferred to the excited state of the lanthanide where it decays to the ground state. Each transition has specific wavelengths, which are given for Eu(III) and Tb(III) in Figure 2.10B.[97] Generally, the energy transfers to the lanthanide ion are *via* the ligand triplet state, because the ISC is forced by the paramagnetic ion and the energy transfer *via* the singlet state is slower than ligand fluorescence or ISC.

The triplet-mediated energy transfer of sensitized lanthanide luminescence can proceed *via* two mechanisms: the Dexter or the Förster mechanism.[98,99] In the Dexter model the energy transfer occurs by the exchange of an electron from the sensitizing ligand to the lanthanide. Therefore orbital overlap is needed and small distances (< 10 Å) are necessary. The Förster mechanism proposes an energy transfer by donor-acceptor dipolar interactions. This happens 'through space' and relies on spectral overlap of the donor emission spectrum with the acceptor absorption spectrum. For an efficient energy transfer and subsequent luminescence, the energy levels between the sensitizer and the lanthanide ion should match.[100]

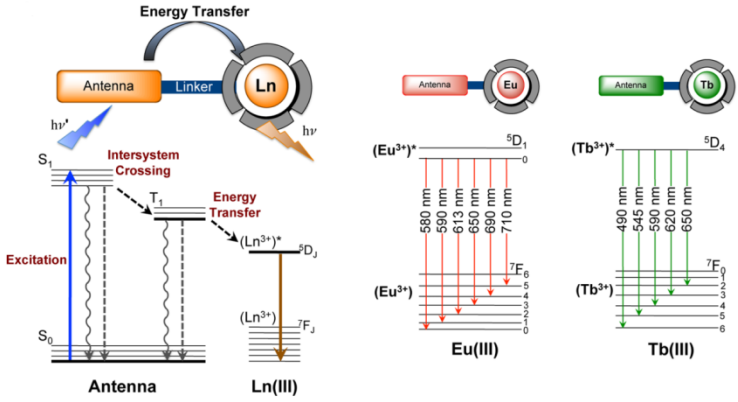

Figure 2.10. The antenna effect. (A) The antenna harvests energy through high molar absorption to the singlet excited state. After undergoing ISC to the triplet state, the antenna transfers energy to the excited state of the lanthanide. The radiative transition of the electrons from this excited state results in luminescent emission from the lanthanide ion. (B) Luminescent *4f−4f* transitions of europium(III) and terbium(III) complexes, with their commonly observed emission wavelengths of red and green light, respectively.[36]

The luminescence intensity of the lanthanides can easily be quenched by non-radiative energy dissipation *via* vibronic modes of solvent molecules.[101] This occurs in the inner coordination sphere or near the vicinity of the metal complex. The most common and very effective quencher is the O-H oscillator.[102] To maximize the emission intensity, the lanthanide should be encapsulated by strong chelates, effectively shielding it from the environment.

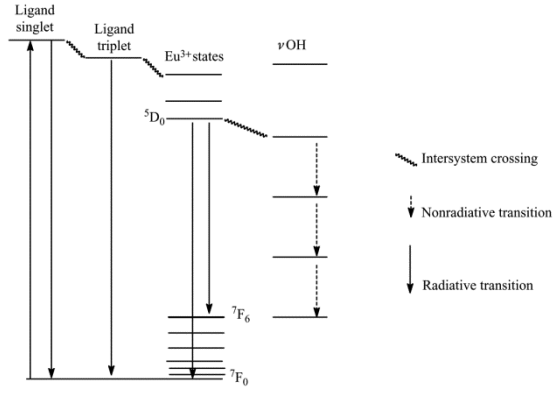

Figure 2.11. Quenching of the europium luminescence by the ν(O-H) overtones.[103]

6 Biocompatibility

In the search for new contrast agents, one needs to keep in mind the biocompatibility of the final product. As stated before, free gadolinium(III) is toxic and changes to the structure of DTPA or DOTA can alter the stability of the whole complex. Changes to the structure can also have an effect on the biodistribution and residence time in the body, although long residence times are not always considered beneficial. Targeting groups can be added to mark specific cells with a bimodal CA.

The true effect of nanoparticles in the human body has not yet been uncovered, but much research has been conducted towards a better understanding towards their biocompatibility. A prediction of biocompatibility of new NPs is frequently done by four parameters: particle size, particle surface properties, particle shape and particle structure.[104–106] For a more accurate assessment about the biocompatible behavior, *in vitro* or *in vivo* studies should be performed. The **particle size** affects the excretion and biodistribution. Large particles (> 50 nm) are excreted via the spleen and liver, while smaller particles show prolonged blood residence times. Small particles (< 50 nm) also provide a maximum in cellular uptake. Another parameter is the **surface properties** of the NPs. A positive charge has a better transvascular transport into tumors, but it could be cytotoxic and could cause an immune response. A neutral charge of NPs results in longer circulation times. A profound member in this group is the FDA approved polyethylene glycol encapsulated IONP. The layer offers increased particle dispersibility leading to a better blood-circulation and decreases the excretion rate. The **particle shape** is another parameter which can influence the biocompatibility. It has been shown that spherical shaped NPs are excreted more rapidly than their non-spherical counterparts. It is not always easy to synthesize different shapes of a particle. The last parameter influencing biocompatibility that recently was considered is the **particle structure**. Mesoporous materials offer the possibility to act as hosts for guest molecules for targeted drug delivery. More research should still be done to increase the understanding about the parameters and their effect on the biocompatibility.

7 Scope of this work

New MRI instruments tend to operate at higher magnetic field as this improves the image quality and sensitivity. Current commercially available positive contrast agents tend to lose their relaxivity efficiency at these higher fields, while negative contrast agents generally operate much better. By increasing the molecular weight, thus slowing the rotational correlation time, increased relaxivity efficiency between 20 and 100 MHz can be obtained. To further improve the performance of contrast agents, a bimodal approach could be used by combining two complementary techniques into one probe. Optical imaging has a great sensitivity, while MRI has superior spacial resolution. Lanthanide chelates offer great features such as long luminescence lifetimes and sharp emission spectra. A lot of research has been done on these types of compounds, however further studies into appropriate ligand designs and efficient lanthanide sensitization must be performed. BODIPY dyes are a group of organic molecules with tunable emission wavelengths and very bright fluorescence. The applications of these dyes are very broad, but the use as bimodal optical probe remains scarce and further optimization and its use as bimodal contrast agents should be explored.

The goal of this PhD study is the development of new multimodal contrast agents for MRI and optical imaging. In a first approach potential MRI contrast agents for higher magnetic fields are developed. The compounds are self-assembled metallostar complexes with an *f*-block element core and three peripheral Gd-DTPA moieties. The aromatic organic structure will act as an antenna for *f*-block luminescence and provides rigidity to effectively increase the rotational correlation time. The synthesis, luminescence and relaxometric properties are reported in *chapter 3*. In a second approach iron oxide nanoparticles are used as potential high field negative MRI CAs. Three new BODIPY dyes are synthesized and covalently bound onto the iron oxide NPs surface. The design, fluorescent data and MRI response is highlighted in *chapter 4*. In a final approach, different BODIPY analogues are coupled to Gd-DOTA to obtain positive bimodal contrast agents. Different azides containing BODIPYs are synthesized and coupled *via* click-chemistry. In *chapter 5* the azide formation in a copper tube *via* a

diazotransfer reaction is described. Subsequent click-reaction leads to a potential positive contrast agent which fluorescent and relaxometric data have been examined. Other methods for BODIPY synthesis and azide formation are presented in *chapter 6*.

8 References

(1) Solomon, I. *Phys. Rev.* **1955**, *99* (2), 559–565.
(2) Solomon, I.; Bloembergen, N. *J. Chem. Phys.* **1956**, *25* (2), 261.
(3) Bloembergen, N. *J. Chem. Phys.* **1957**, *27* (2), 572.
(4) Bloembergen, N.; Morgan, L. O. *J. Chem. Phys.* **1961**, *34* (3), 842.
(5) Tóth, É.; Helm, L.; Merbach, A. In *Contrast Agents I*; Krause, W., Ed.; Topics in Current Chemistry; Springer Berlin Heidelberg: Berlin, Heidelberg, 2002; Vol. 221, pp 61–101.
(6) Botta, M. *Eur. J. Inorg. Chem.* **2000**, *2000* (3), 399–407.
(7) Caravan, P.; Ellison, J. J.; McMurry, T. J.; Lauffer, R. B. *Chem. Rev.* **1999**, *99* (9), 2293–2352.
(8) Hermann, P.; Kotek, J.; Kubíček, V.; Lukeš, I. *Dalt. Trans.* **2008**, *9226* (23), 3027.
(9) Cacheris, W. P.; Quay, S. C.; Rocklage, S. M. *Magn. Reson. Imaging* **1990**, *8* (4), 467–481.
(10) Pierre, V. C.; Allen, M. J.; Caravan, P. *J. Biol. Inorg. Chem.* **2014**, *19* (2), 127–131.
(11) Rohrer, M. *Clinical Blood Pool MR Imaging*; Leiner, T., Goyen, M., Rohrer, M., Schönberg, S., Eds.; Springer Berlin Heidelberg: Berlin, Heidelberg, 2008.
(12) Wang, Y.-X. J. *Quantitative Imaging in Medicine and Surgery*. 2011, pp 35–40.
(13) Caravan, P. *Chem. Soc. Rev.* **2006**, *35* (6), 512.
(14) Caravan, P. *Acc. Chem. Res.* **2009**, *42* (7), 851–862.
(15) Louie, A. *Chem. Rev.* **2010**, *110* (5), 3146–3195.
(16) Hao, D.; Ai, T.; Goerner, F.; Hu, X.; Runge, V. M.; Tweedle, M. *J. Magn. Reson. Imaging* **2012**, *36* (5), 1060–1071.
(17) Shokrollahi, H. *Mater. Sci. Eng. C* **2013**, *33* (8), 4485–4497.
(18) Debroye, E.; Parac-Vogt, T. N. *Chem. Soc. Rev.* **2014**, *43* (23), 8178–8192.
(19) Verwilst, P.; Park, S.; Yoon, B.; Kim, J. S. *Chem. Soc. Rev.* **2015**, *44* (7), 1791–1806.
(20) Prodi, L.; Rampazzo, E.; Rastrelli, F.; Speghini, A.; Zaccheroni, N. *Chem. Soc. Rev.* **2015**, *44* (14), 4922–4952.
(21) Takács, A.; Napolitano, R.; Purgel, M.; Bényei, A. C.; Zékány, L.; Brücher, E.; Tóth, I.; Baranyai, Z.; Aime, S. *Inorg. Chem.* **2014**, *53* (6), 2858–2872.
(22) Aime, S.; Terreno, E.; Botta, M.; Bruce, J. I.; Parker, D.; Mainero, V. *Chem. Commun.* **2001**, No. 1, 115–116.
(23) Moriggi, L.; Cannizzo, C.; Prestinari, C.; Berrière, F.; Helm, L. *Inorg. Chem.* **2008**, *47* (18), 8357–8366.
(24) Artali, R.; Bombieri, G.; Giovenzana, G. B.; Galli, M.; Lattuada, L.; Meneghetti, F. *Inorganica Chim. Acta* **2013**, *407*, 306–312.
(25) Andolina, C. M.; Klemm, P. J.; Floyd, W. C.; Fréchet, J. M. J.; Raymond, K. N. *Macromolecules* **2012**, *45* (22), 8982–8990.
(26) Aime, S.; Fasano, M.; Terreno, E. *Chem. Soc. Rev.* **1998**, *27* (1), 19.
(27) Thompson, A. L.; Parker, D.; Fulton, D. A.; Howard, J. A. K.; Pandya, S.

U.; Puschmann, H.; Senanayake, K.; Stenson, P. A.; Badari, A.; Botta, M.; Avedano, S.; Aime, S. *Dalt. Trans.* **2006**, No. 47, 5605.
(28) Rudovský, J.; Cígler, P.; Kotek, J.; Hermann, P.; Vojtisek, P.; Lukeš, I.; Peters, J. A.; Vander Elst, L.; Muller, R. N. *Chem. - A Eur. J.* **2005**, *11* (8), 2373–2384.
(29) Lebdušková, P.; Kotek, J.; Hermann, P.; Vander Elst, L.; Muller, R. N.; Lukeš, I.; Peters, J. A. *Bioconjug. Chem.* **2004**, *15* (4), 881–889.
(30) Caravan, P.; Cloutier, N. J.; Greenfield, M. T.; McDermid, S. A.; Dunham, S. U.; Bulte, J. W. M.; Amedio, J. C.; Looby, R. J.; Supkowski, R. M.; Horrocks, W. D.; McMurry, T. J.; Lauffer, R. B. *J. Am. Chem. Soc.* **2002**, *124* (12), 3152–3162.
(31) Caravan, P.; Parigi, G.; Chasse, J. M.; Cloutier, N. J.; Ellison, J. J.; Lauffer, R. B.; Luchinat, C.; McDermid, S. A.; Spiller, M.; McMurry, T. J. *Inorg. Chem.* **2007**, *46* (16), 6632–6639.
(32) Parac-Vogt, T. N.; Kimpe, K.; Laurent, S.; Vander Elst, L.; Burtea, C.; Chen, F.; Muller, R. N.; Ni, Y.; Verbruggen, A.; Binnemans, K. *Chem. - A Eur. J.* **2005**, *11* (10), 3077–3086.
(33) Laurent, S.; Henoumont, C.; Vander Elst, L.; Muller, R. N. *Eur. J. Inorg. Chem.* **2012**, *2012* (12), 1889–1915.
(34) Debroye, E.; Eliseeva, S. V.; Laurent, S.; Vander Elst, L.; Petoud, S.; Muller, R. N.; Parac-Vogt, T. N. *Eur. J. Inorg. Chem.* **2013**, *2013* (14), 2629–2639.
(35) Shen, C.; New, E. J. *Curr. Opin. Chem. Biol.* **2013**, *17* (2), 158–166.
(36) Heffern, M. C.; Matosziuk, L. M.; Meade, T. J. *Chem. Rev.* **2014**, *114* (8), 4496–4539.
(37) Li, Y.; Beija, M.; Laurent, S.; Vander Elst, L.; Muller, R. N.; Duong, H. T. T.; Lowe, A. B.; Davis, T. P.; Boyer, C. *Macromolecules* **2012**, *45* (10), 4196–4204.
(38) Qiao, Z.; Shi, X. *Prog. Polym. Sci.* **2015**, *44*, 1–27.
(39) Kobayashi, H.; Kawamoto, S.; Jo, S.-K.; Bryant, H. L.; Brechbiel, M. W.; Star, R. A. *Bioconjug. Chem.* **2003**, *14* (2), 388–394.
(40) Kobayashi, H.; Brechbiel, M. *Adv. Drug Deliv. Rev.* **2005**, *57* (15), 2271–2286.
(41) Torres, S.; Martins, J. A.; André, J. P.; Geraldes, C. F. G. C.; Merbach, A. E.; Tóth, É. *Chem. - A Eur. J.* **2006**, *12* (3), 940–948.
(42) Parac-Vogt, T. N.; Kimpe, K.; Laurent, S.; Piérart, C.; Vander Elst, L.; Muller, R. N.; Binnemans, K. *Eur. Biophys. J.* **2006**, *35* (2), 136–144.
(43) Langereis, S.; Geelen, T.; Grüll, H.; Strijkers, G. J.; Nicolay, K. *NMR Biomed.* **2013**, *26* (7), 728–744.
(44) Kielar, F.; Tei, L.; Terreno, E.; Botta, M. *J. Am. Chem. Soc.* **2010**, *132* (Table 1), 7836–7837.
(45) Debroye, E.; Eliseeva, S. V.; Laurent, S.; Vander Elst, L.; Muller, R. N.; Parac-Vogt, T. N. *Dalt. Trans.* **2014**, *43* (9), 3589.
(46) Harris, M.; Carron, S.; Vander Elst, L.; Laurent, S.; Muller, R. N.; Parac-Vogt, T. N. *Chem. Commun.* **2015**, *51* (14), 2984–2986.
(47) Debouttière, P.-J.; Roux, S.; Vocanson, F.; Billotey, C.; Beuf, O.; Favre-Réguillon, A.; Lin, Y.; Pellet-Rostaing, S.; Lamartine, R.; Perriat, P.; Tillement, O. *Adv. Funct. Mater.* **2006**, *16* (18), 2330–2339.

(48) Alric, C.; Taleb, J.; Duc, G. Le; Mandon, C.; Billotey, C.; Meur-Herland, A. Le; Brochard, T.; Vocanson, F.; Janier, M.; Perriat, P.; Roux, S.; Tillement, O. *J. Am. Chem. Soc.* **2008**, *130* (18), 5908–5915.
(49) Moriggi, L.; Cannizzo, C.; Dumas, E.; Mayer, C. R.; Ulianov, A.; Helm, L. *J. Am. Chem. Soc.* **2009**, *131* (31), 10828–10829.
(50) Platas-Iglesias, C.; Vander Elst, L.; Zhou, W.; Muller, R. N.; Geraldes, C. F. G. C.; Maschmeyer, T.; Peters, J. A. *Chem. - A Eur. J.* **2002**, *8* (22), 5121–5131.
(51) Taylor, K. M. L.; Kim, J. S.; Rieter, W. J.; An, H.; Lin, W.; Lin, W. *J. Am. Chem. Soc.* **2008**, *130* (7), 2154–2155.
(52) Fortin, M.-A.; Petoral Jr, R. M.; Söderlind, F.; Klasson, A.; Engström, M.; Veres, T.; Käll, P.-O.; Uvdal, K. *Nanotechnology* **2007**, *18* (39), 395501.
(53) Bridot, J.-L.; Faure, A.-C.; Laurent, S.; Rivière, C.; Billotey, C.; Hiba, B.; Janier, M.; Josserand, V.; Coll, J.-L.; Vander Elst, L.; Muller, R.; Roux, S.; Perriat, P.; Tillement, O. *J. Am. Chem. Soc.* **2007**, *129* (16), 5076–5084.
(54) Comblin, V.; Gilsoul, D.; Hermann, M.; Humblet, V.; Jacques, V.; Mesbahi, M.; Sauvage, C.; Desreux, J. F. *Coord. Chem. Rev.* **1999**, *185-186*, 451–470.
(55) Parac-Vogt, T. N.; Vander Elst, L.; Kimpe, K.; Laurent, S.; Burtéa, C.; Chen, F.; Van Deun, R.; Ni, Y.; Muller, R. N.; Binnemans, K. *Contrast Media Mol. Imaging* **2006**, *1* (6), 267–278.
(56) Parac-Vogt, T. N.; Pacco, A.; Nockemann, P.; Laurent, S.; Muller, R. N.; Wickleder, M.; Meyer, G.; Vander Elst, L.; Binnemans, K. *Chem. - A Eur. J.* **2006**, *12* (1), 204–210.
(57) Astashkin, A. V.; Raitsimring, A. M.; Caravan, P. *J. Phys. Chem. A* **2004**, *108* (11), 1990–2001.
(58) Holz, M.; Heil, S. R.; Sacco, A. *Phys. Chem. Chem. Phys.* **2000**, *2* (20), 4740–4742.
(59) Roch, A.; Gossuin, Y.; Muller, R. N.; Gillis, P. *J. Magn. Magn. Mater.* **2005**, *293* (1), 532–539.
(60) Matsumoto, Y.; Jasanoff, A. *Magn. Reson. Imaging* **2008**, *26* (7), 994–998.
(61) Marckmann, P. *J. Am. Soc. Nephrol.* **2006**, *17* (9), 2359–2362.
(62) European Medicines Agency. European Medicines Agency makes recommendations to minimise risk of nephrogenic systemic fibrosis with gadolinium-containing contrast agents http://www.ema.europa.eu/ema/index.jsp?curl=pages/news_and_events/news/2009/11/news_detail_000408.jsp&mid=WC0b01ac058004d5c1 (accessed Sep 11, 2015).
(63) Joshi, B. P.; Wang, T. D. *Cancers* **2010**, *2* (2), 1251–1288.
(64) Orosco, R. K.; Tsien, R. Y.; Nguyen, Q. T. *IEEE Rev. Biomed. Eng.* **2013**, *6*, 178–187.
(65) Kobayashi, H.; Ogawa, M.; Alford, R.; Choyke, P. L.; Urano, Y. *Chem. Rev.* **2010**, *110* (5), 2620–2640.
(66) Wu, B.; Piatkevich, K. D.; Lionnet, T.; Singer, R. H.; Verkhusha, V. V. *Curr. Opin. Cell Biol.* **2011**, *23* (3), 310–317.
(67) Saito, K.; Nagai, T. *Curr. Opin. Chem. Biol.* **2015**, *27*, 46–51.

(68) Hong, G.; Zou, Y.; Antaris, A. L.; Diao, S.; Wu, D.; Cheng, K.; Zhang, X.; Chen, C.; Liu, B.; He, Y.; Wu, J. Z.; Yuan, J.; Zhang, B.; Tao, Z.; Fukunaga, C.; Dai, H. *Nat. Commun.* **2014**, *5*.

(69) Ruan, G.; Agrawal, A.; Smith, A. M.; Gao, X.; Nie, S. In *Reviews in Fluorescence 2006*; Geddes, C. D., Lakowicz, J. R., Eds.; Reviews in Fluorescence; Springer US: Boston, MA, 2006; Vol. 2006, pp 181–193.

(70) Resch-Genger, U.; Grabolle, M.; Cavaliere-Jaricot, S.; Nitschke, R.; Nann, T. *Nat. Methods* **2008**, *5* (9), 763–775.

(71) Chen, Z.; Zheng, W.; Huang, P.; Tu, D.; Zhou, S.; Huang, M.; Chen, X. *Nanoscale* **2015**, *7* (10), 4274–4290.

(72) Carron, S.; Li, Q. Y.; Vander Elst, L.; Muller, R. N.; Capobianco, J. A.; Parac-Vogt, T. N. *Dalt. Trans.* **2015**, *44* (25), 11331–11339.

(73) Niu, S. *Advanced water soluble BODIPY dyes : Synthesis and application*; 2011.

(74) Treibs, A.; Kreuzer, F.-H. *Justus Liebigs Ann. Chem.* **1968**, *718* (1), 208–223.

(75) Yee, M.; Fas, S. C.; Stohlmeyer, M. M.; Wandless, T. J.; Cimprich, K. A. *J. Biol. Chem.* **2005**, *280* (32), 29053–29059.

(76) West, R.; Panagabko, C.; Atkinson, J. *J. Org. Chem.* **2010**, *75* (9), 2883–2892.

(77) Kowada, T.; Maeda, H.; Kikuchi, K. *Chem. Soc. Rev.* **2015**, *44* (14), 4953–4972.

(78) Boens, N.; Leen, V.; Dehaen, W. *Chem. Soc. Rev.* **2012**, *41* (3), 1130–1172.

(79) García-Moreno, I.; Amat-Guerri, F.; Liras, M.; Costela, A.; Infantes, L.; Sastre, R.; López Arbeloa, F.; Bañuelos Prieto, J.; López Arbeloa, Í. *Adv. Funct. Mater.* **2007**, *17* (16), 3088–3098.

(80) Duran-Sampedro, G.; Agarrabeitia, A. R.; Garcia-Moreno, I.; Costela, A.; Bañuelos, J.; Arbeloa, T.; López Arbeloa, I.; Chiara, J. L.; Ortiz, M. J. *European J. Org. Chem.* **2012**, *2012* (32), 6335–6350.

(81) Lakshmi, V.; Rajeswara Rao, M.; Ravikanth, M. *Org. Biomol. Chem.* **2015**, *13* (9), 2501–2517.

(82) Bessette, A.; Hanan, G. S. *Chem. Soc. Rev.* **2014**, *43* (10), 3342.

(83) Singh, S. P.; Gayathri, T. *European J. Org. Chem.* **2014**, *2014* (22), 4689–4707.

(84) González-Béjar, M.; Liras, M.; Francés-Soriano, L.; Voliani, V.; Herranz-Pérez, V.; Duran-Moreno, M.; Garcia-Verdugo, J. M.; Alarcon, E. I.; Scaiano, J. C.; Pérez-Prieto, J. *J. Mater. Chem. B* **2014**, *2* (28), 4554.

(85) Lim, S. H.; Thivierge, C.; Nowak-Sliwinska, P.; Han, J.; van den Bergh, H.; Wagnières, G.; Burgess, K.; Lee, H. B. *J. Med. Chem.* **2010**, *53* (7), 2865–2874.

(86) Loudet, A.; Burgess, K. *Chem. Rev.* **2007**, *107* (11), 4891–4932.

(87) Ulrich, G.; Ziessel, R.; Harriman, A. *Angew. Chemie Int. Ed.* **2008**, *47* (7), 1184–1201.

(88) Bernhard, C.; Goze, C.; Rousselin, Y.; Denat, F. *Chem. Commun.* **2010**, *46* (43), 8267.

(89) Bernhard, C.; Moreau, M.; Lhenry, D.; Goze, C.; Boschetti, F.; Rousselin, Y.; Brunotte, F.; Denat, F. *Chem. - A Eur. J.* **2012**, *18* (25), 7834–7841.

(90) Iwaki, S.; Hokamura, K.; Ogawa, M.; Takehara, Y.; Muramatsu, Y.; Yamane, T.; Hirabayashi, K.; Morimoto, Y.; Hagisawa, K.; Nakahara, K.; Mineno, T.; Terai, T.; Komatsu, T.; Ueno, T.; Tamura, K.; Adachi, Y.; Hirata, Y.; Arita, M.; Arai, H.; Umemura, K.; Nagano, T.; Hanaoka, K. *Org. Biomol. Chem.* **2014**, *12* (43), 8611–8618.

(91) Yamane, T.; Hanaoka, K.; Muramatsu, Y.; Tamura, K.; Adachi, Y.; Miyashita, Y.; Hirata, Y.; Nagano, T. *Bioconjug. Chem.* **2011**, *22* (11), 2227–2236.

(92) Koullourou, T.; Natrajan, L. S.; Bhavsar, H.; Pope; Feng, J.; Narvainen, J.; Shaw, R.; Scales, E.; Kauppinen, R.; Kenwright, A. M.; Faulkner, S. *J. Am. Chem. Soc.* **2008**, *130* (7), 2178–2179.

(93) Dehaen, G.; Eliseeva, S. V.; Kimpe, K.; Laurent, S.; Vander Elst, L.; Muller, R. N.; Dehaen, W.; Binnemans, K.; Parac-Vogt, T. N.; Vanderelst, L.; Muller, R. N.; Dehaen, W.; Binnemans, K.; Parac-Vogt, T. N. *Chem. - A Eur. J.* **2012**, *18* (Iv), 293–302.

(94) Debroye, E.; Dehaen, G.; Eliseeva, S. V.; Laurent, S.; Vander Elst, L.; Muller, R. N.; Binnemans, K.; Parac-Vogt, T. N. *Dalt. Trans.* **2012**, *41* (35), 10549.

(95) Dehaen, G.; Verwilst, P.; Eliseeva, S. V.; Laurent, S.; Vander Elst, L.; Muller, R. N.; De Borggraeve, W. M.; Binnemans, K.; Parac-Vogt, T. N. *Inorg. Chem.* **2011**, *50* (20), 10005–10014.

(96) Dehaen, G.; Eliseeva, S. V.; Verwilst, P.; Laurent, S.; Vander Elst, L.; Muller, R. N.; De Borggraeve, W. M.; Binnemans, K.; Parac-Vogt, T. N. *Inorg. Chem.* **2012**, *51* (16), 8775–8783.

(97) Werts, M. H. V. *Sci. Prog.* **2005**, *88* (Pt 2), 101–131.

(98) Dexter, D. L. *J. Chem. Phys.* **1953**, *21* (5), 836.

(99) Förster, T. *Discuss. Faraday Soc.* **1959**, *27*, 7.

(100) Courrol, L. C.; de Oliveira Silva, F. R.; Gomes, L.; Vieira Júnior, N. D. *J. Lumin.* **2007**, *122-123*, 288–290.

(101) Sabbatini, N.; Guardigli, M.; Lehn, J.-M. *Coord. Chem. Rev.* **1993**, *123* (1-2), 201–228.

(102) Horrocks, W. D.; Sudnick, D. R. *J. Am. Chem. Soc.* **1979**, *101* (2), 334–340.

(103) Cotton, S. *Lanthanide and Actinide Chemistry*; 2005.

(104) Gautam, A.; van Veggel, F. C. J. M. *J. Mater. Chem. B* **2013**, *1* (39), 5186.

(105) Tang, F.; Li, L.; Chen, D. *Adv. Mater.* **2012**, *24* (12), 1504–1534.

(106) Soenen, S. J.; Parak, W. J.; Rejman, J.; Manshian, B. *Chem. Rev.* **2015**, *115* (5), 2109–2135.

[†] Illustrations courtesy of Siemens Healthcare GmbH and can be found in their product brochures of MAGNETOM series MRI instruments or their website: http://www.healthcare.siemens.com/magnetic-resonance-imaging

CHAPTER 3

Luminescent Metallostar Complexes

This chapter is based on a manuscript published in *European Journal of Inorganic Chemistry*, 2015, 4207–4216.

"Luminescence and Relaxometric Properties of Heteropolymetallic Metallostar Complexes with Selectively Incorporated Lanthanide(III) Ions", Matthias Ceulemans, Elke Debroye, Luce Vander Elst, Wim M. De Borggraeve, and Tatjana N. Parac-Vogt.

This chapter builds on previous work published by Dr. Elke Debroye.[1] Synthesis and complexation of the reported complex was done in framework of an Erasmus project by Miguel Roldán Albaladejo under supervision of Drs. Matthias Ceulemans. The synthesis leading to the triazole linked product was done by Pieter Vanstraelen as his internship project guided by Drs. Michael Harris and Drs. Matthias Ceulemans. The design and synthesis leading to the ethynyl linked product was done by Drs. Matthias Ceulemans. Gratitude goes towards Prof. Koen Binnemans for TXRF measurements. Relaxometric data were measured and fitted by Prof. Luce Vander Elst at the University of Mons.

1 Introduction

As mentioned in previous chapters the design of lanthanide based systems for potential bimodal imaging attracts a lot of attention. Complexes with both a paramagnetic gadolinium(III) and lanthanide(III) bearing ions can emit in a broad region from visible[2] to NIR[3] and have been intensively studied. Heteropolymetallic complexes with two different chelates and an integrated antenna remain difficult to synthesize in a controlled way due to the coordination similarities along the lanthanide series.

This chapter builds on previously published work where the successful synthesis of a heterotetrametallic complex, $(Gd\mathbf{L^1})_3Eu$, was reported.[1] Two different lanthanide(III) ions were selectively incorporated into one ligand, $\mathbf{L^1}$. The resulting complex contained three Gd-DTPA moieties linked to an europium(III) chelate consisting of a para-substituted dipicolinic acid (DPA), and exhibited both high relaxivity, due to the presence of three gadolinium(III) ions and rigidity, and favorable europium(III) luminescence. Encouraged by these results, we further extend this strategy toward creating potential bimodal contrast agents with selectively incorporated lanthanide ions. A series of $(Gd\mathbf{L^1})_3Ln$ complexes in which Ln represents different luminescent lanthanide(III) ions, has been prepared. In addition, two novel ligands which contain an ethynyl or a triazole linker between the two aromatic centers, have been synthesized with the aim to decrease the excited triplet state of the ligand in order to provide better energy transfer to ytterbium(III).[3] Using the same selective synthetic approach, a series of heterotetrametallic complexes based on these novel ligands have been synthesized and characterized. The magnetic and luminescent properties of the complexes have been studied and their potential as bimodal contrast agents for MRI and optical imaging has been evaluated.

2 Results and discussion

2.1 Ligand design and synthesis

The general ligand design is based on attaching a DTPA scaffold via an amide linkage to para-substituted dipicolinic acid (DPA), which has previously been demonstrated to form tris complexes with lanthanide(III) ions.[1] This approach allows for incorporation of different antennas between coordinating moieties to sensitize the luminescent lanthanide ion. A first method has been previously reported by our group and resulted in the synthesis of a Eu(III) metallostar complex.[1] It uses a Suzuki-Miyaura coupling[4] to obtain a fully protected dipicolinate derivative, in which gadolinium(III) could be selectively incorporated in the DTPA unit. Subsequent removal of the protecting groups and coordination to a luminescent lanthanide(III) ion (Ln = Eu,[1] Tb, Dy, Sm, Ho, Tm, and Yb) yields the desired metallostar complex (Scheme 3.1). All metallostar complexes contain three gadolinium(III)-DTPA units, but differ in the nature of the central lanthanide(III) ion bound to the dipicolinate units.

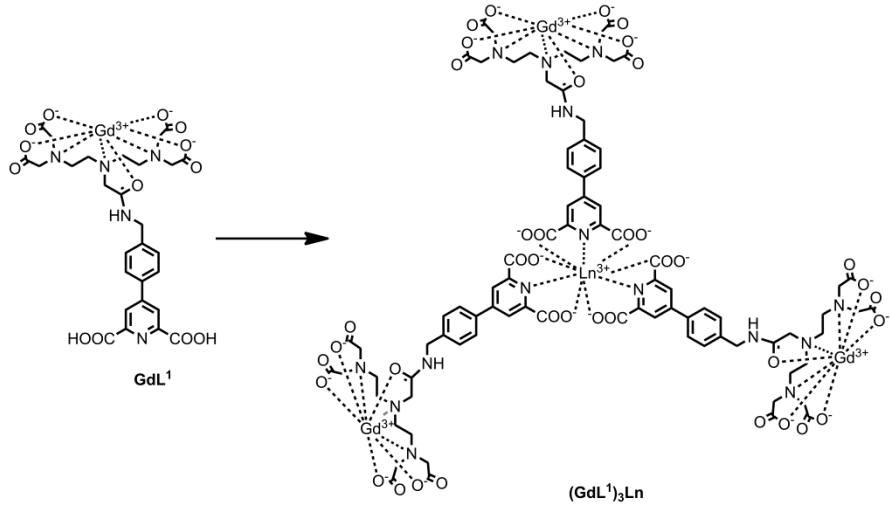

Scheme 3.1. Schematic representation of the complex GdL^1 and the heterotetrametallic metallostar $(GdL^1)_3Ln$ (Ln = Eu(III),[1] Dy(III), Tb(III), Ho(III), Nd(III), Sm(III), Tm(III), and Yb(III)).

The synthesis of the novel ligand $\mathbf{L^2}$ makes use of Sonogashira cross-couplings reaction and employs a slightly altered synthetic pathway than the one previously reported by Bünzli *et al.*[5] The first step is the protection of 4-iodobenzylamine with *t*-boc-anhydride resulting in compound **(1)**. Compound **(1)** is subsequently coupled to trimethylsilylacetylene via a Sonogashira cross-coupling **(2)** and subsequent deprotection of the trimethylsilylgroup yields compound **(3)**. The NMR spectrum clearly shows the disappearance of the highly shielded trimethylsilyl protons at 0.24 ppm and the appearance of a single proton peak of the ethynyl group at 3.06 ppm. Compound **(3)** is able to undergo another Sonogashira cross-coupling under the same conditions to dimethyl-4-bromo-2,6-pyridinedicarboxylate, resulting in compound **(4)** (Scheme 3.2).

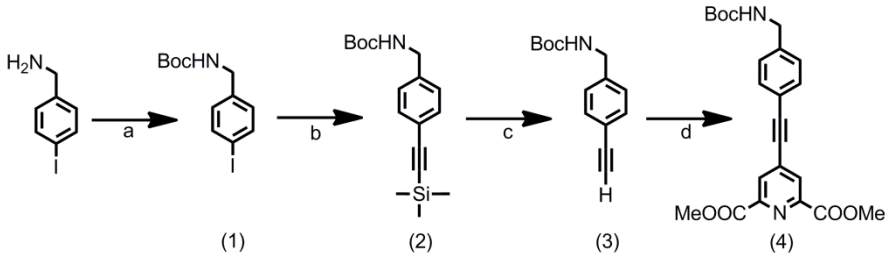

Scheme 3.2. Synthetic pathway GdL^2: a) Boc-anhydride, b) ethynyl trimethylsilane, CuI, $PdCl_2(PPh_3)_2$, c) 1 M TBAF, d) dimethyl-4-bromo-2,6-pyridinedicarboxylate, CuI, $PdCl_2(PPh_3)_2$.

The *t*-Boc group is selectively deprotected using trifluoroacetic acid in dichloromethane (50/50), which is confirmed by the disappearance of the *tert*-butyl peaks at 1.45 ppm and the persistence of the methyl peaks at 4.06 ppm in the NMR spectrum. This approach results in a free amine **(5)** which can be coupled to the one free acid of the DTPA *t*-butylester via amide synthesis, resulting in a fully protected ligand **(6)**. At last, the DTPA *tert*-butyl esters are selectively cleaved using a 6 M HCl solution, resulting in compound **(7).** (Scheme 3.3) The acidic groups of DTPA can then be further coordinated to gadolinium(III). The complexation was performed by using $GdCl_3{\cdot}6H_2O$ in pyridine and the absence of free lanthanide ions is verified by the addition of an arsenazo indicator solution.[6] Selective removal of the methyl ester protective groups from the dipicolinate moiety is done under alkaline conditions and the final ligand is mixed with a

luminescent lanthanide ($LnCl_3 \cdot xH_2O$) salt (Ln = Eu, Tb, Dy, Sm, Ho, Tm, Yb). By this approach the desired metallostar tris complexes $(GdL^2)_3Ln$ are generated, as schematically shown in Scheme 3.4.

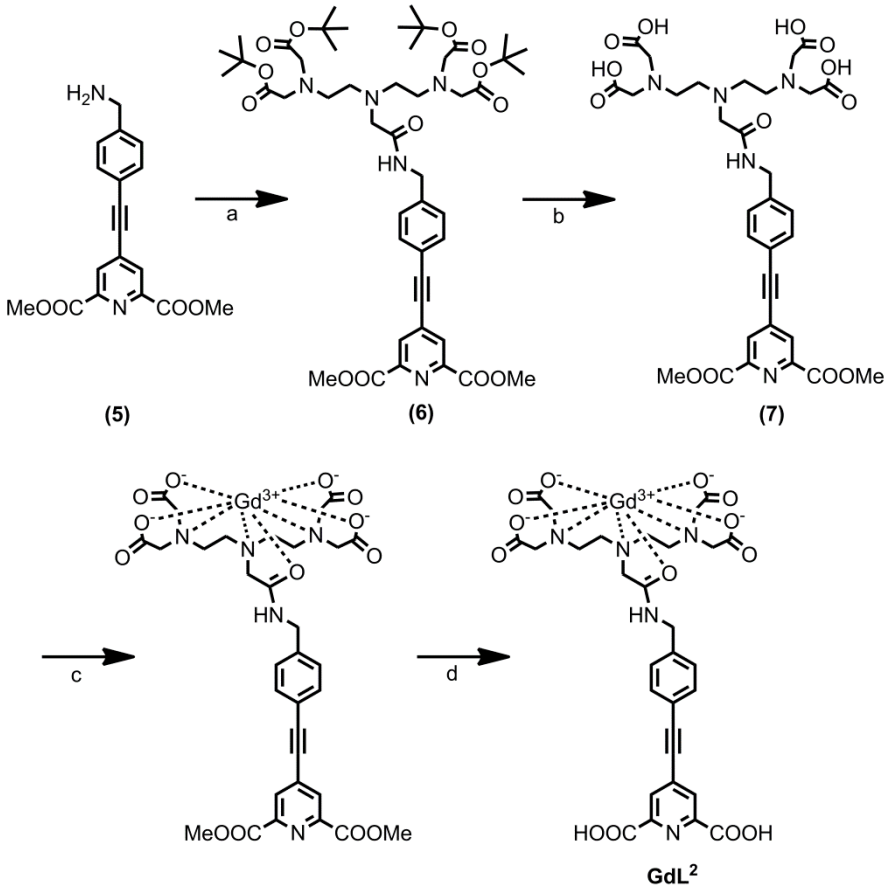

Scheme 3.3. Synthetic pathway GdL^2: a) DTPA *t*-butylester, TBTU, DIPEA, b) 6 M HCl, c) $GdCl_3 \cdot 6H_2O$, pyridine, d) K_2CO_3.

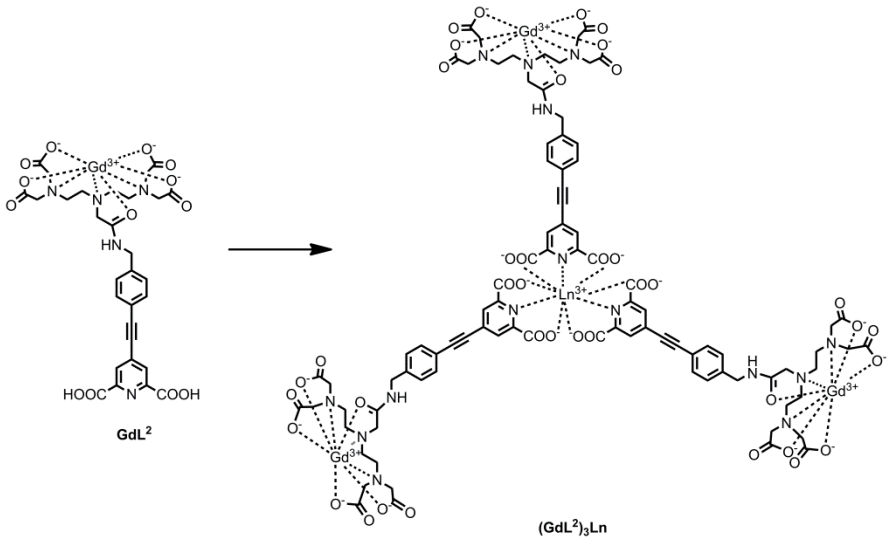

Scheme 3.4. Schematic representation of the complex GdL^2 and the heterotetrametallic metallostar $(GdL^2)_3Ln$ (Ln = Eu(III), Dy(III), Tb(III), Nd(III), Sm(III), Tm(III), and Yb(III)).

The synthesis of ligand $\mathbf{L^3}$ employs click chemistry to combine compound **(3)** with dimethyl-4-azido-pyridine-2,6-dicarboxylate (**8**) to form the protected compound (**9**). Coupling of this compound to a *tert*-butyl protected DTPA unit with TBTU and a base, subsequent deprotection with a 50:50 TFA/DCM mixture yields a ligand with a DTPA containing moiety. Complexation of this DTPA unit with Gd(III) in pyridine yields the methoxy protected Gd$\mathbf{L^3}$ ligand. A saponification step with K_2CO_3 provides us with Gd$\mathbf{L^3}$. No loss of gadolinium(III) was observed during this reaction. A subsequent complexation step, leads to a novel red luminescent (Gd$\mathbf{L^3}$)$_3$Eu metallostar complex depicted in Scheme 3.6.

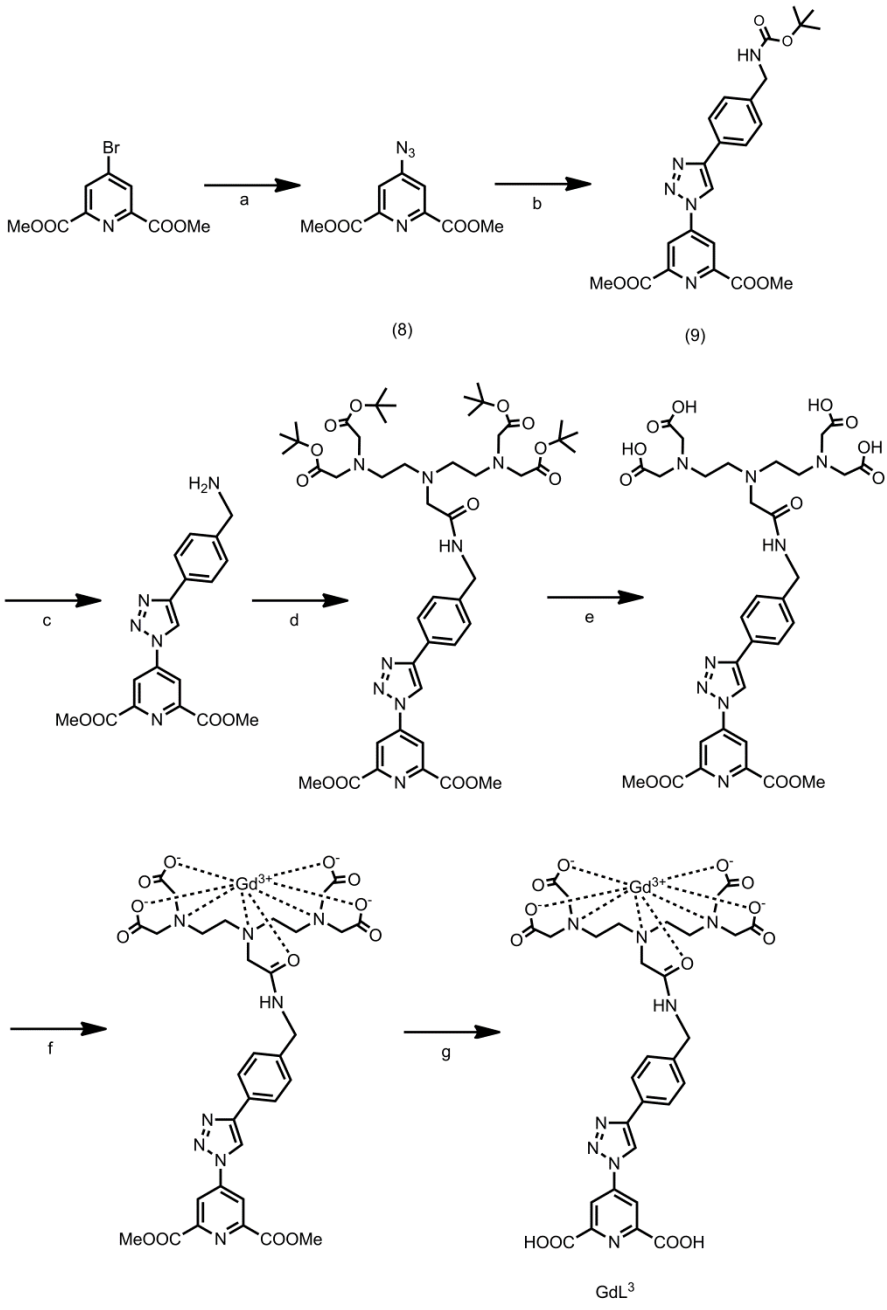

Scheme 3.5. Synthetic pathway of GdL^3: a) NaN_3, b) compound (3), $CuSO_4$, sodium ascorbate, c) TFA/DCM, d) DTPA *t*-butylester, TBTU, DIPEA, e) DCM/TFA, f) $GdCl_3 \cdot 6H_2O$, pyridine, d) K_2CO_3.

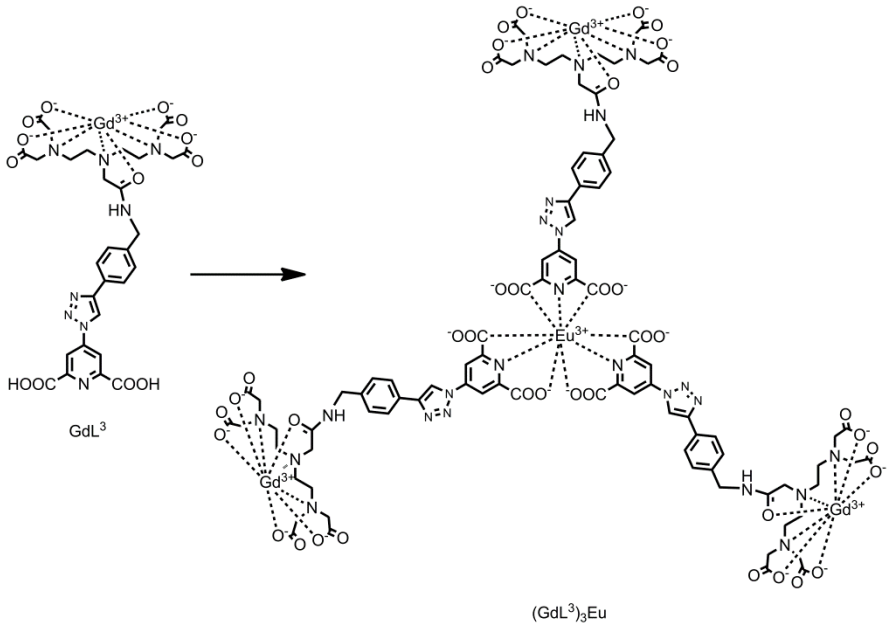

Scheme 3.6. Schematic representation of the complex GdL^3 and the metallostar $(GdL^3)_3Eu$.

2.2 Photophysical properties

The absorption spectrum of the Gd**L**^{1} complex has a well defined maximum around 282 nm (ε = 4250 $cm^{-1}M^{-1}$) caused by the $\pi \rightarrow \pi^*$ transition of DPA.[7] The excitation spectrum shows a broad band between 250 and 300 nm with a maximum at 295 nm. The absorption spectra of Gd**L**^{2} and the tris complex (Gd**L**^{2})$_3$Ln, both show an absorption maximum at 315 nm. The molar extinction coefficient of the free complex Gd**L**^{2} at this maximum is ε_{315} = 6692 $cm^{-1}M^{-1}$, while the one tris-complex has ε_{315} = 11000 $cm^{-1}M^{-1}$.

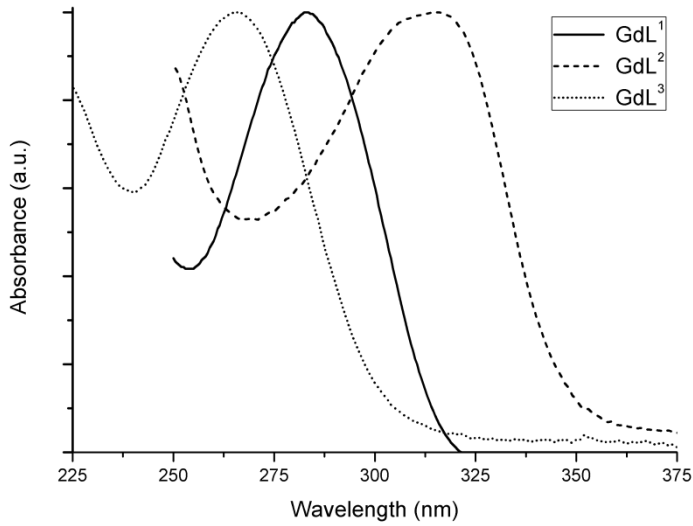

Figure 3.1. Normalized absorption spectra of GdL^{X} (X = 1-3) at room temperature.

In the emission spectra of (Gd**L**^{1})$_3$Eu, (Gd**L**^{2})$_3$Eu and (Gd**L**^{3})$_3$Eu metallostar complexes, the $^5D_0 \rightarrow {}^7F_1$ transition shows splitting into three bands, which suggests a slightly deformed D3 symmetry around the central ion (Figure 3.2).[1,8] This is further supported by the ratio of the $^5D_0 \rightarrow {}^7F_2$ and $^5D_0 \rightarrow {}^7F_1$ transition which is ca. 5-6.

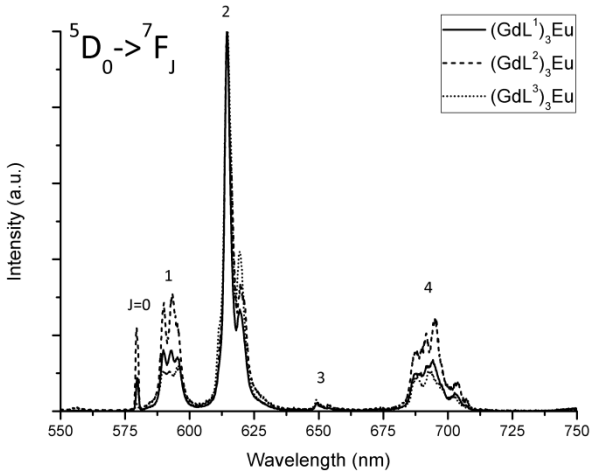

Figure 3.2. Corrected and normalized emission spectra at room temperature of $(GdL^1)_3Eu$ (λ_{exc} = 293 nm), $(GdL^2)_3Eu$ (λ_{exc} = 315 nm), and $(GdL^3)_3Eu$ (λ_{exc} = 262 nm).

Luminescence decays of the metallostar complexes $(Gd\mathbf{L}^1)_3Eu$ and $(Gd\mathbf{L}^2)_3Eu$ have been measured in water and D_2O, and the results are shown in Table 3.2. The decrease of the luminescence lifetime in water compared to D_2O is due to the presence of inner sphere high-energy O-H vibrations and can be used for determining the number of coordinated water molecules. The best fit was observed by applying a bi-exponential decay, which suggests the presence of two different species in solution. The phenomenological equation[9,10] has been employed to determine the hydration number q with an accuracy of ± 0.3.

$$q_{\mathrm{Eu\,(H_2O)}} = 1.11(\Delta k_{obs} - 0.31 + 0.44q^{OH} + 0.99q^{NH} + 0.075q^{CONH}) \quad \text{(eq. 3.1)}$$

In eq. 3.1, Δk_{obs} represents the difference of the decay rate constants $k_{H_2O}(1/\tau_{H_2O})$ and $k_{D_2O}(1/\tau_{D_2O})$, expressed in ms^{-1} for Eu(III). The q^X stands for the number of OH, NH or CONH groups directly bound to the lanthanide center. The results indicate that at the low concentrations used for luminescence measurements ($2.0 \cdot 10^{-5}$ M), an equilibrium has been set between the bis and tris complex. These findings are consistent with those previously reported for

$(DPA)_3Eu$ complexes, in which a significant amount of bis complexes was detected in micromolar concentrations range.[11] As no water is present in the first coordination sphere of the central ion in the tris complex, while in the bis complex there should be three water molecules bound. This allows for determining the ratio of tris/bis complex. An increase of the ratio of tris to bis complex, from 80:20 for $(Gd\mathbf{L^1})_3Eu$ to 93:7 for $(Gd\mathbf{L^2})_3Eu$, is seen upon introduction of an ethynyl linker in the ligand structure. The luminescent quantum yields Q_L^{Ln} were determined upon ligand excitation by a comparative method, using a solution of Rhodamine 101 in ethanol (Q = 100%) as the standard. The quantum yield was determined according to the following equation:

$$Q_L^{Ln} = Q_S \cdot \frac{I_X}{I_S} \cdot \frac{A_S(\lambda_{exc})}{A_X(\lambda_{exc})} \cdot \frac{\eta_X^2}{\eta_S^2} \qquad \text{(eq. 3.2)}$$

In this equation, the s and x refer to the standard and the unknown sample respectively, I represents the corrected total integrated emission intensity, A is the absorbance at the excitation wavelength and η the refractive index of the solution (η_{water} = 1.34 and $\eta_{ethanol}$ = 1.36). The quantum yields are summarized in Table 3.3. Apparently due to the lower $\pi\pi^*$ energy level of $Gd\mathbf{L^2}$, the quantum yield of the complex drops from 9.8% for $(Gd\mathbf{L^1})_3Eu$ to 1.5% of $(Gd\mathbf{L^2})_3Eu$, indicating that $\mathbf{L^2}$ is less efficient in sensitizing europium emission. The observed quantum yield for $(Gd\mathbf{L^3})_3Eu$ was only 0.5%. Direct excitation into the lanthanides is possible but is very inefficient because the *f-f* transitions are Laporte forbidden. The intrinsic quantum yields Q_{Ln}^{Ln} (Ln(III) = Eu(III), Tb(III)) can however be estimated according to the following equations comprising the ratio between the observed (τ_{obs}) and radiative (τ_{rad}) lifetimes.

$$\frac{1}{\tau_{obs}} = A_{MD,0} \cdot n^3 \cdot \left(\frac{I_{tot}}{I_{MD}}\right) \qquad \text{(eq. 3.3)}$$

$$Q_{Ln}^{Ln} = \frac{\tau_{obs}}{\tau_{rad}} \qquad \text{(eq. 3.4)}$$

The Einstein coefficient $A_{MD,0}$ equals 14.65 s^{-1}, n is the refractive index set to $n_{H_2O} = 1.34$, which is equal to that of the neat solvent, and (I_{tot}/I_{MD}) represents the ratio of the total integrated intensity of the transitions to the transition of the magnetic dipole (MD). The intrinsic quantum yield values Q_{Eu}^{Eu} for both the Gd**L**^{1} and Gd**L**^{2} complexes are in the range of 22-24%. At last, we can acquire the ratio between the quantum yield under ligand excitation and the intrinsic quantum yield to obtain the sensitization efficiency (η_{sens}) of the ligand:

$$\eta_{sens} = \frac{Q_L^{Eu}}{Q_{Eu}^{Eu}} \qquad \text{(eq. 3.5)}$$

This results in a sensitization efficiency for (Gd**L**^{1})$_3$Eu of 47% and only 6.3% for (Gd**L**^{2})$_3$Eu. These values are lower than those for the parent (DPA)$_3$Eu complex, which has Q_{Eu} = 24% and η_{sens} = 61%.[7]

Dysprosium(III) complexes with Gd**L**^{1} and Gd**L**^{2}, showed yellow emission due to transitions $^4F_{9/2} \rightarrow {}^6H_J$ (J = 15/2, 13/2 and 11/2). (Gd**L**^{1})$_3$Dy clearly shows these three transitions of Dy(III) with some ligand emission, while the (Gd**L**^{2})$_3$Dy emission spectrum is dominated by ligand emission due to poor sensitization (Figure 3.3). The $^4F_{9/2} \rightarrow {}^6H_{15/2}$ transition, which is typically observed at 485 nm, has completely disappeared under the ligand emission tail. However, the $^4F_{9/2} \rightarrow {}^6H_{13/2}$ transition which is located around 575 nm is clearly visible together with the weak transition of $^4F_{9/2} \rightarrow {}^6H_{11/2}$ at 665 nm. Quantum yields for the dysprosium(III) samples have been measured by the method using a solution of Rhodamine 101 in ethanol (Q = 100%) as a standard. Using eq. 3.2, low values of 1.2% for (Gd**L**^{1})$_3$Dy and 0.8% for (Gd**L**^{2})$_3$Dy are obtained (Table 3.3). The poor efficiency of the ligands to sensitize dysprosium(III) could already be observed in the luminescence spectra. The amount of water molecules can be calculated using the phenomenological equation 3.6:[12–14]

$$q_{\mathrm{Dy\,(H_2O)}} = 21.1 \cdot \Delta k_{obs} - 0.60 \qquad \text{(eq. 3.6)}$$

Values of 1.2 and 0.3 are obtained for (Gd**L**^{1})$_3$Dy and (Gd**L**^{2})$_3$Dy respectively, which results in a ratio of tris to bis complex of 60:40 and 90:10.

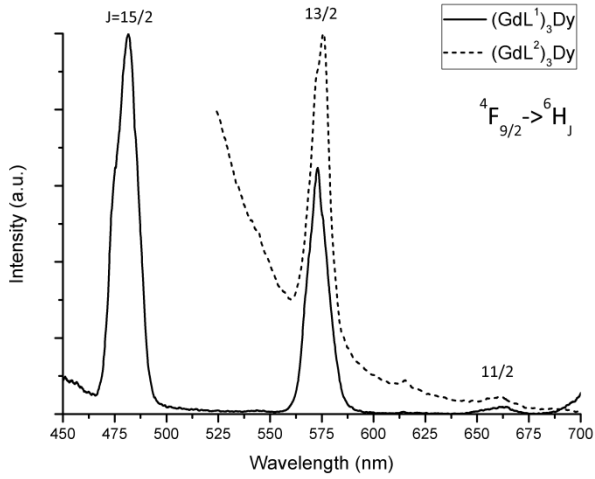

Figure 3.3. Corrected and normalized emission spectra at room temperature of (GdL^1)$_3$Dy (λ_{exc} = 293 nm) and (GdL^2)$_3$Dy (λ_{exc} = 315 nm).

Characteristic green emission is observed for terbium(III) complexes of both Gd**L**^{1} and Gd**L**^{2}, exciting the ligand at 295 nm and 315 nm respectively, due to the Tb(III) $^5D_4 \rightarrow {}^7F_J$ (J = 6-0) transitions (Figure 3.4). Quantum yields for terbium(III) complexes are relative high, using the comparative method of Rhodamine 101, ranging from 30% for (Gd**L**^{1})$_3$Tb to 15% for (Gd**L**^{2})$_3$Tb. The amount of water molecules bound to the luminescent centre can also be determined out of lifetime measurements in H_2O and D_2O using eq. 3.7 and are shown Table 3.3. [9,15]

$$q_{\mathrm{Tb\,(H_2O)}} = 5 \cdot (\Delta k_{\mathrm{obs}} - 0.06) \qquad \text{(eq. 3.7)}$$

The overall ratios of tris to bis complexes for (Gd**L**^{1})$_3$Tb and (Gd**L**^{2})$_3$Tb are 57:43 and 73:27 respectively. These ratios are lower than for the other lanthanides, but still very high quantum yields can be obtained, since the energy from the excited state of terbium(III) is poorly quenched by water.

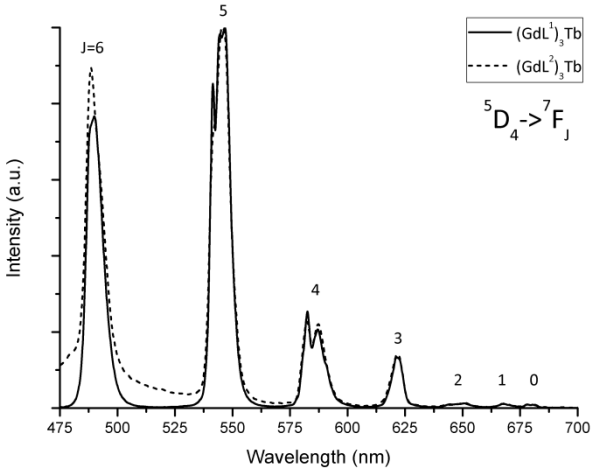

Figure 3.4. Corrected and normalized emission spectra at room temperature of $(GdL^1)_3Tb$ (λ_{exc} = 293 nm) and $(GdL^2)_3Tb$ (λ_{exc} = 315 nm).

Tris complexes of all other luminescent lanthanides such as neodymium(III), holmium(III), samarium(III) or thulium(III) unfortunately only give rise to ligand emission and no distinct peaks for lanthanide emission could be observed. The low energy of the $\pi\pi^*$ state apparently makes both $\mathbf{L^1}$ and $\mathbf{L^2}$ poor sensitizers for these lanthanides.

Table 3.1. TXRF ratios of Gd to Ln of the metallostar complexes.

ratio	Tb	Dy	Ho	Sm	Nd	Tm	Yb
(Gd$\mathbf{L^1}$)-Ln	2.49	2.80	3.07	3.54	3.18	3.73	1.92
(Gd$\mathbf{L^2}$)-Ln	3.06	3.06	2.92	2.59	2,70	/	3.03

However, in the case of the ytterbium(III) ion complex $(Gd\mathbf{L^2})_3Yb$ emission at 980 nm corresponding to $^2F_{5/2} \rightarrow {}^2F_{7/2}$ transition could be observed when the complex was measured in the solid state, while it was absent for $(Gd\mathbf{L^1})_3Yb$. Luminescence in the IR region was not seen in aqueous solutions of either $(Gd\mathbf{L^1})_3Yb$ nor $(Gd\mathbf{L^2})_3Yb$, most likely because of the quenching of the radiative emission by water. (Figure 3.5)

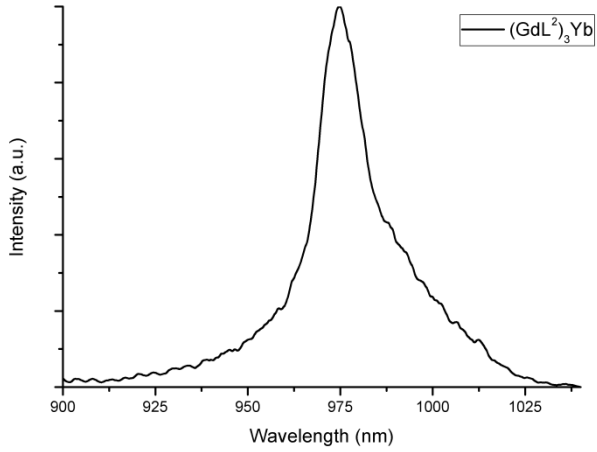

Figure 3.5. Corrected and normalized solid state emission spectrum of $(GdL^2)_3Yb$ (λ_{exc} = 315 nm).

Table 3.2. Luminescence lifetimes of the different $(GdL)_3Ln$ complexes (Ln = Eu, Dy, Tb), average number of calculated water molecules in the first coordination sphere (q) and the ratio of tris/bis complex under the conditions of the measurements ($2.0 \cdot 10^{-5}$ M).

	H_2O	D_2O	q	Ratio tris/bis
$(GdL^1)_3Eu$[a]	0.23 ms	1.12 ms	0.6	80:20
$(GdL^1)_3Dy$	9 µs	39 µs	1.2	60:40
$(GdL^1)_3Tb$	1.42 ms	2.42 ms	1.3	57:43
$(GdL^2)_3Eu$	0.20 ms	1.11 ms	0.2	93:7
$(GdL^2)_3Dy$	9 µs	14 µs	0.3	90:10
$(GdL^2)_3Tb$	2.20 ms	2.40 ms	0.8	73:27

[a] From ref. 1

Table 3.3. Calculated quantum yields of the $(GdL^1)_3Ln$ (λ_{exc} = 293 nm) and $(GdL^2)_3Ln$ complexes (λ_{exc} = 315 nm).

Ln	$(Gd\mathbf{L^1})_3Ln$	$(Gd\mathbf{L^2})_3Ln$
Eu	9.8%	1.5%
Dy	1.2%	0.8%
Tb	30.9%	15.3%

2.3 Relaxometric studies

The efficiency of a 1 mM solution of gadolinium(III) agent to shorten the longitudinal relaxation time (T_1) can be derived from proton NMRD profiles by measuring the water proton relaxivity (r_1) as a function of the magnetic field strength. The relaxation rate is enhanced by the dipolar interaction between the water molecules and the paramagnetic centre, gadolinium(III). Besides inner sphere contributions,[11,42] which result from the water molecules directly bound to the paramagnetic centre and exchanging with the bulk, outer sphere[43] interactions of water have to be taken into account and in some cases second sphere interactions[44] can have significant effects. Several parameters are defined for the inner sphere water molecules. While water molecules directly bound to the luminescent centre have a negative effect on the luminescence, a high relaxivity can be obtained with a higher amount of water molecules directly bound to the paramagnetic centre (q). Other parameters are the distance between gadolinium(III) and water (r), the water residence time (τ_M), the rotational correlation time of the paramagnetic centre (τ_R), the electronic relaxation time of gadolinium(III) at zero field (τ_{S0}) and the correlation time modulating the electronic relaxation (τ_v).

The ^{1}H NMRD profiles of $Gd\mathbf{L^1}$ and $(Gd\mathbf{L^1})_3Eu$ have been reported in a recent publication.[1] The profile of $(Gd\mathbf{L^1})_3Eu$ displayed a characteristic hump between 20 and 100 MHz which is assigned to the formation of a supramolecular structure. At 20 MHz and 310 K, the relaxivity is enhanced to 8.3 $s^{-1}mM^{-1}$ for $Gd\mathbf{L^1}$ and to 9.6 $s^{-1}mM^{-1}$ for $(Gd\mathbf{L^1})_3Eu$ with respect to 3.8 $s^{-1}mM^{-1}$ found for Gd-DTPA, as could be expected given the higher molecular weight of the synthesized chelates. Taken into account the presence of three gadolinium ions per metallostar compound, a

longitudinal relaxation rate of 28.8 $s^{-1}mM^{-1}$ per (Gd**L**^{1})$_3$Eu molecule is obtained at 20 MHz and 310 K.

In this chapter the relaxometric properties of metallostars based on the **L**^{2} ligand have been examined. Similarly to (Gd**L**^{1})$_3$Eu, the proton NMRD profiles of (Gd**L**^{2})$_3$Ln metallostars (measured in water at pH 7.4 and 310 K) show a hump between 20 and 100 MHz, characteristic of supramolecular structures in solution (Figure 3.6). It is to be pointed out that the NMRD profile of Gd**L**^{2} is quite similar to those of the metallostar complexes suggesting a self aggregation of the monomer to form dimeric, trimeric or multimeric species.

Table 3.4. Parameters obtained by fitting the ^{1}H NMRD data in water at pH 7.4 and 310 K. Fixed values q = 1, r = 0.31 nm, d = 0.36 nm, τ_M = 1500 ns and D = 3.0·10^{-9} m^{2}s^{-1}.

Parameter (ps)	Gd-DTPA [a]	Gd**L**^{2}	(Gd**L**^{2})$_3$Eu	(Gd**L**^{2})$_3$Dy	(Gd**L**^{2})$_3$Tb
τ_R	54 ± 1	809 ± 48	1000 ± 3	818 ± 35	916 ± 41
τ_{S0}	87 ± 3	83 ± 1	64 ± 1	70 ± 1	66 ± 1
τ_V	25 ± 3	20 ± 1	21 ± 1	18 ± 1	17 ± 1

[a] From ref. 20

The NMRD data shown in Figure 3.6 are fitted to the Solomon-Bloembergen-Morgan equation, which as expected indicate a significant increase of τ_R compared to Gd-DTPA. However, due to the possible equilibria between tris and bis complexes, the precise values of τ_R are difficult to determine. It should be noted that equilibria between tris and bis complex observed in the luminescence measurements might be absent, or present to lesser extent due to the higher concentrations used in the NMRD measurements. Also, from the stability constants of Ln-DTPA and Ln(DPA)$_3$ complexes it is plausible that redistribution of Gd(III) and Eu(III) ions between both the ligands may take place. However, this is unlikely as the emission spectrum of (Gd**L**^{1})$_3$Eu and (Gd**L**^{2})$_3$Eu does not show the splitting of $^5D_0 \rightarrow {}^7F_1$ transition, which would be expected to occur if Eu(III) would be complexed in the DTPA part. The relaxivities measured at 20 MHz at temperatures ranging between 25 and 45 °C increased by less than 13% indicating a slow water exchange. During the fitting procedure, τ_M was fixed to

1500 ns for all metallostars as well as for the Gd**L**^{2} complex. At 20 MHz and 310 K, the relaxivity of the complexes (Gd**L**^{2})$_3$Ln with Ln = Eu(III), Dy(III) and Tb(III), have been determined to be very similar (8.09, 7.60 and 7.24 $s^{-1}mM^{-1}$ respectively). Assuming the presence of three Gd-DTPA moieties, the expected r_1 relaxivity of the molecules would be 24.27, 22.8 and 21.72 $s^{-1}mM^{-1}$ per metallostar complex, which is slightly lower than the value of 28.8 $s^{-1}mM^{-1}$ observed for the (Gd**L**^{1})$_3$Eu metallostar.[1]

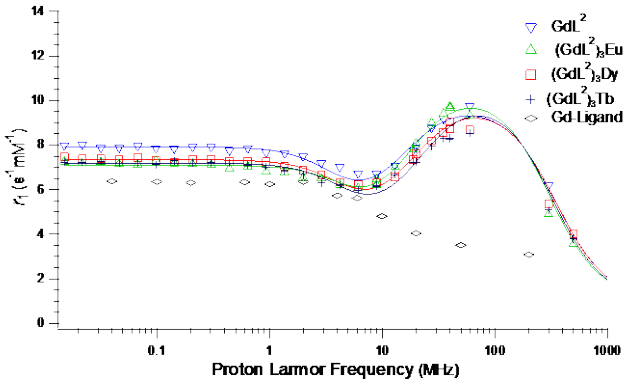

Figure 3.6. NMRD profiles of GdL^{2} and (GdL^{2})$_3$Ln (with Ln = Eu, Dy, and Tb) compared to Gd-DTPA in water at 310 K.

3 Conclusions

In this chapter, the selective incorporation of several lanthanides into two ditopic ligands has been accomplished leading to metallostar complexes which exhibited favorable luminescent and relaxometric properties for potential use as bimodal MRI/OI agents. Incorporation of Eu(III), Dy(III) and Tb(III) into the complexes results in emission in the visible region upon excitation into the ligand levels. Quantum yields of up to 10% for (Gd**L**^{1})$_3$Eu were achieved, with a sensitization efficiency (η_{sens}) of 47%. Introducing a ligand having an ethynyl group (Gd**L**^{2}) or triazole ring (Gd**L**^{3}), lowers the energy of the $\pi\pi^*$ excited state, resulting in the decrease of the quantum yield of the metallostar complex to 1.5% and 0.5% respectively, and a decrease of the sensitization efficiency to only 6.3% for (Gd**L**^{2})$_3$Eu. The same effect has been observed for dysprosium(III) and terbium(III) complexes. At the concentrations used in the luminescence measurements, the tris complexes partially convert into bis complexes, however, the presence of an extra linker between the aromatic rings in Gd**L**^{2} allows for a larger tris to bis complex ratio, as compared to the Gd**L**^{1} ligand. The lower energy resulting from this linker also lowers the $\pi\pi^*$ excited state of Gd**L**^{2} allowing it to sensitize ytterbium(III) in the solid state. The NMRD profiles of (Gd**L**^{2})$_3$Ln complexes display a characteristic hump between 20 and 100 MHz due to the formation of a supramolecular structure, with enhanced longitudinal relaxivity of up to 25 $s^{-1}mM^{-1}$ per metallostar assembly at 20 MHz and 310 K.

4 Experimental section

General Synthesis of $(GdL^1)_3Ln$. All complexes were synthesized by applying the previously reported procedure[3] and by replacing $EuCl_3$ with appropriate $LnCl_3 \cdot xH_2O$ salt. The complexes have been characterized by TXRF spectrometry, IR and optical spectroscopy.

Synthesis of *tert*-butyl 4-iodobenzylcarbamate (1)

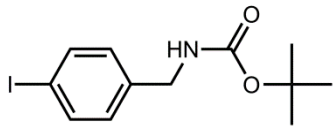

4-Iodobenzylamine (1 eq.; 0.680 g; 2.92 mmol) and triethylamine (1.5 eq.; 4.38 mmol; 0.443 g) is dissolved in 20 ml THF. The solution was cooled in an ice bath and *t*-boc-anhydride (1.5 eq.; 4.38 mmol; 0.955 g) is slowly added. It was allowed to stir overnight at room temperature and the solvent was evaporated. 20 ml of water was added and the product was extracted with EtOAc (3 x 20 ml). The combined organic layer was washed with brine and dried over $MgSO_4$. The solvent was evaporated and yielded a white solid (yield: 0.966 g; 99%). ESI-MS (MeOH, m/z): calcd: 356.17 g/mol $[M+H]^+$, found: 356.6 g/mol $[M+Na]^+$. ^{1}H NMR (300 MHz, $CDCl_3$, δ ppm): 1.45 (s, 9H, *t*-Bu), 4.23 (d, $^3J_{H,H}$ = 5.6 Hz, 2H, NHC**H**$_2$C), 4.87 (broad, 1H, N**H**CH$_2$C), 7.01 (d, $^3J_{H,H}$ = 8.4 Hz, 2H, I-CCHC**H**C), 7.65 (d, $^3J_{H,H}$ = 8.4 Hz, 2H, I-CC**H**CHC). ^{13}C NMR (75 MHz, $CDCl_3$, δ ppm): 28.38; 44.10; 79.71; 92.59; 129.36; 137.62; 138.73; 155.83.

Synthesis of *tert*-butyl 4-((trimethylsilyl)ethynyl)benzylcarbamate (2)

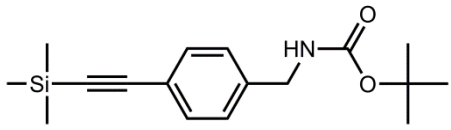

Product (**1**) (1 eq.; 0.966 g; 2.90 mmol), copper(II) iodide (10 mol%; 0.055 g; 0.290 mmol), bis(triphenylphosphine)palladium(II)chloride (5 mol%; 0.101 mg; 0.145 mmol), triethylamine (2 eq.; 0.587 g; 5.80 mmol) were suspended in 10 ml

of dry THF and stirred for 15 minutes under inert atmosphere. (Trimethylsilyl)acetylene (1.2 eq.; 0.118 g; 1.2 mmol) was added and stirred overnight. The solution was diluted with diethylether (50 ml) and the mixture was filtrated over celite. The crude product was purified using silica (eluent = chloroform) and yielded the desired product as an off white solid (yield: 0.704 g; 80%). ESI-MS (MeOH, m/z): calcd: 326.46 g/mol $[M+Na]^+$, found: 326.5 g/mol $[M+Na]^+$. ^{1}H NMR (300 MHz, $CDCl_3$, δ ppm): 0.24 (s, 9H, Si-C**H**$_3$), 1.45 (s, 9H, *t*-Bu), 4.29 (d, $^3J_{H,H}$ = 5.6 Hz, 2H, NHC**H**$_2$C), 4.85 (broad, 1H , N**H**CH$_2$C), 7.20 (d, $^3J_{H,H}$ = 7.6 Hz, 2H, CCHC**H**C), 7.42 (d, $^3J_{H,H}$ = 7.6 Hz, 2H, CC**H**CHC). ^{13}C NMR (75 MHz, $CDCl_3$, δ ppm): 0.37; 28.34; 44.46; 79.68; 94.18; 104.86; 122.11; 127.23; 132.20; 139.43; 155.88.

Synthesis of *tert*-butyl 4-ethynylbenzylcarbamate (3)

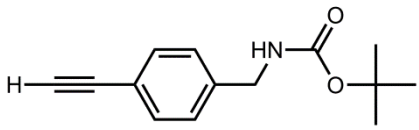

Product (**2**) (1 eq.; 0.671 g; 2.21 mmol) was dissolved into 20 ml THF and cooled to 0 °C. TBAF (1 M) (2 eq.; 4.42 mmol; 4.02 mL) was added and stirred at 0 °C for 1 hour. After the reaction, 50 ml of a water/DCM mixture was added. The organic layer was collected, dried and evaporated. The crude product was purified using silica (eluent = DCM) resulting in a white solid (yield: 0.382 g; 75%). ESI-MS (MeOH, m/z): calcd: 354.28 g/mol $[M+Na]^+$, found: 354.6 g/mol $[M+Na]^+$. ^{1}H NMR (300 MHz, $CDCl_3$, δ ppm): 1.45 (s, 9H, *t*-Bu), 3.1 (s, 1H, CC**H**), 4.30 (d, $^3J_{H,H}$ = 5.9 Hz, 2H, NHC**H**$_2$C), 4.90 (broad, 1H, N**H**CH$_2$C), 7.23 (d, $^3J_{H,H}$ = 8.3 Hz, 2H, CCHC**H**C), 7.44 (d, $^3J_{H,H}$ = 8.3 Hz, 2H, CC**H**CHC). ^{13}C NMR (75 MHz, $CDCl_3$, δ ppm): 28.38; 44.37; 79.70; 83.43; 121.02; 127.1; 127.29; 132.34; 139.84; 155.87.

Synthesis of dimethyl 4-((4-(((*tert*-butoxycarbonyl)amino)methyl)phenyl)ethynyl)pyridine-2,6-dicarboxylate (4)

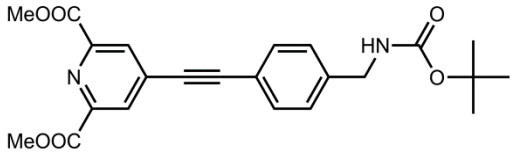

4-Bromopyridine-2,6-dimethylcarboxylate (1 eq.; 0.411 g; 1.50 mmol), CuI (10 mol%, 28.6 mg; 0.15 mmol) and bis(triphenylphosphine)palladium(II) (5 mol%, 52.7 mg; 0.075 mmol) were added to 10 ml dry THF. Triethylamine (2 eq.; 0.304 g; 3.00 mmol) was added and the mixture was allowed to stir for 15 minutes. Product (**3**) (1.1 eq.; 0.382 g; 1.65 mmol) was added and the mixture was stirred for 4 hours at 40 °C. The THF was evaporated, CH_2Cl_2 was added and the suspension was washed with water. The crude product was dissolved in methanol and stirred for 30 minutes. The precipitate was filtered off and dried to obtain the desired product as a light brown solid (yield: 0.535 g; 84%). ESI-MS (MeOH, m/z): calcd: 447.44 g/mol $[M+Na]^+$, found: 447.7 g/mol $[M+Na]^+$. ^{1}H NMR (300 MHz, $CDCl_3$, δ ppm): 1.47 (s, 9H, t-Bu), 4.04 (s, 6H, O**Me**), 4.36 (d, $^3J_{H,H}$ = 6.1 Hz, 2H, NHC**H**$_2$C), 4.92 (broad, 1H, N**H**CH$_2$C), 7.31 (d, $^3J_{H,H}$ = 8.1 Hz, 2H, CCHC**H**C), 7.50 (d, $^3J_{H,H}$ = 8.1 Hz, 2H, CC**H**CHC); 8.36 (s, 2H, C**H**CC≡C). ^{13}C NMR (75 MHz, $CDCl_3$, δ ppm): 28.39; 44.36; 53.33; 79.83; 85.41; 96.79; 120.24; 127.54; 129.65; 132.36; 132.73; 141.15; 148.44; 155.88; 164.75.

Synthesis of dimethyl 4-((4-(aminomethyl)phenyl)ethynyl)pyridine-2,6-dicarboxylate (5)

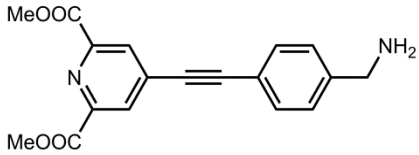

Product (**4**) (1 eq.; 0.212 g; 0.5 mmol) was dissolved in 10 ml of a DCM/TFA (50/50) mixture and stirred for 12 h at room temperature. The solvents were evaporated and 10 ml DCM/MeOH (6/4) was added and evaporated. The crude

product was dissolved in DCM and washed with a saturated aqueous $NaHCO_3$ solution and with brine, then dried over $MgSO_4$ (yield: 0.151 g; 93%). ESI-MS (MeOH, m/z): calcd: 347.32 g/mol $[M+Na]^+$, found: 347.7 g/mol $[M+Na]^+$. ^1H NMR (300 MHz, D_5-pyr, δ ppm): 3.91 (s, 6H, O**Me**), 4.68 (s, 2H, NHC**H**$_2$C), 4.92 (broad, 1H, N**H**CH_2C), 7.72 (d, $^3J_{H,H}$ = 7.9 Hz, 2H, CCHC**H**C), 7.83 (d, $^3J_{H,H}$ = 7.9 Hz, 2H, CC**H**CHC); 8.37 (s, 2H, C**H**CC≡C). ^{13}C NMR (75 MHz, $CDCl_3$, δ ppm): 53.33; 85.24; 97.02; 119.75; 127.38; 129.63; 132.01; 132.14; 132.32; 134.59; 148.40; 164.75.

Synthesis of dimethyl 4-((4-(5-(2-(bis(2-(*tert*-butoxy)-2-oxoethyl)amino)ethyl)-8-(2-(*tert*-butoxy)-2-oxoethyl)-12,12-dimethyl-3,10-dioxo-11-oxa-2,5,8-triazatridecyl)phenyl)ethynyl)pyridine-2,6-dicarboxylate (6)

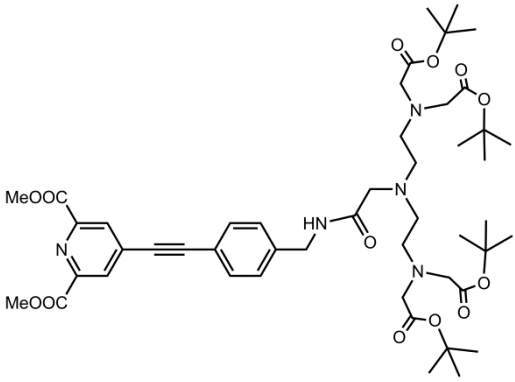

Product (**5**) (1.1 eq.; 0.28 mmol; 0.90 g) was dissolved in 10 mL dry DMF and N,N-diisopropylethylamine (1.5 eq.; 0.38 mmol; 66 µL) was added to the solution. The mixture was stirred for 15 minutes at room temperature under inert atmosphere. At the same time, the DTPA *tert*-butyl ester (1 eq.; 0.25 mmol; 0.156 g), TBTU (1.5 eq.; 0.38 mmol; 0.121 g) and N,N-diisopropylethylamine (1 eq.; 0.25 mmol; 44 µL) were dissolved in 10 mL dry DMF in a three neck flask and stirred for 15 minutes at room temperature under argon atmosphere. The solution from flask 1 was added dropwise over a period of 10 minutes to the three-neck flask 2 and the mixture was stirred at room temperature under argon atmosphere for 24 hours. After evaporation, the residue was redissolved in DCM. The suspension was washed with a saturated aqueous $NaHCO_3$ solution and with brine.

The organic phase was dried with magnesium sulfate and evaporated under reduced pressure. The obtained product was further purified with silica column chromatography (eluent: $CHCl_3$/ 5% MeOH/ 0.66% NH_3) and the collected fractions were evaporated and dried under vacuum at 50 °C, yielding a yellow oil (yield: 0.181 g; 70%). ESI-MS (MeOH, m/z): calcd: 947.08 g/mol $[M+Na]^+$, found: 947.4 g/mol $[M+Na]^+$. ^{1}H NMR (300 MHz, $CDCl_3$, δ ppm): 1.44 (s, 36H, *t*-Bu); 2.64 (t, 4H, NC**H**$_2$CH$_2$N), 2.78 (t, 4H, NCH$_2$C**H**$_2$N), 3.24 (s, 2H, NC**H**$_2$C(O)NH), 3.33 (s, 8H, NC**H**$_2$C(O)O), 4.04 (s, 6H, O**Me**), 4.51 (d, $^3J_{H,H}$ = 6.2 Hz, 2H, NHC**H**$_2$C), 7.38 (d, $^3J_{H,H}$ = 8.2 Hz, 2H, CCHC**H**C), 7.53 (d, $^3J_{H,H}$ = 8.2 Hz, 2H, CC**H**CHC); 8.35 (s, 2H, C**H**CC≡C), 8.88 (broad, 1H, N**H**CH$_2$C). ^{13}C NMR (75 MHz, $CDCl_3$, δ ppm): 28.16; 28.42; 38.61; 42.67; 52.10; 53.32; 53.76; 55.69; 81.09; 85.10; 97.31; 119.65; 128.13; 129.59; 132.13; 134.67; 142.06; 148.43; 164.77; 170.51.

Synthesis of 2,2',2'',2'''-((((2-((4-((2,6-bis(methoxycarbonyl)pyridin-4-yl)ethynyl)benzyl)amino)-2-oxoethyl)azanediyl)bis(ethane-2,1-diyl))bis(azanetriyl))tetraacetic acid (7)

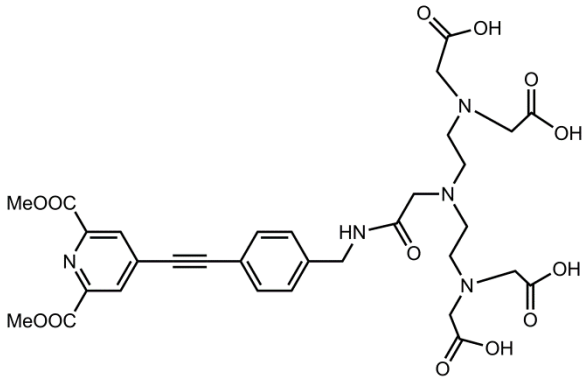

The protected ligand precursor (**6**) (1 eq.; 0.19 mmol; 0.175 g) was dissolved in a 6 M HCl solution and stirred for 1 hour at room temperature under argon atmosphere. The solvent was evaporated, water was added and the solution was evaporated again (2x). The product was redissolved in water and the pH was adjusted from circa 2 to 7 with pyridine. The solvents were evaporated and dried under vacuum at 50 °C as a pale yellow oil (yield: 0.176 mmol; 93%). ^{1}H NMR

(300 MHz, D_5-pyr, δ ppm): 2.64 (t, 4H, NC**H**$_2$CH$_2$N), 2.78 (t, 4H, NCH$_2$C**H**$_2$N), 3.24 (s, 2H, NC**H**$_2$C(O)NH), 3.91 (s, 6H, O**Me**), 4.15 (s, 8H, NC**H**$_2$C(O)O), 4.80 (d, $^3J_{H,H}$ = 6.4 Hz, 2H, NHC**H**$_2$C), 7.57 (d, $^3J_{H,H}$ = 8.3 Hz, 2H, CCHC**H**C), 7.62 (d, $^3J_{H,H}$ = 8.3 Hz, 2H, CC**H**CHC); 8.35 (s, 2H, C**H**CC≡C).

Synthesis of dimethyl 4-azidopyridine-2,6-dicarboxylate (8)

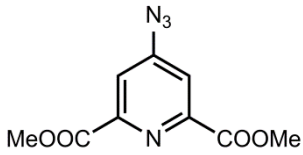

Dimethyl 4-bromopyridine-2,6-dicarboxylate (1 eq.; 1.5 mmol; 0.400 g) was dissolved in 5 mL DMF and NaN_3 (5 eq.; 7.3 mmol; 0.475 g) was added and stirred at 60 °C overnight. After the reaction the solution was added into 75 mL of water under stirring. A white precipitate was formed and collected via filtration (yield: 0.244 g; 71%). EI-MS (MeOH, m/z): calcd: 237.18 g/mol $[M+H]^+$, found: 237 g/mol $[M+H]^+$. ^{1}H NMR (300 MHz, $CDCl_3$, δ ppm): 4.03 (s, 6H, O**Me**), 7.94 (2H, C**H**); ^{13}C NMR (75 MHz, $CDCl_3$, δ ppm): 53.5; 118.1; 149.9, 151.8, 164.5.

Synthesis of dimethyl 4-(4-(4-(((*tert*-butoxycarbonyl)amino)methyl)phenyl)-1H-1,2,3-triazol-1-yl)pyridine-2,6-dicarboxylate (9)

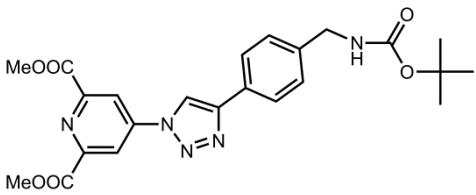

Compound **(8)** (1 eq.; 0.73 mmol; 0.172 g) and compound **(3)** (1 eq.; 0.73 mmol; 0.168 g) were dissolved in dioxane. Copper(II)sulfate (10 mol%) and sodium ascorbate (20 mol%) are dissolved in a small quantity of water and added to the mixture and the solution was kept at 30 °C for 24 h. After evaporation of the solvent, an orange oily liquid is obtained and crystallized from methanol (yield:

0.255 g; 75%). ESI-MS (MeOH, m/z): calcd: 468.47 g/mol $[M+H]^+$, found: 490.6 g/mol $[M+Na]^+$.

Synthesis of dimethyl 4-(4-(4-(aminomethyl)phenyl)-1H-1,2,3-triazol-1-yl)pyridine-2,6-dicarboxylate (10)

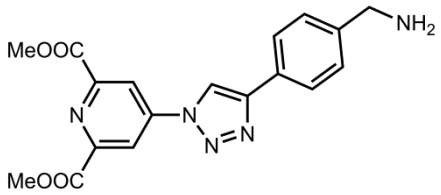

Compound **(8)** (1 eq.; 0.55 mmol; 0.255 g) was dissolved in 10 ml of a DCM/TFA (50/50) mixture and stirred for 12 h at room temperature. The solvents were evaporated and 10 ml DCM/MeOH (6/4) was added and evaporated. The crude product was dissolved in DCM and washed with a saturated aqueous $NaHCO_3$ solution and with brine, then dried over $MgSO_4$ (yield: 0.158 g; 78%). ESI-MS (MeOH, m/z): calcd: 390.47 g/mol $[M+Na]^+$, found: 757 g/mol $[2M+Na]^+$.

Synthesis of dimethyl 4-(4-(4-(5-(2-(bis(2-(*tert*-butoxy)-2-oxoethyl)amino)ethyl)-8-(2-(*tert*-butoxy)-2-oxoethyl)-12,12-dimethyl-3,10-dioxo-11-oxa-2,5,8-triazatridecyl)phenyl)-1H-1,2,3-triazol-1-yl)pyridine-2,6-dicarboxylate (11)

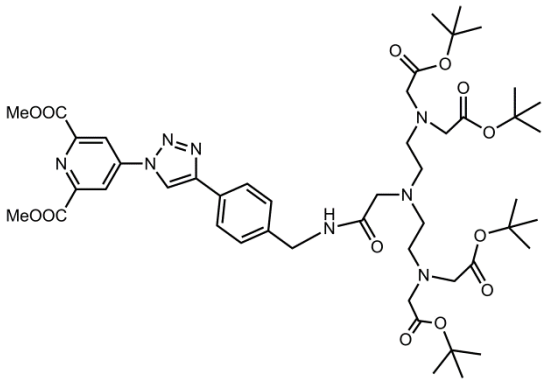

Product **(10)** (1.1 eq.; 0.425 mmol; 0.156 g) was dissolved in 10 mL dry DMF and N,N-diisopropylethylamine (1.2 eq.; 0.464 mmol; 81 µL) was added to the solution. The mixture was stirred for 15 minutes at room temperature under inert atmosphere. At the same time, the DTPA *tert*-butyl ester (1 eq.; 0.25 mmol; 0.156 g), HATU (1.2 eq.; 0.464 mmol; 0.176 g) were dissolved in a three neck flask in 10 mL dry DMF and stirred for 15 minutes at room temperature under argon atmosphere. Synthetic procedure is analogous to compound **(6)** yielding yellow oil (yield: 0.240 g; 64%). ESI-MS (MeOH, m/z): calcd: 968.11 g/mol $[M+H]^+$, found: 991 g/mol $[M+Na]^+$.

Synthesis 2,2',2'',2'''-((((2-((4-(1-(2,6-bis(methoxycarbonyl)pyridin-4-yl)-1H-1,2,3-triazol-4-yl)benzyl)amino)-2-oxoethyl)azanediyl)bis(ethane-2,1-diyl))bis(azanetriyl))tetraacetate (12)

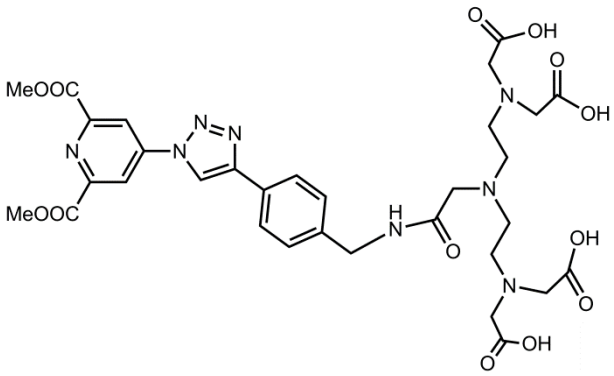

Product **(11)** (1 eq.; 0.284 mmol; 0.240 g) was dissolved in 10 ml of a DCM/TFA (50/50) mixture and stirred for 12 h at room temperature. The solvents were evaporated and 10 ml of DCM/MeOH (6/4) was added and evaporated and the resulting residue was dissolved in pyridine (yield 0.148 g; 70%).

General synthesis of methyl protected Gd$\mathbf{L^x}$

The methyl protected ligand (1 eq.) was dissolved in 5 mL pyridine and the hydrated $GdCl_3$ salt (1.05 eq.) in 0.3 mL water was added to the solution. This mixture was stirred for 3 hours at 70 °C. The solvent was removed under reduced pressure and ethanol was added. The crude product and the suspension was refluxed for 1 hour and filtrated over a P4 glass filter resulting in a pale brown solid. The absence of free lanthanide ions was checked by using an arsenazo indicator.

General synthesis of Gd$\mathbf{L^x}$

The methyl protected Gd$\mathbf{L^x}$ complex (1 eq.) was dissolved in 5 mL of water and K_2CO_3 (2.5 eq.) was added to the solution. The mixture was stirred overnight at room temperature. After the reaction, a pH of about 9 was monitored. The solvent was evaporated, water was added and it was stirred for 30 minutes whereby the pH changed to circa 8. The solvent was removed under reduced pressure and orange flakes were obtained (Gd$\mathbf{L^2}$: 0.11 mmol; 95%; Gd$\mathbf{L^3}$: 0.09 mmol; 55%).

General Synthesis of $\mathbf{(GdL^2)_3Ln}$.

The deprotected ligand Gd$\mathbf{L^2}$ (3 eq.; 51 mg; 0.06 mmol) was dissolved in 3 mL of water. The appropriate $LnCl_3 \cdot xH_2O$ (1.1 eq.; 0.02 mmol) was added and the reaction was kept at 70 °C for 3 hours. The solvent was removed under reduced pressure and ethanol was added. The suspension was refluxed for 1 hour and filtered over a P4 glass filter. The complexes have been characterized by TXRF spectrometry, IR and optical spectroscopy. The IR spectrum of the ligands show a strong absorption in the IR region around 1600 cm^{-1} which corresponds to the C=O bond. After complexation a new peak appears around 1500 cm^{-1}. The Gd/Ln ratio obtained via TXRF spectrometry is the following: 3.0 (Gd/Tb), 3.0 (Gd/Dy), 3.0 (Gd/Eu), 2.9 (Gd/Sm), 2.7 (Gd/Nd), 3.0 (Gd/Yb).

5 References

(1) Debroye, E.; Ceulemans, M.; Vander Elst, L.; Laurent, S.; Muller, R. N.; Parac-Vogt, T. N. *Inorg. Chem.* **2014**, *53* (3), 1257–1259.

(2) Placidi, M. P.; Engelmann, J.; Natrajan, L. S.; Logothetis, N. K.; Angelovski, G. *Chem. Commun.* **2011**, *47* (41), 11534.

(3) Platas-Iglesias, C.; Piguet, C.; André, N.; Bünzli, J.-C. G. *J. Chem. Soc. Dalt. Trans.* **2001**, No. 20, 3084–3091.

(4) Ohe, T.; Miyaura, N.; Suzuki, A. *J. Org. Chem.* **1993**, *58* (8), 2201–2208.

(5) Aebischer, A.; Gumy, F.; Bünzli, J.-C. G. *Phys. Chem. Chem. Phys.* **2009**, *11* (9), 1346.

(6) Onishi, H. *Talanta* **1972**, *19* (4), 473–478.

(7) Gassner, A.-L.; Duhot, C.; G. Bünzli, J.-C.; Chauvin, A.-S. *Inorg. Chem.* **2008**, *47* (17), 7802–7812.

(8) Bünzli, J.-C. G.; Eliseeva, S. V. *Springer Ser. Fluoresc.* **2011**, 1–45.

(9) Beeby, A.; Clarkson, I. M.; Dickins, R. S.; Faulkner, S.; Parker, D.; Royle, L.; de Sousa, A. S.; Williams, J. A. G.; Woods, M. *J. Chem. Soc. Perkin Trans. 2* **1999**, No. 3, 493–504.

(10) Supkowski, R. M.; Horrocks, W. D. *Inorganica Chim. Acta* **2002**, *340*, 44–48.

(11) Moore, E. G. *Dalt. Trans.* **2012**, *41* (17), 5272.

(12) Kimura, T.; Kato, Y. *J. Alloys Compd.* **1998**, *275-277*, 806–810.

(13) Horrocks, W. D.; Sudnick, D. R. *J. Am. Chem. Soc.* **1979**, *101* (2), 334–340.

(14) Debroye, E.; Laurent, S.; Vander Elst, L.; Muller, R. N.; Parac-Vogt, T. N. *Chem. - A Eur. J.* **2013**, *19* (47), 16019–16028.

(15) Harris, M.; Carron, S.; Vander Elst, L.; Laurent, S.; Muller, R. N.; Parac-Vogt, T. N. *Chem. Commun.* **2015**, *51* (14), 2984–2986.

(16) Solomon, I. *Phys. Rev.* **1955**, *99* (2), 559–565.

(17) Bloembergen, N. *J. Chem. Phys.* **1957**, *27* (2), 572.

(18) Freed, J. H. *J. Chem. Phys.* **1978**, *68* (9), 4034.

(19) Botta, M. *Eur. J. Inorg. Chem.* **2000**, *2000* (3), 399–407.

(20) Laurent, S.; Vander Elst, L.; Muller, R. N. *Contrast Media Mol. Imaging* **2006**, *1* (3), 128–137.

CHAPTER 4

T_2 Contrast Agents based on iron oxide nanoparticles functionalized with BODIPY dyes

This chapter is based on a submitted manuscript:

"Luminescent and Relaxometric Properties of BODIPY derivatives covalently bond to iron oxide nanoparticles as potential bimodal contrast agents", Matthias Ceulemans, Maarten Bloemen, Charlotte Verstraete, Bella Manshian, Uwe Himmelreich, Thierry Verbiest, Wim M. De Borggraeve and Tatjana N. Parac-Vogt.

Synthesis and functionalization of the nanoparticles were done by Dr. Maarten Bloemen. Two photon fluorescence imaging was done by Dra. Charlotte Verstraete. Cell viability studies and MRI results were done by Dr. Bella Manshian and Prof. Uwe Himmelreich. BODIPY synthesis and spectroscopic data was recorded by Drs. Matthias Ceulemans.

1 Introduction

Superparamagnetic nanoparticles have attracted a lot of attention due to their unique magnetic properties. For example, iron oxide particles are frequently used in hyperthermia, optical or drug carrier experiments and MRI.[1–5] A well known and frequently used material for MRI are the superparamagnetic iron oxide particles, which induce inhomogeneties in the local magnetic field and make them very efficient T_2 MRI contrast agents.[6] By combination of iron oxides with an organic luminophore, one can obtain a bimodal probe which has a very good spatial resolution and high sensitivity.[7–11]

A class of organic luminophore are BODIPY dyes, which are small organic molecules with generally very high extinction coefficients, fairly sharp fluorescence peaks and high quantum yields.[12,13] BODIPY derivatives were already used in a variety of applications such as electroluminescent devices, tunable laser dyes and fluorescent switches.[14] Their biological applications are found as labels for proteins[15,16] and DNA.[17,18]

The combination of BODIPY derivatives covalently bound to iron oxide particles remains scarce. Few examples are known but they suffer from large size[11] or a low emission wavelength.[10] In this chapter three novel BODIPY derivatives are developed that can be covalently attached to ultrasmall iron oxide nanoparticles via siloxane chemistry. The BODIPY dyes are introduced onto the particles surface during a single functionalization step, thus eliminating post-functionalization procedures. Moreover, it is advantageous that the dye can be embedded into a ligand shell, which is protecting it from the environment and reduces possible adverse effects of experimental conditions. The addition of stabilizing ligands such as siloxane-PEG improves the water dispersibility and biocompatibility of the IO NPs.[19] The convenient synthesis of siloxane coated iron oxide particles as potential bimodal contrast agent for MRI and optical imaging can have broader applicability as the developed procedure provides an efficient and straightforward methodology for grafting different BODIPY derivatives onto a nanoparticle surface in general.[20]

2 Results and discussion

2.1 Ligand design and synthesis

The strategy to synthesize small monodisperse multimodal iron oxide nanoparticles (NPs) is depicted in Scheme 4.1. Oleate capped iron oxide NPs are synthesized according to literature procedure by Park *et al.*[21] The covalent functionalization of these NPs utilizes an optimized synthetic procedure by Bloemen *et al.*[20] The synthetic approach to the BODIPY derivatives is a straightforward two-step reaction, which will lead to the BODIPY core. BODIPY$(CH_2)_2CH{=}CH_2$ (BDP1) was previously reported by Esfandiari *et al.*[22] and was synthesized using a slightly altered method. Reaction of 4-pentenoyl chloride with two equivalents of 2,4-dimethylpyrrole and subsequent complexation with boron trifluoride diethyl etherate gives BDP1 in a good yield (Scheme 4.2). The double bond implemented in the *meso* position of the BODIPY core allows easy covalent attachment to the ultrasmall iron oxide nanoparticles. The emission wavelength of BODIPY derivatives can be tuned by increasing the electron resonance of the core structure. Tissue penetration is a very important factor in choosing the emission wavelength of the luminophore. A good trade-off between image resolution and penetration depth can be made in the region between 665 to 900 nm, the so-called biological window.[23] A selective Knoevenagel condensation of the methyl arms was used to further modify the BODIPY core. Addition of an appropriate aldehyde to BDP1 gave the desired products (BDP2 and BDP3) after a reaction time of only 1 h at 80 °C (Scheme 4.2).

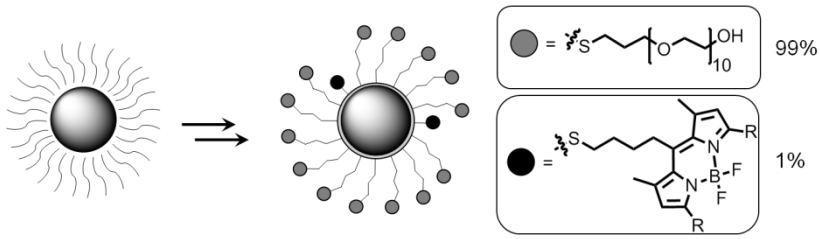

Scheme 4.1. Schematic representation of the synthesized iron oxide NPs. The oleate capped iron oxide NPs were treated with the appropriate ratio of siloxanes to obtain the different NPs: NP-BDP1, NP-BDP2 and NP-BDP3.

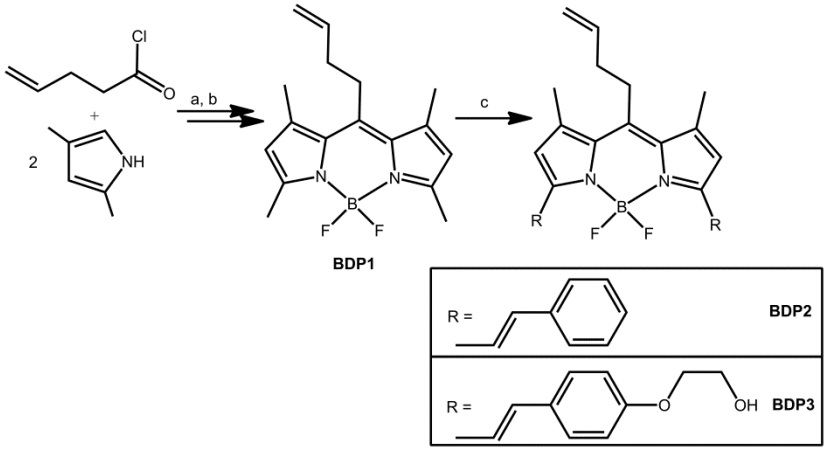

Scheme 4.2. Synthetic pathway to synthesize the desired BODIPY derivatives: a) R.T., 30 min → reflux, overnight b) triethylamine, $BF_3 \cdot Et_2O$, 0 °C, 5 min → R.T., overnight, c) molecular sieves, pyrrolidine, acetic acid, 80 °C, 1 h.

The allyl bond of the BODIPY dye allows for conversion with (3-mercaptopropyl) trimethoxysilane *via* thiolene click chemistry (Scheme 4.3).[24] The final hybrid IO NPs are obtained by reacting BODIPY-siloxane (1%) with a PEG_{10}-siloxane (99%) in presence of a base and the IO NPs. The PEG_{10} chains are used in order to ensure water dispersibility and biocompatibility of the NPs.[24] Using an increased concentration of 5% BODIPY-siloxane to 95% PEG_{10}-siloxane was also attempted, but the final particles were not stable in aqueous solutions, most likely due to the apolar nature of the BODIPY derivative. Therefore, a ratio of 1% was kept for further studies, as a good trade-off between good fluorescence and water dispersibility. Due to the apolar nature of BDP2, the straightforward grafting onto the IO particle has proven to be more difficult as the resulting NPs were not water dispersible. By using 4-(2-hydroxyethoxy)benzaldehyde instead of benzaldehyde, the BODIPY core was made more polar and the resulting BDP3 could easily be grafted onto the surface of NPs resulting in a water dispersible product. Despite the incompatibility of BDP2 with aqueous environments, this derivative was attached to NPs generating a NP-BDP2 hybrid which is dispersible in apolar solvents. Such hybrid could be potentially useful for applications in apolar media, such as polymer blends or for thin film production.

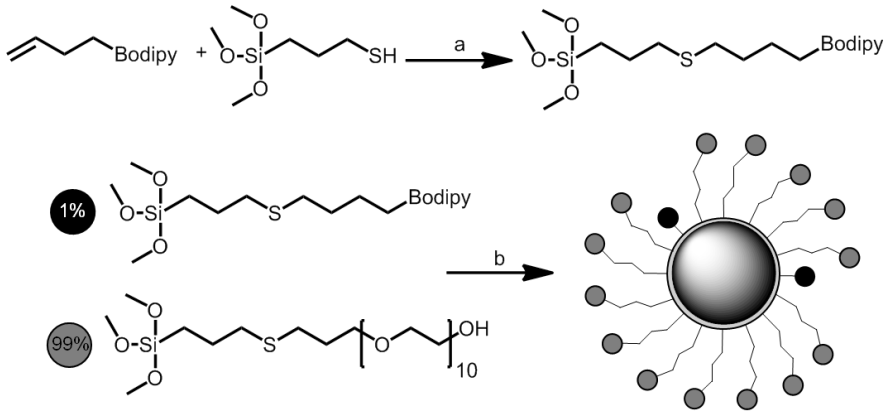

Scheme 4.3. Synthetic procedure for the functionalization of iron oxide NPs. a) 5% 2,2-Dimethoxy-2-phenylacetophenone, chloroform, UV, 0.5-1 h. b) triethylamine, toluene, sonication, 5 h.

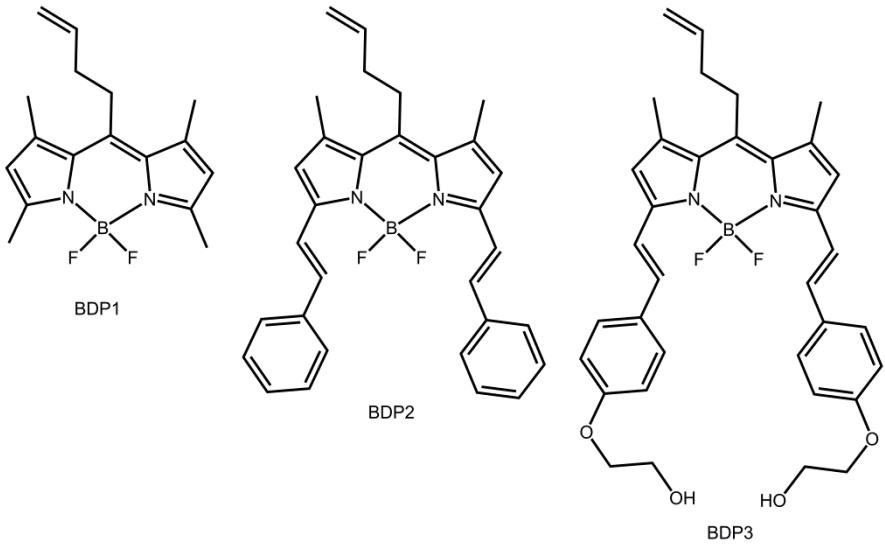

Figure 4.1. An overview of the novel BODIPY derivatives used.

2.2 Photophysical properties

The final obtained BODIPY derivatives are strongly colored solids with a slight metallic luster, which in solution gave a strong fluorescence upon irradiation. The electronic absorption and emission spectra of BDP1, BDP2 and BDP3 are shown in Figure 4.2, and exhibit the characteristic narrow absorption bands. The main absorption bands show maximum λ_{abs}(max) at 502, 618 and 639 nm for BDP1, BDP2 and BDP3 respectively. This visible absorption band is assigned to the $S_0 \rightarrow S_1$ transition. Additional, considerable weaker, broad absorption bands were also observed in the UV-Vis region at ca. 350 nm, and is attributed to the $S_0 \rightarrow S_2$ transition (not shown).[25] Although the absorption spectra show great similarities, the emission patterns are quite different, due to the substituents on the 3 and 5 position of the BODIPY core. The emission maximum λ_{em}(max) of BDP1 was observed at 538 nm, which results in a Stokes shift of 36 nm. The emission spectrum of BDP2 shows two emission maxima at 651 and 690 nm, while the two maxima for BDP3 were observed at 680 and 712 nm. It is therefore evident that introduction of an ethylene glycol moiety into the BODIPY core of BDP3, gives rise to a red shift of 21 nm in comparison with BDP2.

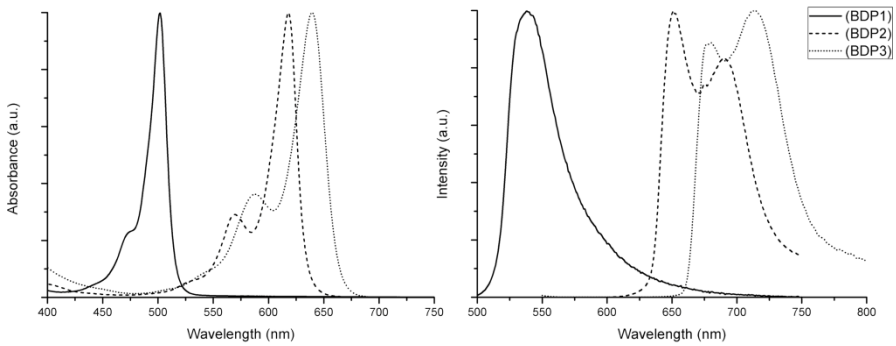

Figure 4.2. Normalized absorbance (left) and emission spectrum (right): BDP1 ($CHCl_3$, λ_{ex} = 480 nm, full line), BDP2 ($CHCl_3$, λ_{ex} = 580 nm, dashed line) and BDP3 ($CHCl_3$, λ_{ex} = 580 nm, dotted line).

The absorbance spectrum of NP-BDP show the distinct exponential curve of Rayleigh scattering as expected from such small particles, but clear absorption maxima can be distinguished (Figure 4.3). The excitation spectra are shown in grey. The absorption maximum λ_{abs}(max) of NP-BDP1 is the same as for the free BDP1 dye and is observed at 502 nm. A shift in λ_{abs}(max) was however observed for NP-BDP2 (from 618 to 515 nm) and NP-BDP3 (from 639 to 518 nm) upon attachment to the NP core. These shifts are most likely result of aggregation of BODIPY derivatives onto the surface of NP due to π-π stacking. Upon excitation at 480 nm the emission maximum λ_{em}(max) of NP-BDP1 was observed at 538 nm. An emission signal was observed for NP-BDP2 at 594 nm with the broad shoulder, while NP-BDP3, exhibited two maxima at 613 and 661 nm, upon excitation at 580 nm. The NP-BDP2 and NP-BDP3 exhibit therefore large Stokes shifts of 78 nm and 95 nm respectively.

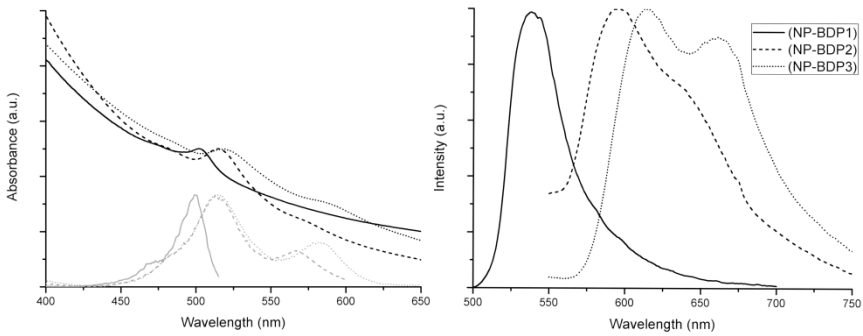

Figure 4.3. Normalized absorbance and excitation (left) and emission spectrum (right): NP-BDP1 (H_2O, λ_{em} = 525 nm, λ_{ex} = 480 nm, full line), NP-BDP2 ($CHCl_3$, λ_{em} = 610 nm, λ_{ex} = 500 nm, dashed line), and NP-BDP3 (H_2O, λ_{em} = 660 nm, λ_{ex} = 500 nm, dotted line).

In addition to one-photon fluorescence, all NP-BDPs also showed interesting characteristics for two-photon fluorescence. Two-photon experiments were carried out by dropcasting the NP-BDPs on a glass plate and visualizing them under a multiphoton microscopy at a fundamental wavelength of 1100 nm and a 15X magnification. NP-BDP3 showed a strong increase in two-photon fluorescence compared to the iron oxide NPs without BODIPY (Figure 4.4). This interesting feature offers potential application for multimodal imaging in addition to MRI. It

has been shown that multiphoton microscopy can be used for *in vivo* experiments with high penetration depths, but the lack of contrast and the difficult administration of fluorophores hampers research.[26] For cancer research, iron oxide NPs can be used to target the tumors, since the particles will automatically accumulate in these cells due to passive targeting.[27] Therefore, NP-BDPs may be suitable for increasing contrast in tumors *in vivo*, which would lead to a reduction of the minimum laser power, thus resulting in less tissue damage.

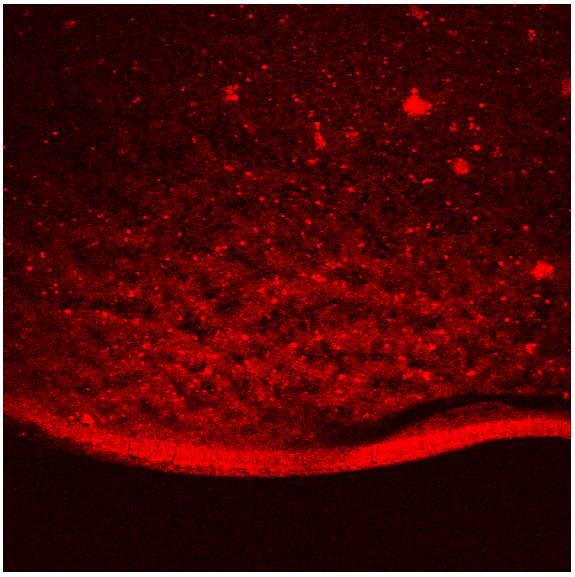

Figure 4.4. Two-photon fluorescence image of NP-BDP3 under a multiphoton microscopy at a fundamental wavelength of 1100 nm and a 15X magnification.

2.3 Relaxivity studies

To assess the relaxivity of the iron oxide nanoparticles different concentrations of nanoparticles were homogenously suspended in an agar phantom (Figure 4.5) and the relaxivity values of the iron oxide nanoparticles were calculated from a parametric map (Table 4.1). A clear increase in relaxivity can be observed at higher concentrations of iron oxide nanoparticles. As expected, the relaxivities r_1 and r_2 of the bare nanoparticles and the functionalized nanoparticles do not differ greatly. Values of r_2 of 52 ± 5 $s^{-1}mM^{-1}$ for the bare NPs and 49 ± 3 $s^{-1}mM^{-1}$, 47 ± 7 $s^{-1}mM^{-1}$ are obtained for NP-BDP1 and NP-BDP3, respectively. Furthermore,

human ovarian cancer (SKOV3) cells were labeled with the NPs to validate the potential to visualize them by MRI. T_2^*-weighted MR images of labeled and unlabeled cells are shown in Figure 4.5. A clear contrast increase is observed in the tube with the labeled cells.

Table 4.1. Relaxivities of iron oxide nanoparticles functionalized without and with BODIPY dyes (NP-BDP1 and NP-BDP3). Relaxivities were determined in agar phantoms using various concentrations of the respective nanoparticles (Figure 4.5) and were calculated from a parametric map.

	r_1 [$s^{-1}mM^{-1}$]	r_2 [$s^{-1}mM^{-1}$]
Bare NP	1.21 ± 0.10	52 ± 5
NP-BDP1	1.12 ± 0.15	49 ± 3
NP-BDP3	1.15 ± 0.10	47 ± 7

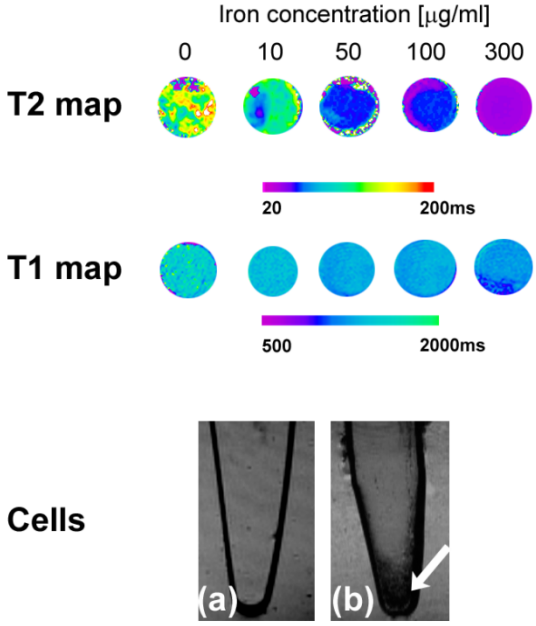

Figure 4.5. Color-coded T_2 and T_1 relaxivities maps of nanoparticles suspended in agar phantoms using various concentrations of nanoparticles. Gray-colored T_2^*-weighted images of (a) unlabeled and (b) labeled human ovarian cancer (SKOV3) cells suspended in agar. The arrow indicates hypo-intense areas in the MRI due to NP-labeled cells. The total amount of cells was 10^5 ml^{-1}.

2.4 Cell viability studies

In order to assess the biocompatibility of the nanoparticles, the toxic effects of the NP-BDP3 particles were assessed with a previously validated high-content image based screening approach,[28] where effects of NPs on cell viability and alterations in cell morphology were evaluated. The data show a clear cell type dependent difference in cytotoxicity from cellular exposure to the NP-BDP3 (Figure 4.5). The rat tumor (AR42J) and human ovarian cancer (SKOV3) cells showed no significant cytotoxicity following exposure to the NPs at any of the tested concentrations. Human hepatic stellate (GRX) cells were only significantly affected by the NPs at the highest concentrations (100 and 200 µg/ml). Contrary to these cell types, human umbilical vein (HUVEC) and rat insulinoma (INS1) cells demonstrated a high sensitivity to the NP-BDP3, with significant cell death noted in both cell types starting from the lower 5 and 10 µg/ml concentrations consecutively. The effects of the NPs in these cells on cellular survival were most drastic at 50 µg/ml concentration and above where cell survival reached down to approximately 50% and lower with the increase in the exposure level.

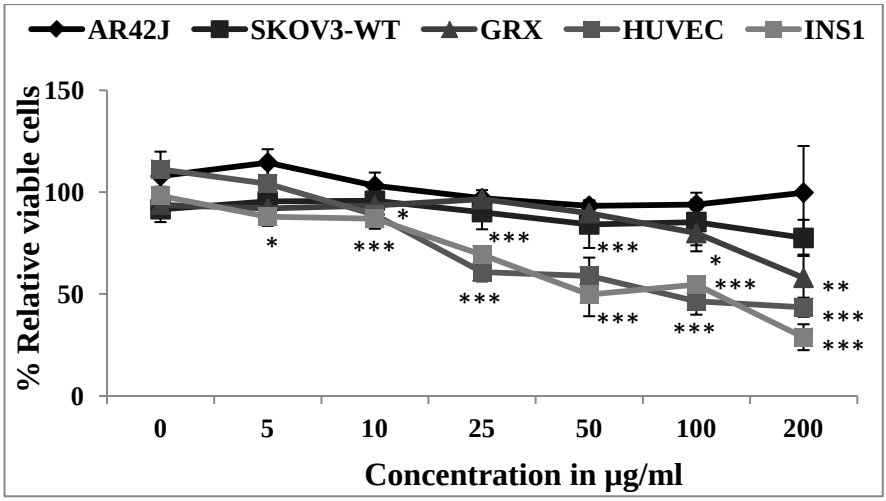

Figure 4.6. Cell viability results of AR42J, SKOV3, GRX, HUVEC, and INS1 cells exposed to various concentrations of NP-BDP3 for 24 h. Results represent quantitative data for the analysis of a minimum of 2000 cells per condition. Quantitative data are presented as mean + SEM (n = 3) for NP-treated cells relative to untreated control cells (± 100%). The degree of statistical significance is shown when appropriate (*: $p < 0.05$, **: $p < 0.01$, ***: $p < 0.001$).

3 Conclusions

In this paper the synthesis and characterization of small monodisperse multimodal iron oxide nanoparticles, functionalized with three types of boron-dipyrromethene (BODIPY) derivatives has been reported. Three BODIPY derivatives, BDP1, BDP2, and BDP3 were covalently attached to iron oxide nanoparticles *via* thiolene click chemistry. All three hybrids showed absorption maxima in the range of 500-540 nm, which could be clearly distinguished within the absorption spectrum dominated by Rayleigh scattering. Upon excitation, bright green and red fluorescence at 538, 594, and 661 nm was observed for NP-BDP1, NP-BDP2, and NP-BDP3 respectively. Interestingly, NP-BDP3 showed a strong increase in two-photon fluorescence compared to the iron oxide NPs with no BODIPY. Relaxivity studies on agar phantoms showed an r_2 value of 49 ± 3 and 47 ± 7 $s^{-1}mM^{-1}$ for NP-BDP1 and NP-BDP3 respectively. Cell viability studies on rat tumor (AR42J) and human ovarian cancer (SKOV3) cells showed no significant cytotoxicity at any of the tested concentrations. Human hepatic stellate (GRX) cells were only significantly affected by the NPs at the highest tested concentrations, 100 and 200 µg/ml.

4 Experimental section

Synthesis of BODIPY$(CH_2)_2CH=CH_2$ (BDP1)

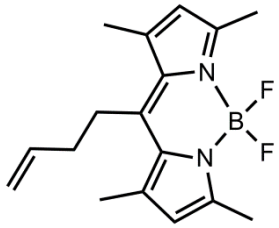

This molecule was synthesized according to an altered synthesis of Esfandiari *et al.*[22] To a solution of 4-pentenoyl chloride (1 eq.; 4.86 mmol; 0.536 mL) in 25 mL dry DCM was added 2,4-dimethylpyrrole (2 eq.; 9.71 mmol; 1 mL). And the solution was stirred for 30 minutes at room temperature. The color changed from yellow to red-brown. Phosphoryl chloride (1.1 eq.; 5.35 mmol; 0.500 mL) was slowly added and the solution was refluxed overnight. The solution was then cooled to 0 °C and triethylamine (10 eq.; 49 mmol; 6.8 mL) was added. After 5 minutes of stirring at 0 °C boron trifluoride diethyl etherate (11 eq.; 53 mmol; 6.6 mL) was slowly added and the solution was stirred at room temperature overnight. Diethyl ether (100 mL) was added to the solution and the organic layer was washed with water (3x 50 mL). The organic layer was dried with $MgSO_4$ and concentrated *in vacuo*. The resulting residue was purified using silica column (eluent: DCM/PET 50:50) yielding an orange solid (yield: 0.639 g, 43%). ESI-MS (MeOH, m/z): calcd: 325.18 g/mol $[M+Na]^+$, found: 325.8 g/mol $[M+Na]^+$. ^1H NMR (400 MHz, $CDCl_3$, δ ppm): 2.34-2.39 (m, 2H), 2.41 (s, 6 H), 2.53 (s, 6H), 3.03-3.07 (m, 2H), 5.09-5.19 (m, 2H), 6.07 (s, 2H); ^{13}C NMR (100 MHz, $CDCl_3$, δ ppm): 14.43, 14.45, 16.28, 27.07, 35.24, 115.62, 121.68, 131.39, 140.41, 145.43, 153.97.

Synthesis of BDP2 (2)

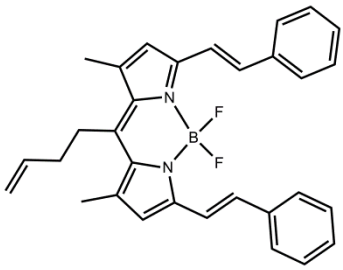

BDP1 (1 eq.; 0.25 mmol; 75 mg) was dissolved in dry ACN (12 mL) under argon atmosphere and 4 Å molecular sieves were quickly added. Then benzylaldehyde (5 eq.; 1.28 mmol; 0.130 mL), pyrrolidine (6 eq.; 1.5 mmol; 0.125 mL) and glacial acetic acid (6 eq.; 1.5 mmol; 0.086 mL) were added under argon atmosphere. The reaction was immersed in a pre-heated 80 °C oil bath and in a few minutes the color turned blue. The reaction was followed with TLC (eluent: DCM/PET 50:50 R_F: 0.43) until full conversion of the starting product, which took about an hour. The mixture was cooled to room temperature and 40 mL DCM/diethyl ether (1:2) was added. The organic layer was washed with a 0.05 M HCl solution (2x 40 mL), saturated $NaHCO_3$ (20 mL), brine (20 mL). The organic layer was dried over $MgSO_4$ and reduced to dryness *in vacuo*. The residue was purified using silica column (eluent: DCM/PET 50:50, R_f = 0.43) yielding a purple solid (yield: 36 mg, 30%). ESI-MS (MeOH, m/z): calcd: 480.38 g/mol $[M+H]^+$, found: 979.4 g/mol $[2M+Na]^+$. ^{1}H NMR (400 MHz, $CDCl_3$, δ ppm): 2.38-2.45 (m, 2H), 2.50 (s, 6 H), 3.10-3.14 (m, 2H), 5.12-5.22 (m, 2H), 5.95-6.01 (m, 1H), 6.74 (s, 2H), 7.28-7.44 (m, 8H), 7.64-7.77 (m, 8H); ^{13}C NMR (100 MHz, $CDCl_3$, δ ppm): 16.6, 27.1, 35.5, 115.7, 118.4, 119.3, 127.5, 128.7, 128.8, 133.3, 135.8, 136.4, 136.7, 139.7, 142.7, 151.5.

Synthesis of BDP3 (3)

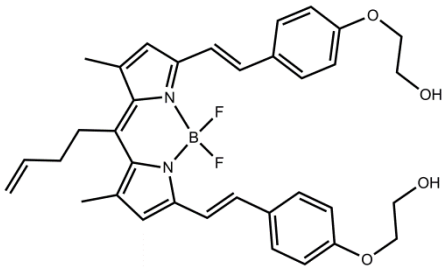

Synthesis of **BDP3** is analogous to **BDP2**, but 4-(2-hydroxyethoxy)benzaldehyde is used. The residue was purified using silica column (eluent: EtOAc, R_f = 0.30) yielding a purple solid (yield: 30 mg, 20%). ESI-MS (MeOH, m/z): calcd: 599.49 g/mol $[M+H]^+$, found: 600.0 g/mol $[M+H]^+$. ^{1}H NMR (400 MHz, $CDCl_3$, δ ppm): 2.39-2.46 (m, 2H), 2.51 (s, 6 H), 3.12-3.16 (m, 2H), 4.00-4.02 (m, 4H), 4.14-4.17 (m, 4H), 5.12-5.23 (m, 2H), 5.94-6.01 (m, 1H), 6.72 (s, 2H), 6.97-7.44 (d, J = 8.7, 4H), 7.20-7.24 (d, 2H), 7.58-7.60 (d, 4H); 7.58-7.63 (d, J = 17, 2H); ^{13}C NMR (100 MHz, $CDCl_3$, δ ppm): 16.6, 27.1, 29.7, 35.6, 61.4, 69.3, 114.9, 115.7, 117.5, 118.1, 129.0, 130.1, 135.2, 136.5, 139.4, 141.7, 151.6, 159.3.

Thiolene click chemistry

To form the siloxane-terminated molecule, an allyl terminated molecule (mixture of allyl-PEG and allyl-BODIPY, total 1 mmol) was mixed with (3-mercaptopropyl) trimethoxysilane (1 eq.; 1 mmol; 185.7 mL) and 2,2-dimethoxy-2-phenylacetophenone (DMPAP, 0.05 eq.; 0.05 mmol; 12.8 mg). This mixture was stirred for 1 hour in a UV chamber, equipped with 3 LEDs (365 nm, output power 200 mW). If smaller quantities are used, a small amount of chloroform can be added to improve the stirring. The product was used without further purification.

Nanoparticle functionalization

The synthesis of iron oxide NP as well as functionalization with siloxanes onto their surface was performed as reported in ref. 20 and is reported here for convenience. In general, 1 mmol of siloxanes is mixed with 100 mg of IONP in 50 mL of toluene. To this mixture 2.5 mL of triethylamine and 50 μL of water are added. The solution was placed in an ultrasonication bath for 5 hours, after which 50 mL of heptane was added to precipitate the particles. Afterwards, they were attracted magnetically and washed 3 times with acetone. Finally the particles were dried in vacuum and dispersed in MilliQ water (with a concentration up to 20 mg/mL).

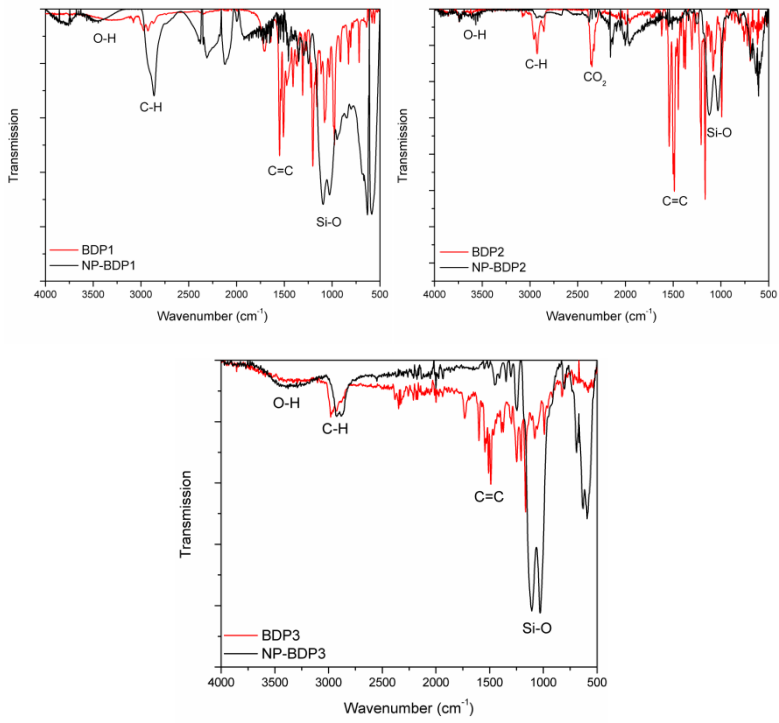

Figure 4.7. IR data of the synthesized BODIPY derivatives (red) and the nanoparticles (black).

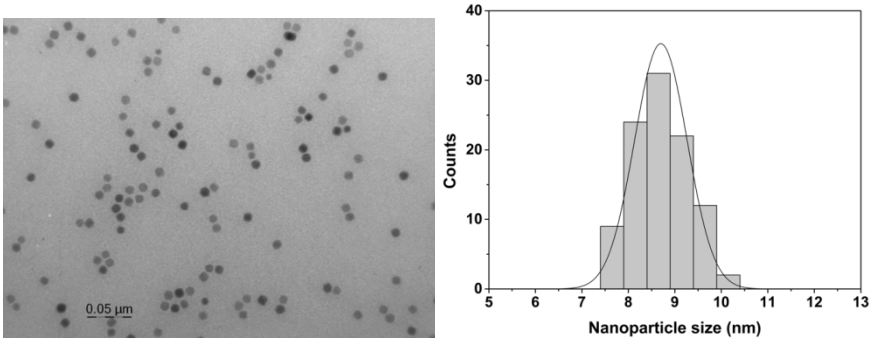

Figure 4.8. TEM image of the oleate capped NPs. The average size is 8.6 ± 0.6 nm.

5 References

(1) Ito, A.; Shinkai, M.; Honda, H.; Kobayashi, T. *J. Biosci. Bioeng.* **2005**, *100* (1), 1–11.

(2) Teja, A. S.; Koh, P.-Y. *Prog. Cryst. Growth Charact. Mater.* **2009**, *55* (1-2), 22–45.

(3) Brullot, W.; Strobbe, R.; Bynens, M.; Bloemen, M.; Demeyer, P.-J.; Vanderlinden, W.; De Feyter, S.; Valev, V. K.; Verbiest, T. *Mater. Lett.* **2014**, *118*, 99–102.

(4) Carron, S.; Bloemen, M.; Vander Elst, L.; Laurent, S.; Verbiest, T.; Parac-Vogt, T. N. *J. Mater. Chem. B* **2015**, *3* (21), 4370–4376.

(5) Carron, S.; Li, Q. Y.; Vander Elst, L.; Muller, R. N.; Capobianco, J. A.; Parac-Vogt, T. N. *Dalt. Trans.* **2015**, *44* (25), 11331–11339.

(6) Laurent, S.; Forge, D.; Port, M.; Roch, A.; Robic, C.; Vander Elst, L.; Muller, R. N. *Chem. Rev.* **2008**, *108* (6), 2064–2110.

(7) Frullano, L.; Meade, T. J. *J. Biol. Inorg. Chem.* **2007**, *12* (7), 939–949.

(8) Louie, A. *Chem. Rev.* **2010**, *110* (5), 3146–3195.

(9) Chekina, N.; Horák, D.; Jendelová, P.; Trchová, M.; Beneš, M. J.; Hrubý, M.; Herynek, V.; Turnovcová, K.; Syková, E. *J. Mater. Chem.* **2011**, *21* (21), 7630.

(10) Topel, S. D.; Topel, Ö.; Bostancıoğlu, R. B.; Koparal, A. T. *Colloids Surfaces B Biointerfaces* **2015**, *128*, 245–253.

(11) Ertem, E.; Bekdemir, A.; Atilgan, A.; Akkaya, E. U. *Pure Appl. Chem.* **2014**, *86* (6).

(12) Loudet, A.; Burgess, K. *Chem. Rev.* **2007**, *107* (11), 4891–4932.

(13) Ulrich, G.; Ziessel, R.; Harriman, A. *Angew. Chemie Int. Ed.* **2008**, *47* (7), 1184–1201.

(14) Boens, N.; Leen, V.; Dehaen, W. *Chem. Soc. Rev.* **2012**, *41* (3), 1130–1172.

(15) Maltas, E.; Kursunlu, A. N.; Arslan, G.; Ozmen, M. *Appl. Surf. Sci.* **2015**, *349*, 811–816.

(16) Murale, D. P.; Hong, S. C.; Yun, J.; Yoon, C. N.; Lee, J.-S. *Chem. Commun.* **2015**, *51* (30), 6643–6646.

(17) Metzeker, M. L. Substitued 4,4-difluoro-4-bora-3A,4A-diaza-s-indacene Compounds for 8-color DNA Sequencing. WO/2003/06681, August 15, 2003.

(18) Dziuba, D.; Pohl, R.; Hocek, M. *Bioconjug. Chem.* **2014**, *25* (11), 1984–1995.

(19) Bruce, I. J.; Sen, T. *Langmuir* **2005**, *21* (15), 7029–7035.

(20) Bloemen, M.; Brullot, W.; Luong, T. T.; Geukens, N.; Gils, A.; Verbiest, T. *J. Nanoparticle Res.* **2012**, *14* (9), 1100.

(21) Park, J.; An, K.; Hwang, Y.; Park, J.-G.; Noh, H.-J.; Kim, J.-Y.; Park, J.-H.; Hwang, N.-M.; Hyeon, T. *Nat. Mater.* **2004**, *3* (12), 891–895.

(22) Esfandiari, N. M.; Wang, Y.; Bass, J. Y.; Blum, S. A. *Inorg. Chem.* **2011**, *50* (19), 9201–9203.

(23) Joshi, B. P.; Wang, T. D. *Cancers* **2010**, *2* (2), 1251–1288.

(24) Bloemen, M.; Van Stappen, T.; Willot, P.; Lammertyn, J.; Koeckelberghs, G.; Geukens, N.; Gils, A.; Verbiest, T. *PLoS One* **2014**, *9* (10), e109475.

(25) Wang, L.; Verbelen, B.; Tonnelé, C.; Beljonne, D.; Lazzaroni, R.; Leen, V.; Dehaen, W.; Boens, N. *Photochem. Photobiol. Sci.* **2013**, *12* (5), 835.
(26) Dunn, K. W.; Sutton, T. A. *ILAR J.* **2008**, *49* (1), 66–77.
(27) Danhier, F.; Feron, O.; Préat, V. *J. Control. Release* **2010**, *148* (2), 135–146.
(28) Manshian, B. B.; Moyano, D. F.; Corthout, N.; Munck, S.; Himmelreich, U.; Rotello, V. M.; Soenen, S. J. *Biomaterials* **2014**, *35* (37), 9941–9950.

CHAPTER 5

Gd-DOTA functionalized with BODIPY dye as a potential T_1 contrast agent

This chapter is based on a manuscript in published in *Inorganics*, 2015, 3, 516-533.

"Gadolinium(III)-DOTA complex functionalized with BODIPY as a potential bimodal contrast agent for MRI and optical imaging", Matthias Ceulemans, Koen Nuyts, Wim M. De Borggraeve, and Tatjana N. Parac-Vogt.

In this chapter the synthesis and characterization of a novel gadolinium(III)-DOTA complex functionalized with a boron-dipyrromethene (BODIPY) derivative is described. The assembly of the luminescent complex relies on azide diazotransfer chemistry in a copper tube flow reactor with subsequent click chemistry. Optimization of the flow reaction was done by Dr. Koen Nuyts and reported in a paper.[1] The synthesis and characterization of the luminescent complex was done by Drs. Matthias Ceulemans. Gratitude goes towards Prof. Koen Binnemans for TXRF measurements and to Prof. Luce Vander Elst of the University of Mons for the relaxometric data.

1 Introduction

As mentioned in previous chapters, a promising class of organic dyes to synthesize bimodal MRI contrast agents are 4,4-difluoro-4-bora-3a,4a-diaza-s-indacene (abbreviated as BODIPY) and its derivatives. This class of organic molecules generally has very high extinction coefficients, fairly sharp fluorescence peaks and high quantum yields. The BODIPY core is fairly stable under physiological conditions and relatively insensitive to the environment. Their emission wavelength is tunable by increasing the resonance within the BODIPY core.[2] The BODIPY dyes have been used in a variety of applications such as biological labels and probes,[3–5] fluorescent probes,[6] laser dyes,[7,8] light emitting diodes,[9] solar cells,[10,11] and potential sensitizers in photodynamic therapy.[12,13]

The first potential bimodal imaging agent for optical and nuclear imaging (PET/CT) consisting of a DOTA ligand and functionalized with a BODIPY compound was reported in 2010 by Bernhard *et al.*[14] In 2012 the same group expanded their compound to a DOTAGA derivative (GA = glutaric acid) which gives more stable complexes with the transition metals.[15] Considering the versatility and favorable optical properties of BODIPY organic dyes, there are surprisingly very few examples of its use as an optical probe in the development of bimodal contrast agents. In previous work primary amines are converted into azides functionalized in a copper tube flow reactor. These azides were used in a subsequent copper mediated cycloaddition using the copper catalyst generated *in situ* from the metallic copper.[1] This chapter further expands this strategy for performing azide-alkyne cycloaddition in order to create a Gd-DOTA-BODIPY derivative. The synthesis and characterization of this novel compound and evaluation of its potential as a bimodal contrast agent for MRI and optical imaging is investigated.

2 Results and Discussion

2.1 Ligand design and synthesis

The main concept used in order to create a Gd-DOTA-BODIPY derivative is based on using click chemistry to couple a BODIPY dye to a DOTA moiety. The resulting bimodal agent with both optical and paramagnetic entities, 5,5-difluoro-1,3,7,9-tetramethyl-10-(2-(4-((2-gadolinium(III)-(4,7,10-tris(carboxylatomethyl)-1,4,7,10-tetraazacyclododecan-1-yl)acetamido)methyl)-1H-1,2,3-triazol-1-yl)ethyl)-5H-dipyrrolo[1,2-c:2',1'-f][1,3,2]diazaborinin-4-ium-5-uide, is presented in Figure 5.1.

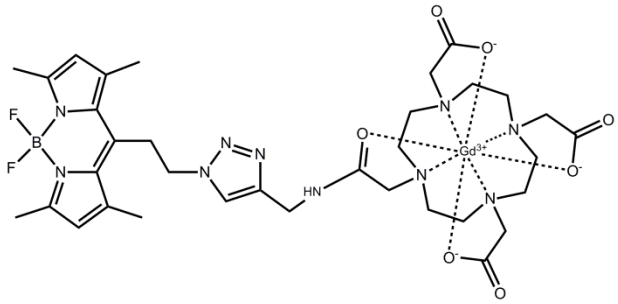

Figure 5.1. The synthesized Gd-DOTA-BODIPY derivative.

The synthesis of the BODIPY core starts with the protection of β-alanine with phthalic acid in solvent free conditions. Subsequent reaction with thionyl chloride converts the acid group into an acid chloride, which can react further with two equivalents of 2,4-dimethylpyrrole to form a dipyrromethene derivative. Complexation of this product with borontrifluoride dietherate and a base forms BODIPY-$(CH_2)_2$-phthalimide. This product can easily be transformed into BODIPY-$(CH_2)_2$-amine by using hydrazine in ethanol, which was clearly demonstrated by the disappearance of the aromatic peaks at 7.77 and 7.88 ppm, and appearance of a new peak at 1.61 ppm in the ^{1}H NMR spectrum (Scheme 5.1). The final BODIPY product contains an amine function which can be transformed in a copper tube into an azide via a diazotranfer reagent (ISA·H_2SO_4) giving BODIPY-$(CH_2)_2$-azide shown in Figure 5.2a.[16,17]

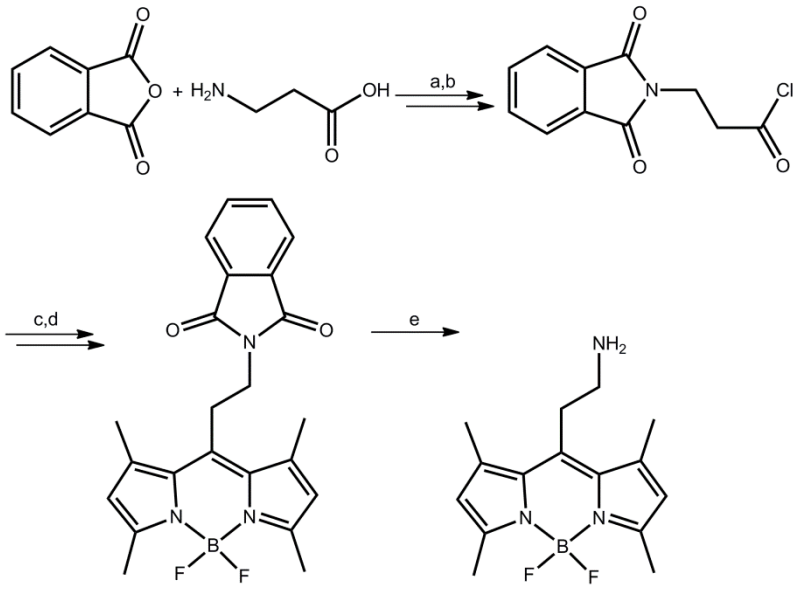

Scheme 5.1. Synthetic procedure for BODIPY-$(CH_2)_2$-amine: a) 160 °C, 6 h; b) $SOCl_2$, reflux, 3 h; c) 2 eq. 2,4-dimethylpyrrole, DCM, 0 °C → reflux, 4 h; d) 10 eq. DIPEA, 11 eq. $BF_3 \cdot Et_2O$, DCM, 0 °C → R.T., overnight; e) $N_2H_4 \cdot H_2O$, EtOH, reflux, 3 h.

The propargylated Ln-DOTA complex (Ln = La(III), Gd(III)) that was used for coupling to BODIPY dye is shown in Figure 5.2b.[18,19] The coupling was performed by using a flow chemistry approach, which can mitigate some safety related issues regarding working with azides.[20] Organic azides can be synthesized from primary amines via a diazotransfer reaction. Trifluoromethanesulfonyl azide is most commonly used as a diazotransfer reagent.[21] The potential short shelf life and highly explosive nature requires careful consideration of the safety issues for their handling.[22] Some safety issues can be circumvented by introduction of imidazole-1-sulfonyl azide (ISA) or its hydrogen sulfate salt ($ISA \cdot H_2SO_4$).[16,23] The flow reaction was performed by mixing solutions of BODIPY-$(CH_2)_2$-amine and $ISA \cdot H_2SO_4$, which is graphically represented in Scheme 5.2. Upon leaving the reactor, the reaction mixture was directly added to a solution of propargylated Ln-DOTA (Ln = La(III) or Gd(III)), resulting in the final product Ln-DOTA-BODIPY.

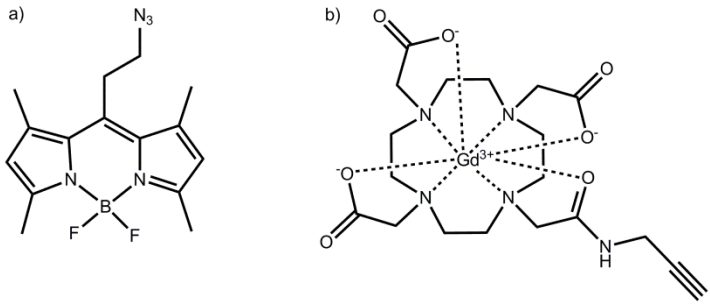

Figure 5.2. a) Structure of BODIPY-$(CH_2)_2$-azide made in a copper tube reactor. b) Structure of propargylated Gd(III)-DOTA complex used to couple to the azide.

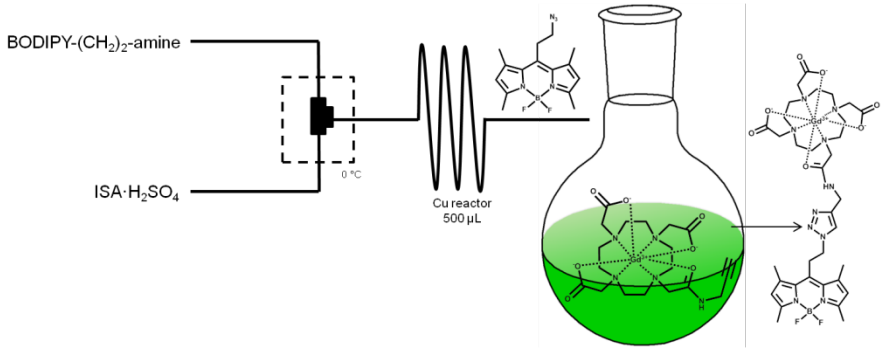

Scheme 5.2. Schematic representation of the flow reactor.

The Ln-DOTA-BODIPY complexes have been isolated, purified and the diamagnetic lanthanum(III) complex La-DOTA-BODIPY has been characterized by ^{1}H NMR spectroscopy in solution (Figure 5.3). The ^{1}H NMR spectrum shows a distinct peak of the triazole proton at 7.55 ppm and two protons on the BODIPY core at 6.00 ppm, indicating a successful linkage of the DOTA moiety with the BODIPY derivative. The ^{1}H NMR spectrum also shows broad peaks in the region from 2.20-3.82 ppm which are typical for the protons in the DOTA ring.[24]

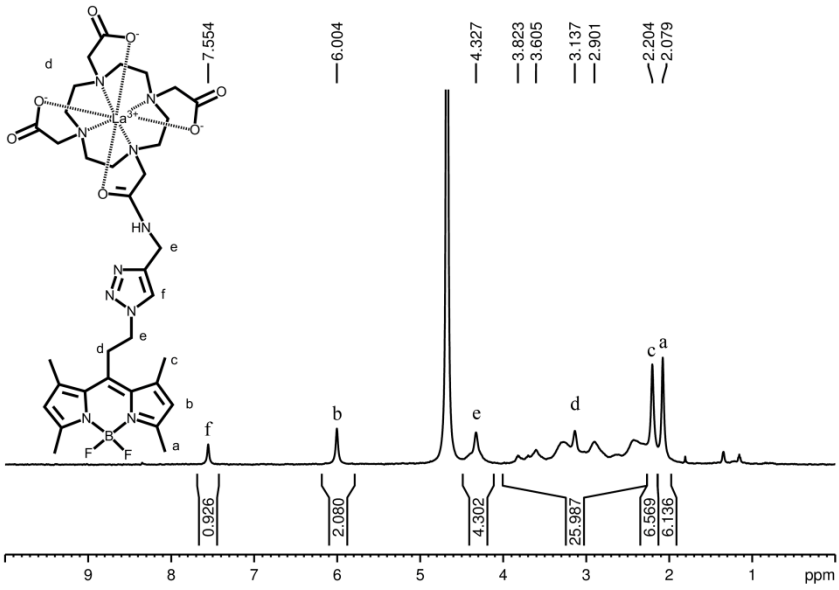

Figure 5.3. ^{1}H NMR spectrum of the final clicked La-DOTA-BODIPY derivative measured in deuterated water. The protons of the triazole ring (7.55 ppm) and of the BODIPY core (6.00 ppm) are clearly visible indicating a successful linkage of the DOTA moiety with the BODIPY derivative.

2.2 Photophysical properties

The solid of this BODIPY derivative is strongly red colored. BODIPY derivatives are apolar in nature and dissolve very well in apolar organic solvents, like chloroform or dichloromethane, and will emit bright green fluorescence. Due to the coupling to hydrophilic Ln-DOTA complex, the final Ln-DOTA-BODIPY adducts are water soluble and give bright green fluorescence in aqueous solution, as is depicted in Figure 5.4, where an aqueous solution of the synthesized Gd-DOTA-BODIPY in the absence and presence of excitation at 366 nm is shown Figure 5.4. Furthermore, the figure shows the electronic spectra of Gd-DOTA-BODIPY and depicts the characteristic and rather narrow absorption and emission bands typical for BODIPY dyes. A main absorption band (dotted line) with a maximum λ_{abs}(max) at 503 nm is observed for Gd-DOTA-BODIPY in aqueous solution. Absorption maxima of 507 and 502 nm were recorded for BODIPY-$(CH_2)_2$-phthalimide and BODIPY-$(CH_2)_2$-amine respectively. The visible absorption bands can be assigned to the $S_0 \rightarrow S_1$ transition.[25] An additional,

considerably weaker broad absorption band is observed in the UV-Vis region around 360 nm, and is attributed to the $S_0 \rightarrow S_2$ transition. It should be noted that the optical properties of the BODIPY dyes can be tuned by increasing conjugation by placing different substituents on the BODIPY core. Such substitutions increase the resonance of the whole structure and provide a red shift of the main emission band, which is favorable for biological applications. A tradeoff between tissue penetration and image resolution for *in vivo* imaging can be made in the optical imaging window (from 665 to 900 nm).[26] In this region the extinction coefficients of the main sources of absorption, hemoglobin, deoxyhemoglobin, and water, are at their minimum. However, it must be taken into account that placing additional substituents on the BODIPY usually renders the system more hydrophobic and decreases the solubility of the entire complex in water. The emission maximum (λ_{ex} = 490 nm, H_2O) of Gd-DOTA-BODIPY is observed at 523 nm, and is in accordance with the previously reported BODIPY derivatives.[27] The excitation maximum (λ_{em} = 570 nm, H_2O) shows a peak at 503 nm. (Figure 5.4)

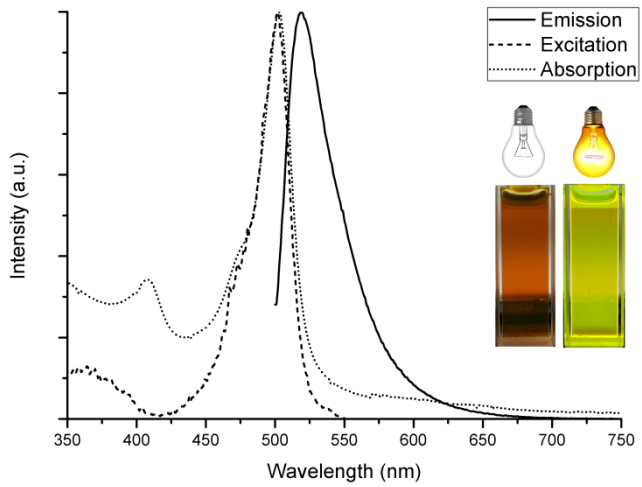

Figure 5.4. Absorption (dotted line), emission (λ_{ex} = 490 nm, black line) and excitation (λ_{em} = 570 nm, dashed line) spectra of Gd-DOTA-BODIPY in water. An aqueous solution of Gd-DOTA-BODIPY in the absence and presence of excitation at 366 nm.

The fluorescent quantum yields Q_L of La-DOTA-BODIPY and Gd-DOTA-BODIPY were determined upon ligand excitation by a comparative method, using a solution of Rhodamine 6G (Q = 78%)[28] in water as the standard. The advantage of BODIPY dyes is that the quantum yields of their derivatives are generally high, even in water.[6] The quantum yield was determined according to the following equation:

$$Q_L = Q_S \cdot \frac{I_X}{I_S} \cdot \frac{A_S(\lambda_{exc})}{A_X(\lambda_{exc})} \cdot \frac{\eta_X^2}{\eta_S^2} \qquad \text{(eq. 5.1)}$$

In this equation the s and x refer to the standard and the unknown sample respectively, I represents the corrected total integrated emission intensity, A the absorbance at the excitation wavelength, η the refractive index of the solution (η_{water} = 1.34) and Q_s the quantum yield of the standard. The samples are diluted until the absorbance at the excitation wavelength is between 0.02–0.05. Quantum yields are recorded with ligand excitation wavelength of 490 nm and gave values of 80% and 83% for La-DOTA-BODIPY and Gd-DOTA-BODIPY respectively.

2.3 Relaxivity measurements

The relaxivity r_1 is the efficiency of a 1 mM solution of gadolinium(III) agent to shorten the longitudinal relaxation time (T_1). According to the Solomon Bloembergen Morgan theory[29,30] several parameters can alter the relaxivity of a contrast agent. High relaxivity can be obtained with a higher amount of water molecules directly bound to the paramagnetic centre (q). Although an easy parameter to adjust, increasing the q value leads to less stable complexes. Other parameters are the distance between gadolinium(III) and water (r), the water residence time (τ_M), the rotational correlation time of the paramagnetic centre (τ_R), the electronic relaxation time of gadolinium(III) at zero field (τ_{S0}) and the correlation time modulating the electronic relaxation (τ_v). The relaxivity of Gd-DOTA-BODIPY derivative measured at frequencies of 20 and 60 MHz at 310 K and was found to be 3.9 and 3.6 $s^{-1}mM^{-1}$ respectively. These values are in close comparison with previously reported values for Gd-DOTA complex, which gave values of 3.5 and 3.1 $s^{-1}mM^{-1}$ at 20 and 60 MHz respectively.[31] A slight increase

compared to the parent Gd-DOTA complex can be attributed to the higher molecular weight of the Gd-DOTA-BODIPY complex, resulting in a slower rotational correlation rate and an overall increase of the relaxivity. The limiting factors for the increase of Gd-DOTA-BODIPY relaxivity are probably the presence of an amide bond in the DOTA scaffold which may slow down the water exchange rate, or flexible linker used for attaching the BODIPY core to the DOTA moiety, which may result in high internal rotations within the Gd-DOTA-BODIPY complex.

3 Conclusions

In this chapter a novel Gd-DOTA-BODIPY derivative is synthesized via a diazotransfer reaction under flow conditions in a copper tube. The complex is water-soluble and exhibits favorable fluorescent properties, thus offering the possibility for the use of BODIPY adducts for *in vivo* optical imaging. A high quantum yield of 83% is obtained in water, and bright emission was observed at 523 nm. Shifting of the emission to the more optimal red-IR region of the spectrum will be attempted in future by increasing the electronic resonance of the BODIPY by adding appropriate substituents to the BODIPY core. The complex exhibits relaxivities which are comparable to the parent Gd-DOTA complex and therefore holds potential as a bimodal contrast agent for MRI and optical imaging.

4 Experimental section

Synthesis of 3-(1,3-dioxoisoindolin-2-yl)propanoic acid (1)

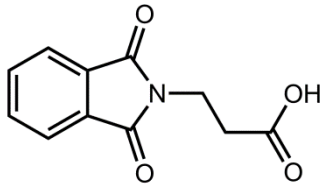

Phthalic anhydride (1 eq.; 40 mmol; 5.92 g) and β-alanine (1 eq.; 40 mmol; 3.56 g) were added in a round bottom flask and heated up to 160 °C for 6 h where it became a smelt. The mixture was cooled and the resulting solid was dissolved in DCM. The solution was washed with 0.1 M HCl (3x 30 mL). The organic layer was dried with $MgSO_4$ and evaporated till dryness as a white solid. (yield: 5.68 g, 25.9 mmol, 65%). CI-MS (MeOH, m/z): calcd: 219.19 g/mol, found: 220.0 g/mol $[M+H]^+$. ^1H NMR (300 MHz, $CDCl_3$, δ ppm): 2.80 (t, J=7.4 Hz, 2H), 4.00 (t, J=7.4 Hz, 2H), 7.74 (m, 2H), 7.84 (m, 2H); ^{13}C NMR (75 MHz, $CDCl_3$, δ ppm): 32.8, 33.4, 123.4, 132.0, 134.1, 168.0, 176.5.

Synthesis of BODIPY-$(CH_2)_2$-phthalimide (2)

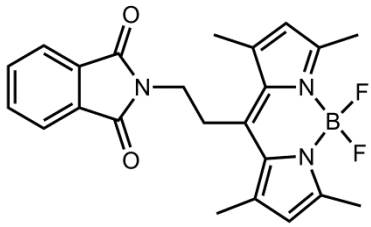

To a round bottom flask product **(1)** (1 eq.; 5 mmol; 1.10 g) and thionyl chloride (5 eq.; 25 mmol; 1.82 mL) were added and refluxed for 3 hours. The thionyl chloride was removed *in vacuo* till dryness. The acid chloride was used further without any purification. The yellow residue was dissolved in 30 mL dry DCM and 2,4-dimethylpyrrole (2 eq.; 10 mmol; 1.04 mL) was slowly added. The solution was stirred for 30 minutes at room temperature. The color changed from

yellow to red-brown. The solution was subsequently refluxed for 4 h. The solution was then cooled to 0 °C and triethylamine (10 eq.; 50 mmol; 6.97 mL) was added. After 5 minutes of stirring at 0 °C boron trifluoride diethyl etherate (11 eq.; 55 mmol; 6.79 mL) was slowly added and the solution was stirred overnight at room temperature. The solution was diluted with diethyl ether (100 mL) and the organic layer was washed with water (3x 50 mL). The organic layer was dried with $MgSO_4$ and concentrated *in vacuo*. The resulting residue was purified using silica column (eluent: DCM/PET 50:50) yielding a dark orange solid (yield: 0.392 g, 0.9 mmol, 19%). CI-MS (MeOH, m/z): calcd: 421.25 g/mol, found: 421 g/mol $[M]^+$. ^{1}H NMR (300 MHz, $CDCl_3$, δ ppm): 2.54 (s, 6H), 2.67 (s, 6H), 3.42 (t, J=8.60 Hz,2H), 3.89 (t, J=8.60 Hz, 2H), 6.11 (s, 2H), 7.77 (m, 2H), 7.88 (m, 2H); ^{13}C NMR (100 MHz, $CDCl_3$, δ ppm): 14.6, 16.4, 27.7, 39.0, 122.2, 123.5, 131.7, 131.9, 134.3, 139.8, 141.5, 154.9, 168.2.

Synthesis of BODIPY-$(CH_2)_2$-amine (3)

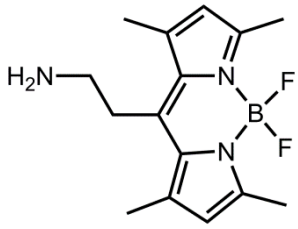

BODIPY-$(CH_2)_2$-phthalimide **(2)** (1 eq.; 0.37 mmol; 158 mg) and hydrazine hydrate (1 eq.; 0.37 mmol; 18.8 mg) in 20 mL ethanol was refluxed for 3 h. After which the solution was cooled to room temperature and filtrated with a Millipore 0.45 µM filter and the solvent was concentrated *in vacuo* as an orange solid (yield: 0.106 g, 0.36 mmol, 97%). CI-MS (MeOH, m/z): calcd: 291.17 g/mol, found: 282 g/mol $[M-F]^+$ and 291 $[M]^+$. ^{1}H NMR (300 MHz, $CDCl_3$, δ ppm): 1.61, (broad, 2H), 2.45 (s, 6H), 2.51 (s, 6H), 2.99 (m, 2H), 3.14 (m, 2H), 6.05 (s, 2H); ^{13}C NMR (100 MHz, $CDCl_3$, δ ppm): 10.5, 12.6, 28.2, 40.1, 117.9, 127.8, 136.6, 138.9, 150.2.

Synthesis of DO3A-*t*Bu (4)

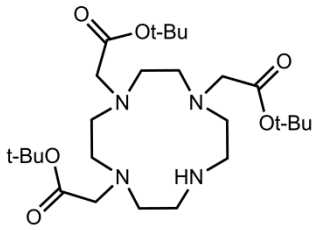

The synthesis uses an altered synthesis by Viguier *et al.*[18] To a solution of tetraazacyclododecane (1 eq.; 5.80 mmol; 1 g), sodium bicarbonate (3.5 eq.; 20.3 mmol; 1.71 g) in 150 mL ACN under an argon atmosphere a solution of *tert*-butyl bromoacetate (3.5 eq.; 20.3 mmol; 3.0 mL) in 50 mL ACN was added drop wise. The mixture was refluxed for 17 h. After removing the salts via filtration over Celite® the solvent was evaporated and the solid was recrystallized from toluene as a white powder (yield: 2.47 g, 4.8 mmol, 82%). ESI-MS: m/z calcd 516 $[M+H]^+$, 538 $[M+Na]^+$, found 516.0 $[M+H]^+$, 537.5 $[M+Na]^+$. ^1H NMR ($CDCl_3$, 300 MHz, δ ppm): 1.46 (s, 27H), 2.88 (t, 12H), 3.08 (t, 4H), 3.30 (s, 2H), 3.38 (s, 4H); ^{13}C NMR ($CDCl_3$, 75 MHz, δ ppm): 28.2, 28.3, 47.5, 49.5, 51.3, 58.1, 81.6, 81.7, 169.8, 170.6.

Synthesis of {4,10-Bis-*tert*-butoxycarbonylmethyl-7-[(2-propynylcarbamoyl)-methyl]-1,4,7,10-tetraaza-cyclododec-1-yl}-acetic acid *tert*-butyl ester (5)

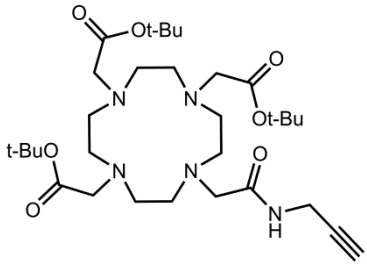

A solution of DO3A-*t*Bu **(4)** (1 eq.; 1.5 mmol; 772 mg), N-(2-propynyl)chloroacetamide (1.2 eq.; 1.8 mmol; 291 mg,) and K_2CO_3 (2 eq.; 3.0 mmol; 415 mg) in 70 mL ACN was stirred under nitrogen at reflux temperature

for 17 h. After filtration of over Celite®, the solvent was removed *in vacuo*, the residual mixture was purified by basic alumina (eluens $CHCl_3$:MeOH (98:2)) to give a colorless solid (yield: 1.45 g, 2.4 mmol, 94%). ESI-MS: m/z calcd 610.80 $[M+H]^+$, found 632 $[M+Na]^+$. ^1H NMR ($CDCl_3$, 300 MHz, δ ppm): 1.45 (s, 18H), 1.46 (s, 9H), 2.15 (t, J=2.3 Hz, 1H), 2.52 (broad, 4H), 2.70 (broad, 4H), 2.82 (broad, 4H), 2.91 (broad, 4H), 3.10 (s, 2H), 3.27 (s, 4H), 3.38 (s, 2H), 4.05 (dd, J=5.5 Hz, J=2.3 Hz, 2H), 9.27 (t, J=5.5 Hz, 1H); ^{13}C NMR ($CDCl_3$, 75 MHz, δ ppm): 28.2, 28.3, 28.6, 29.3, 52.1, 52.5, 53.8, 55.2, 56.2, 57.6, 70.2, 72.9, 80.9, 170.8.

Synthesis of {4,10-Bis-carboxymethyl-7-[(2-propynylcarbamoyl)-methyl]-1,4,7,10-tetraaza-cyclododec-1-yl}-acetic acid (6)

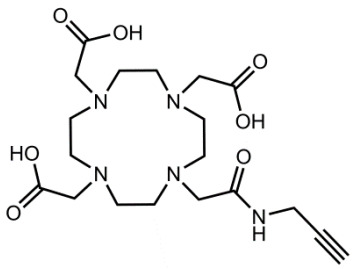

Product **(5)** (1 eq., 1.45 g, 2.4 mmol) was dissolved in 10 mL of a DCM/TFA (50:50) mixture and stirred under inert atmosphere overnight. After the reaction, 20 mL of DCM was added and evaporated (repeated 2 times) (yield: 1.07 g, 2.4 mmol, quantitative). ESI-MS: m/z calcd 442.22 $[M+H]^+$, found 442 $[M+H]^+$, 464 $[M+Na]^+$. ^1H NMR (D_2O, 300 MHz, δ ppm): 2.42 (t, 1H), 2.48-4.01 (broad, 22H), 3.81 (broad, 2H); ^{13}C NMR (D_2O, 75 MHz, δ ppm): 29.1, 29.6, 49.7, 53.7, 58.6, 60.6, 60.8, 69.3, 72.7, 73.5, 78.7, 175.4, 179.4, 179.6.

General procedure for complexation of propargylated DOTA

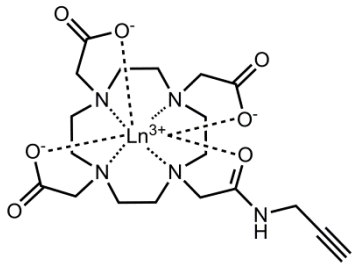

General procedure for complexation of propargylated DOTA: Product **(6)** (1 eq.) was dissolved in 5 mL water and the appropriate lanthanide(III) chloride hydrate (1.1 eq.) was added. The pH was adjusted to 5.5 with a 0.1 M KOH solution and stirred overnight at 60 °C. The solvent was evaporated. The residue was redissolved in 5 mL water and Chelex-100 was added and stirred for 2 h. This last step was repeated till no free lanthanide was found with an Arsenazo III indicator.[32]

Propargylated Gd-DOTA **(7):** (yield: 0.446 g, 0.75 mmol, 67%). ESI-MS: m/z calcd 596.70 $[M+H]^+$, found 619.2 $[M+Na]^+$. IR (neat): $\tilde{\nu}$ = 3416, 3245, 3098, 2873, 1675, 1609 cm^{-1}.

Propargylated La-DOTA **(8)**: (yield: 0.445 g, 0.77 mmol, 65%). ESI-MS: m/z calcd 478.36 $[M+H]^+$, found 600.5 $[M+Na]^+$. ^1H NMR ($CDCl_3$, 300 MHz, δ ppm): 2.42 (t, 1H), 2.48-4.01 (broad, 22H), 3.81 (broad, 2H). ^{13}C NMR ($CDCl_3$, 75 MHz, δ ppm): 29.1, 29.6, 49.7, 53.7, 58.5, 60.6, 60.8, 69.2, 72.7, 73.5, 78.7, 175.4, 179.4, 179.6; IR (neat): $\tilde{\nu}$ = 3429, 3258, 3103, 2857, 1673, 1606 cm^{-1}.

General procedure flow:

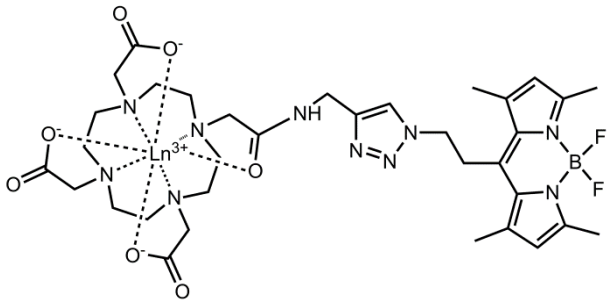

Solution A: a 2 mL solution in a degassed mixture of 10:3:3 MeOH:DCM:H_2O of 1 equivalent BODIPY-amine and 11 equivalents of DIPEA. Solution B: a 2 mL solution of 3 equivalents of ISA·H_2SO_4 in a degassed mixture of 10:3:3 MeOH:DCM:H_2O.

Both solutions in a separate syringe are combined *via* a T-mixer in an ice bath before introducing the mixture to the copper tube flow reactor (150 µL) at room temperature. Flow speed is adjusted so the retention time in the reactor is 300 seconds. The column is stabilized during 3 reactor volumes. Upon leaving the reactor, the reaction mixture was directly added to a solution of 1.5 equivalents of Ln-DOTA-propargyl and 1.5 eq. sodium ascorbate. The mixture is left stirring overnight. The aqueous layer is lyophilized, redissolved in distilled water, purified *via* HPLC and lyophilized. The products are isolated as bright orange powders.

Product **(9)** (Gd-DOTA-BODIPY): (yield: 13 mg, 0.01 mmol, 6%). ESI-MS: m/z calcd 913.85 $[M+H]^+$, found 913.2 $[M+H]^+$. $[Gd^{3+}]$ = 1.454 mmol/l for relaxivity study measured by TXRF against a gallium standard.

Product **(10)** (La-DOTA-BODIPY): (yield: 23 mg, 0.03 mmol, 9%). ESI-MS: m/z calcd 895.51 $[M+H]^+$, found 917.8 $[M+Na]^+$ (positive mode), 894.2 $[M+e]^-$ (negative mode). ^1H NMR (D_2O, 300 MHz, δ ppm): 2.08 (s, 6H), 2.20 (s, 6H), 2.20-3.82 (broad, 26H), 4.33 (broad, H), 6.00 (s, 2H), 7.55 (s, 1H). ^{11}B NMR (D_2O, 80 MHz, δ ppm): 2.16 ppm with respect to $B(OMe)_3$ as reference.

After each reaction the copper tube flow reactor is cleansed in a sonication bath for 10 minutes while introducing a 1:1 mixture of MeOH:triethylamine at 4 mL/min, followed by 20 mL of pentane at 4 mL/min. The reactor is dried with argon and stored under argon.

5 References

(1) Nuyts, K.; Ceulemans, M.; Parac-Vogt, T. N.; Bultynck, G.; De Borggraeve, W. M. *Tetrahedron Lett.* **2015**, *56* (13), 1687–1690.

(2) Ulrich, G.; Ziessel, R.; Harriman, A. *Angew. Chemie Int. Ed.* **2008**, *47* (7), 1184–1201.

(3) Yee, M.; Fas, S. C.; Stohlmeyer, M. M.; Wandless, T. J.; Cimprich, K. A. *J. Biol. Chem.* **2005**, *280* (32), 29053–29059.

(4) West, R.; Panagabko, C.; Atkinson, J. *J. Org. Chem.* **2010**, *75* (9), 2883–2892.

(5) Kowada, T.; Maeda, H.; Kikuchi, K. *Chem. Soc. Rev.* **2015**, *44* (14), 4953–4972.

(6) Boens, N.; Leen, V.; Dehaen, W. *Chem. Soc. Rev.* **2012**, *41* (3), 1130–1172.

(7) García-Moreno, I.; Amat-Guerri, F.; Liras, M.; Costela, A.; Infantes, L.; Sastre, R.; López Arbeloa, F.; Bañuelos Prieto, J.; López Arbeloa, Í. *Adv. Funct. Mater.* **2007**, *17* (16), 3088–3098.

(8) Duran-Sampedro, G.; Agarrabeitia, A. R.; Garcia-Moreno, I.; Costela, A.; Bañuelos, J.; Arbeloa, T.; López Arbeloa, I.; Chiara, J. L.; Ortiz, M. J. *European J. Org. Chem.* **2012**, *2012* (32), 6335–6350.

(9) Lakshmi, V.; Rajeswara Rao, M.; Ravikanth, M. *Org. Biomol. Chem.* **2015**, *13* (9), 2501–2517.

(10) Bessette, A.; Hanan, G. S. *Chem. Soc. Rev.* **2014**, *43* (10), 3342.

(11) Singh, S. P.; Gayathri, T. *European J. Org. Chem.* **2014**, *2014* (22), 4689–4707.

(12) González-Béjar, M.; Liras, M.; Francés-Soriano, L.; Voliani, V.; Herranz-Pérez, V.; Duran-Moreno, M.; Garcia-Verdugo, J. M.; Alarcon, E. I.; Scaiano, J. C.; Pérez-Prieto, J. *J. Mater. Chem. B* **2014**, *2* (28), 4554.

(13) Lim, S. H.; Thivierge, C.; Nowak-Sliwinska, P.; Han, J.; van den Bergh, H.; Wagnières, G.; Burgess, K.; Lee, H. B. *J. Med. Chem.* **2010**, *53* (7), 2865–2874.

(14) Bernhard, C.; Goze, C.; Rousselin, Y.; Denat, F. *Chem. Commun.* **2010**, *46* (43), 8267.

(15) Bernhard, C.; Moreau, M.; Lhenry, D.; Goze, C.; Boschetti, F.; Rousselin, Y.; Brunotte, F.; Denat, F. *Chem. - A Eur. J.* **2012**, *18* (25), 7834–7841.

(16) Fischer, N.; Goddard-Borger, E. D.; Greiner, R.; Klapötke, T. M.; Skelton, B. W.; Stierstorfer, J. *J. Org. Chem.* **2012**, *77* (4), 1760–1764.

(17) Hansen, A. M.; Sewell, A. L.; Pedersen, R. H.; Long, D.-L.; Gadegaard, N.; Marquez, R. *Tetrahedron* **2013**, *69* (39), 8527–8533.

(18) Viguier, R. F. H.; Hulme, A. N. *J. Am. Chem. Soc.* **2006**, *128* (35), 11370–11371.

(19) Verwilst, P.; Eliseeva, S. V.; Carron, S.; Vander Elst, L.; Burtea, C.; Dehaen, G.; Laurent, S.; Binnemans, K.; Muller, R. N.; Parac-Vogt, T. N.; De Borggraeve, W. M. *Eur. J. Inorg. Chem.* **2011**, *2011* (24), 3577–3585.

(20) Hessel, V.; Kralisch, D.; Kockmann, N.; Noël, T.; Wang, Q. *ChemSusChem* **2013**, *6* (5), 746–789.

(21) Bräse, S.; Baner, K. *Organic Azides: Syntheses and Applications*; John Wiley & Sons: Chichester, 2010.

(22) Johansson, H.; Pedersen, D. S. *European J. Org. Chem.* **2012**, *2012* (23), 4267–4281.
(23) Goddard-Borger, E. D.; Stick, R. V. *Org. Lett.* **2007**, *9* (19), 3797–3800.
(24) Duimstra, J. A.; Femia, F. J.; Meade, T. J. *J. Am. Chem. Soc.* **2005**, *127* (37), 12847–12855.
(25) Wang, L.; Verbelen, B.; Tonnelé, C.; Beljonne, D.; Lazzaroni, R.; Leen, V.; Dehaen, W.; Boens, N. *Photochem. Photobiol. Sci.* **2013**, *12* (5), 835.
(26) Kobayashi, H.; Ogawa, M.; Alford, R.; Choyke, P. L.; Urano, Y. *Chem. Rev.* **2010**, *110* (5), 2620–2640.
(27) Niu, S.; Ulrich, G.; Ziessel, R.; Kiss, A.; Renard, P.-Y.; Romieu, A. *Org. Lett.* **2009**, *11* (10), 2049–2052.
(28) Olmsted, J. *J. Phys. Chem.* **1979**, *83* (20), 2581–2584.
(29) Solomon, I. *Phys. Rev.* **1955**, *99* (2), 559–565.
(30) Bloembergen, N. *J. Chem. Phys.* **1957**, *27* (2), 572.
(31) Laurent, S.; Vander Elst, L.; Muller, R. N. *Contrast Media Mol. Imaging* **2006**, *1* (3), 128–137.
(32) Onishi, H. *Talanta* **1972**, *19* (4), 473–478.

CHAPTER 6

Towards T_1 contrast agents *via* copper mediated cycloaddition

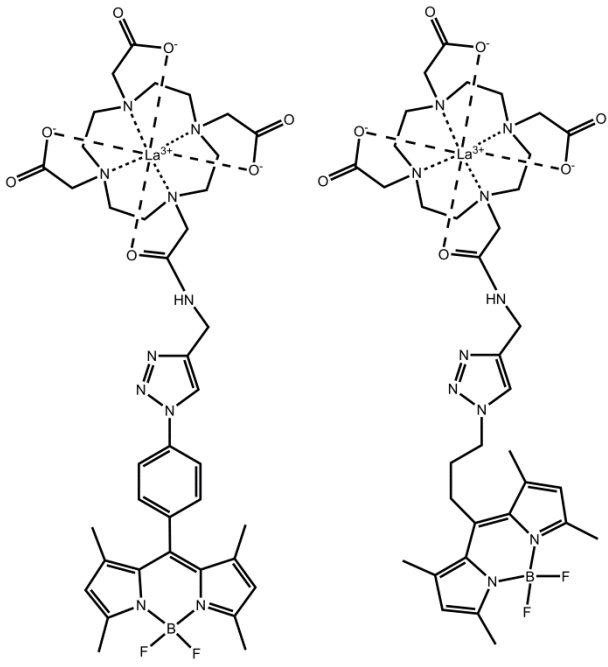

Ligand design, synthesis and characterization of the luminescent complexes were done by Drs. Matthias Ceulemans. Gratitude goes towards Prof. Koen Binnemans for TXRF measurements.

1 Introduction

Magnetic resonance imaging (MRI) as a diagnostic tool has grown over the past years.[1–6] Gadolinium(III) chelates have some interesting properties that efficiently induce relaxation of water molecules.[1] In modern molecular imaging techniques the commonly used contrast agents are the acyclic diethylenetriaminepentaacetic acid (Gd-DTPA) and the cyclic 1,4,7,10-tetraazacyclododecane-1,4,7,10-tetraacetic acid (Gd-DOTA).[2] The eight-fold coordination ensures stability (log K = 22.5 and 25.3 for Gd-DTPA and Gd-DOTA respectively), and allows the binding of one water molecule directly to the metal center.[7–9] MRI suffers from a low sensitivity; on the contrary, optical imaging (OI) is a very sensitive technique. Combination of both MRI and OI into one probe would allow images to reveal more details, ensure the same biodistribution and reduce the stress imposed on the body than using two separate probes. For the design of *in vivo* probes tissue penetration is a very important factor when deciding which fluorophores to use. A good trade-off between the image resolution and penetration depth can be made in the region between 665 to 900 nm.[10] BODIPY dyes are a class of small organic molecules with very high extinction coefficients, fairly sharp fluorescence peaks and high quantum yields. Their emission wavelength is tunable by increasing the resonance within the BODIPY core.[11]

Although BODIPY dyes were known since the late 1960s, it was only in the 1990s that the true versatility of these dyes were fully recognized.[12] The first publication reporting on successful linkage of a DOTA moiety with a BODIPY derivative was published by Bernhard *et al.*[13] The goal is to develop a potential bimodal imaging agent for optical and nuclear imaging (PET/CT). So far no reports of the use of BODIPY-DOTA derivatives used for optical and magnetic resonance imaging are known. In this chapter different synthetic procedures are highlighted in order to couple DOTA to BODIPY dyes. The general ligand design consists of suitable BODIPY dyes preparation in order to covalently bind them to a DOTA moiety by a modular approach.

2 Results and discussion

2.1 Ligand design and synthesis

The first approach to obtain an optical and MRI probe uses the coupling between free acid and free amine group to form a stable amide bond. In a second approach a copper mediated cycloadditon was used in order to synthesize a BODIPY derivative with a La-DOTA complex.

2.1.1 DOTA-BODIPY via coupling reagents

Ligand design and synthesis

In the first approach we attempted to synthesize the potential bimodal contrast via coupling using peptide synthesis (Scheme 6.1). With this approach a carboxylic acid and an amine can be coupled with coupling agents such as TBTU or HATU. We opted for the approach in which an acid group on DOTA would be coupled to an amine on BODIPY, due to available expertise within the group.

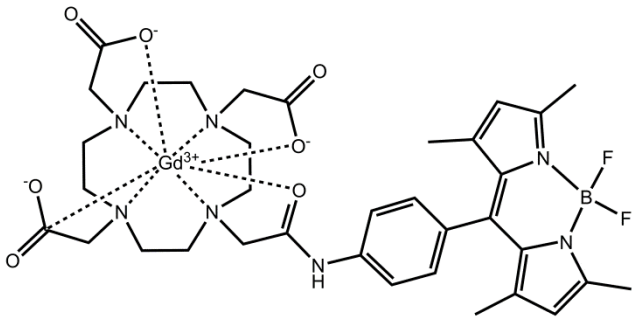

Scheme 6.1. The structure of the final targeted potential bimodal MRI contrast agent.

The synthetic strategy behind a single acid group containing DOTA ligand is straightforward. Three amine functionalities of cyclen are selectively substituted with *tert*-butyl bromoacetic acid as shown in Scheme 6.2. To ensure formation of DO3A-*t*Bu, 3.5 equivalents of *tert*-butyl bromoacetate were used. A purification step is required to separate the desired product DO3A-*t*Bu from the undesired byproduct DOTA-*t*Bu. At first, column chromatography with basic alumina was

used, but separation of the two products was not satisfactory and impure, off-white solids were obtained. Simple crystallization from toluene lead to pure DO3A-*t*Bu as a white solid. The fourth amine of DO3A-*t*Bu was substituted with benzyl bromoacetate and subsequent hydrogenation over Pd/C and hydrogen gas, either *via* a Parr shaker or under atmospheric pressure, lead to a free carboxylic acid derivative in high yields.

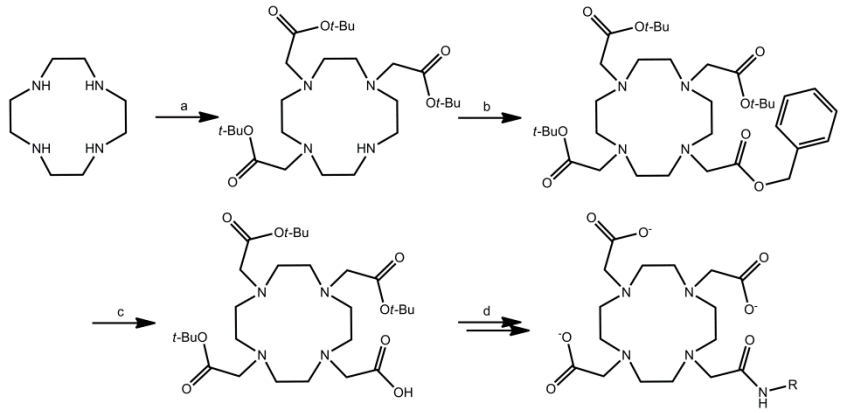

Scheme 6.2. Synthetic pathway for a free acid containing DOTA derivative. : a) 3.5 eq. *tert*-butyl bromoacetate, $NaHCO_3$, ACN, reflux, overnight; b) benzyl bromoacetate, K_2CO_3, ACN, reflux, overnight; c) Pd/C (5%), H_2, 4 h, Parr shaker; d) amide formation.

The *meso* position of the BODIPY core was used to bear an amine function, because this position makes it easy to prepare desired derivatives with readily available starting materials. In a first approach, benzyl carbamate (Cbz) protected amine was used to build up the BODIPY core, because these groups are easily removed via hydrogenation and should protect the amine from nucleophilic attacks. During acyl chloride formation, only a five membered ring is observed when 5-(carbobenzoxyamino)valeric acid was used (Scheme 6.3).

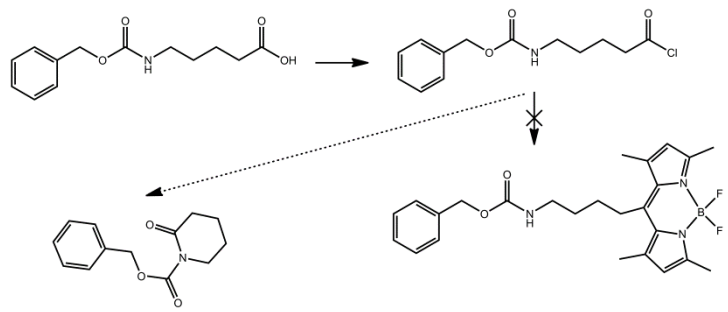

Scheme 6.3. Synthetic strategy to form a Cbz-protected BODIPY. Only a six membered ring is formed.

In a second approach an aniline group is introduced on the *meso* position of the BODIPY core. The synthetic procedure starts from 4-nitrobenzoic acid or 4-nitrobenzaldehyde. Conversion of 4-nitrobenzoic acid into an acyl chloride with thionyl chloride and subsequent reaction with two equivalents of 2,4-dimethylpyrrole forms a *meso* nitrophenyl-dipyrromethene. The same product is formed in a one-pot synthesis by reacting 4-nitrobenzaldehyde with two equivalents of 2,4-dimethylpyrrole in the presence of an acid catalyst, followed by reaction by a mild oxidant such as *p*-chloranil. The *meso* nitrophenyl-dipyrromethene is subsequently complexed with boron trifluoride diethyl etherate ($BF_3 \cdot Et_2O$) and a triethylamine as base to form the bright green emissive BODIPY 8-nitrophenyl derivative (Scheme 6.4).

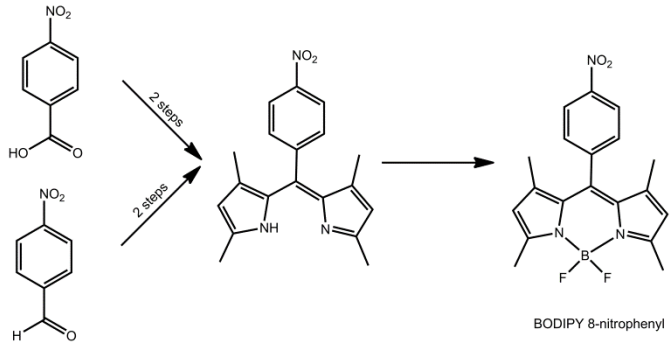

Scheme 6.4. Two synthetic pathways to form *meso* nitrophenyl-dipyrromethene. Complexation with boron trifluoride diethyl etherate and a base leads to the bright green emissive BODIPY 8-nitrophenyl.

Two methods are explored to reduce the nitro function to an amine: Pd/C catalyzed hydrogenation with H_2 or reduction with hydrazine. The first method has been proven to be much slower than the second. Boiling BODIPY 8-nitrophenyl, hydrazine, and a catalytic amount of palladium (5%) on carbon in ethanol for two hours and filtration leads to the desired product in good yields (Scheme 6.5).

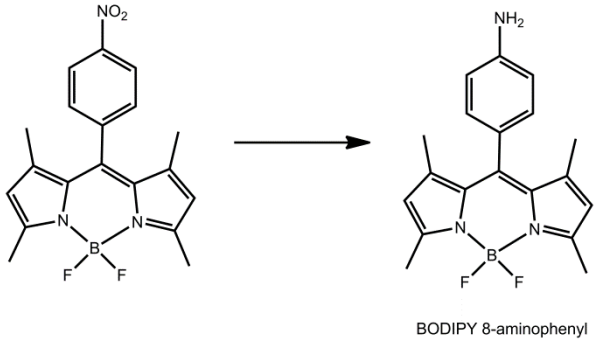

Scheme 6.5. Synthesis of BODIPY 8-aminophenyl: 5 eq. H_4N_2, cat. Pd (5%)/C, EtOH, reflux, 2 h.

The aniline of BODIPY 8-aminophenyl was used in a coupling reaction with the free acid containing DOTA derivative. To facilitate the reaction by activating the carboxylic acid group, several coupling reagents were used: 1-[bis(dimethylamino)methylene]-1H-1,2,3-triazolo[4,5-b]pyridinium-3-oxid-hexafluorophosphate (HATU) and dicyclohexylcarbodiimide (DCC) with N-hydroxysuccinimide (NHS). Unfortunately all the coupling reactions resulted in impure samples that were collected after alumina column purification.

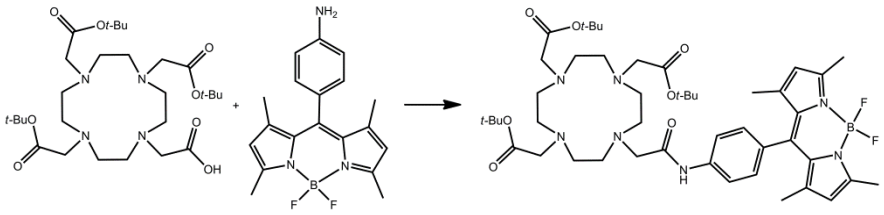

Scheme 6.6. BODIPY 8-aminophenyl in a coupling reaction with the free acid containing DOTA derivative using coupling reagents forming the desired fully protected BODIPY derivative.

To achieve the better separation of the byproducts another approach was attempted. In this method the BODIPY 8-aminophenyl was alkylated with bromoacetyl bromide prior to a substitution reaction with the amine of DO3A-*t*Bu. The nucleophilic substitution was done as a first attempt under reflux conditions in DMF with K_2CO_3 as a base. Destruction of the BODIPY complex was observed after this overnight reaction. In a second approach lower temperatures were used to complete the reaction. Strong bases such as sodium hydride at 0 °C can be used to deprotonate the amine leading to a very reactive nucleophile. An easy extraction step resulted in the desired product which was characterized by means of ESI-MS and NMR.

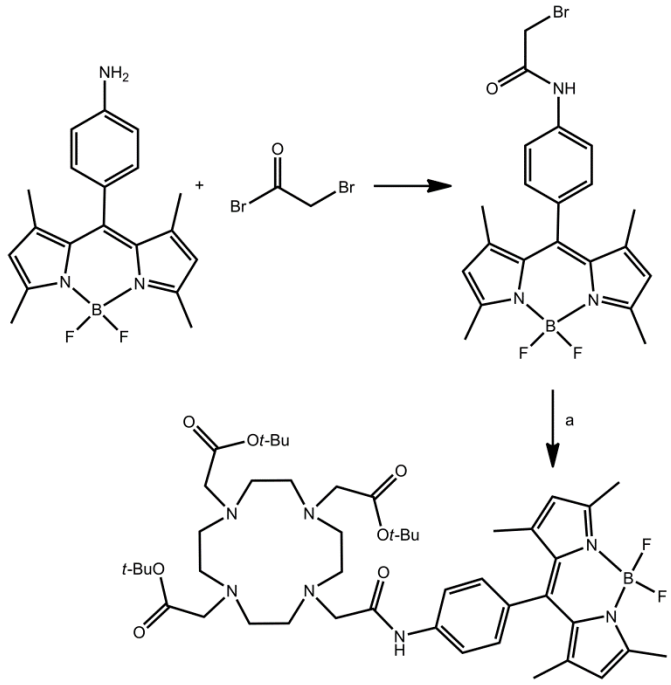

Scheme 6.7. Acylation with subsequent nucleophilic substitution yields a protected BODIPY derivative. A) DO3A-*t*Bu, NaH, 0 °C.

The ^{1}H NMR spectrum of the acylated BODIPY 8-aminophenyl shows the amide proton at 8.20 ppm, two doublets (J = 8 Hz) at 7.20 and 7.64 ppm, assigned to the aromatic protons, a distinct peak of the BODIPY core at 5.94 ppm and the methyl protons at 2.54 and 1.39 ppm. The singlet at 3.99 ppm is assigned to the protons next to the bromine (Figure 6.1).

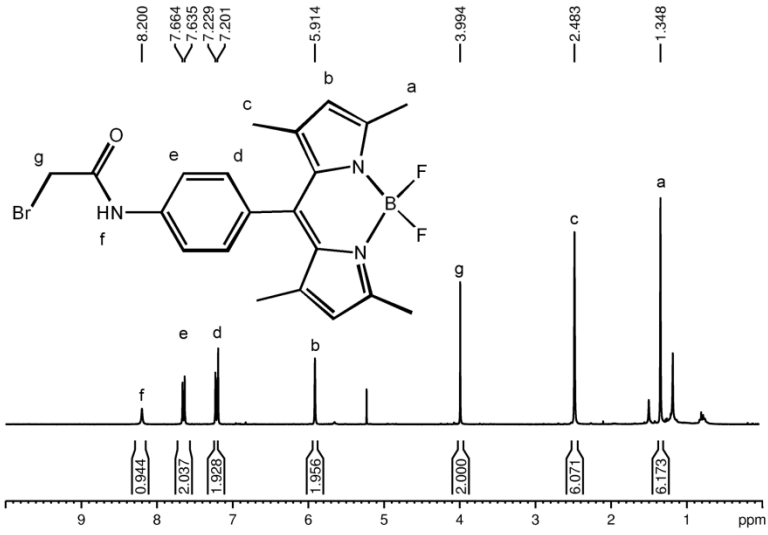

Figure 6.1. ^{1}H NMR spectrum of the acylated BODIPY 8-aminophenyl.

In the final product the large peak at 1.44 ppm is assigned to the *t*-Bu groups and the observed broad bands between 2.58–3.42 ppm to the ring protons of the DOTA moiety.[14] The BODIPY peaks are found in the final product and are shifted: the two aromatic doublets (J = 8 Hz) at 7.14 and 8.02 ppm, two protons of the BODIPY core at 5.94 ppm and the methyl protons at 2.54 and 1.39 ppm. The singlet at 3.99 ppm is shifted towards lower values (Figure 6.2). Deprotection and subsequent complexation were further performed in order to obtain the final desired potential bimodal probe, however the BODIPY derivative was destroyed during the deprotection step.

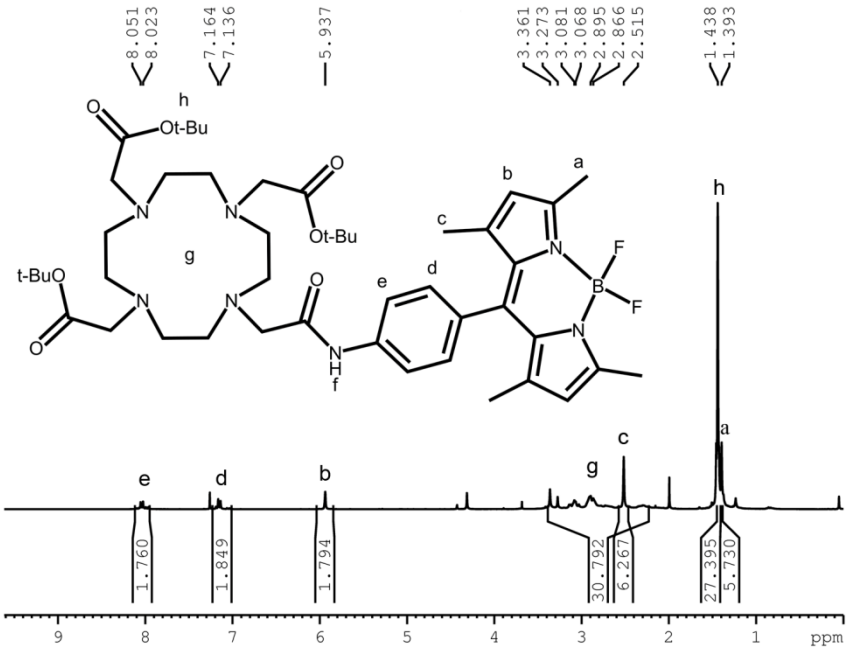

Figure 6.2. ^{1}H NMR spectrum of the BODIPY derivative.

2.1.2 DOTA-BODIPY via copper mediated cycloaddition

Ligand design and synthesis

The second approach used copper mediated cycloaddition which led to the formation of azide containing BODIPYs. Commercially available BODIPY derivatives BODIPY 8-chloromethane and BODIPY 8-bromomethane were first considered for this approach. As prices for these dyes are considerably large (1120 USD/100 mg)[15] the option to synthesize these derivatives from the readily available and cheap bromoacetyl bromide or chloroacetyl chloride was chosen. The final products can be made in a simple one-pot two-step reaction (Scheme 8). Attempts were made to substitute the halogen with sodium azide, but no substitution was found. Also in literature no examples are found of this type of reaction.

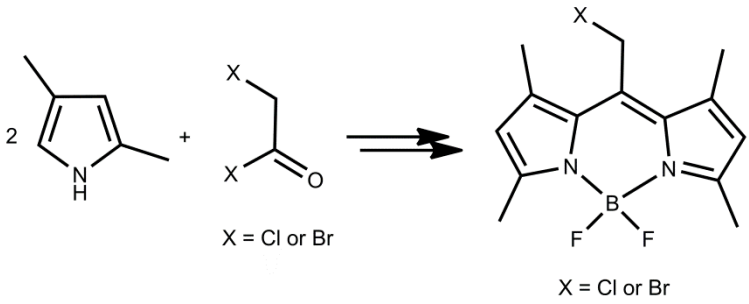

Scheme 6.8. The synthetic pathway of BODIPY 8-chloromethane and BODIPY 8-bromomethane. A simple two step reaction leads to the desired products.

In a second approach two BODIPY azides were reproduced from known reaction pathways from literature and are depicted in figure 6.3.[16,17] The BODIPY-Ph-N_3 is synthesized from the BODIPY 8-aminophenyl derivative, where *via* a diazonium compound the azide was substituted in a one pot synthesis. BODIPY-$(CH_2)_3$-N_3 was obtained via a substitution reaction of BODIPY-$(CH_2)_3$-Cl which was obtained by using 4-chlorobutyryl chloride and 2 equivalents of 2,4-dimethylpyrrole followed by complexation with $BF_3 \cdot Et_2O$ and a base. These azide containing BODIPY derivates are used in copper mediated cycloaddition with the propargylated DOTA complex, as discussed in previous chapter (Figure 4). The DOTA moiety should be chelated with a lanthanide ion prior the copper mediated cycloaddition, as the copper catalyst used will form strong complexes with the DOTA derivative.

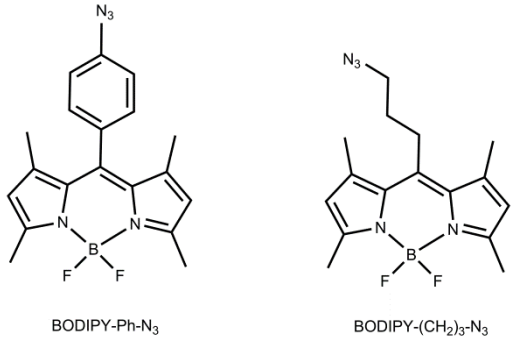

Figure 6.3. BODIPY azide derivatives from literature used in the copper mediated cycloaddition.

In the copper mediated cycloaddition the azides were mixed with the propargylated La-DOTA complex in combination with copper sulphate and sodium ascorbate, which will generate the active Cu(I) species. The desired products were collected after an HPLC purification and analyzed using NMR in solution.

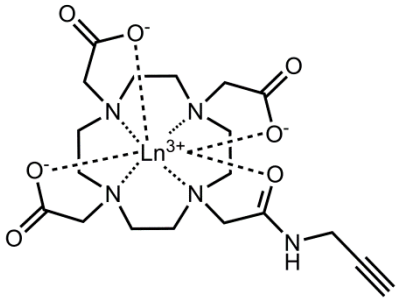

Figure 6.4. Structure of the propargylated Ln-DOTA (Ln = La(III)) derivative.

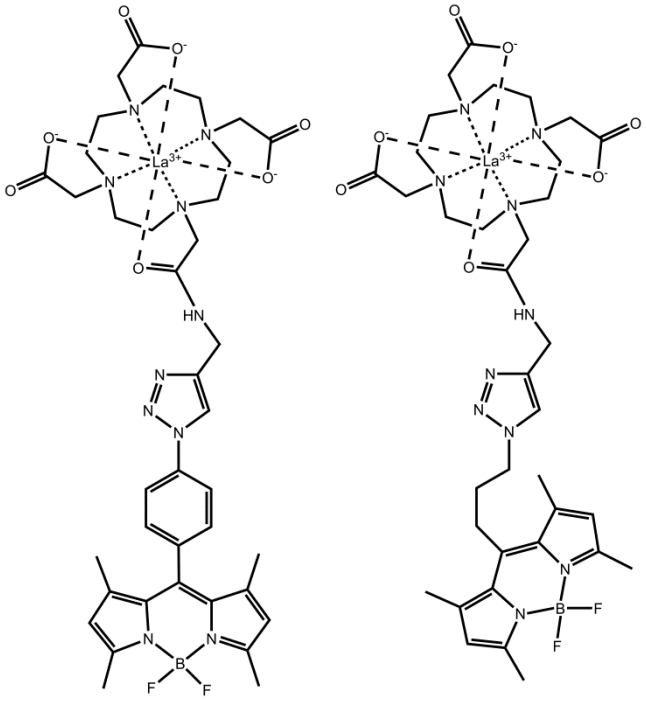

Figure 6.5. Molecular structures of the synthesized La-DOTA-BDP4 (left) and La-DOTA-BDP5 (right) *via* a copper mediated cycloaddition.

No clear NMR data could be recorded for La-DOTA-BDP4, but the HPLC trace of the purified product suggests the formation of the final product with a molecular mass of 941.2 g/mol (see Experimental section).

The ^{1}H NMR spectrum of La-DOTA-BDP5 shows a distinct peak of the triazole proton at 7.77 ppm and two protons on the BODIPY core at 5.99 ppm, indicating a successful linkage of the DOTA moiety with the BODIPY derivative. The ^{1}H NMR spectrum also shows broad peaks in the region from 2.20-3.82 ppm which are typical for the protons in the DOTA ring.[14] The formation of the final product can also be seen in the HPLC trace (see Experimental section).

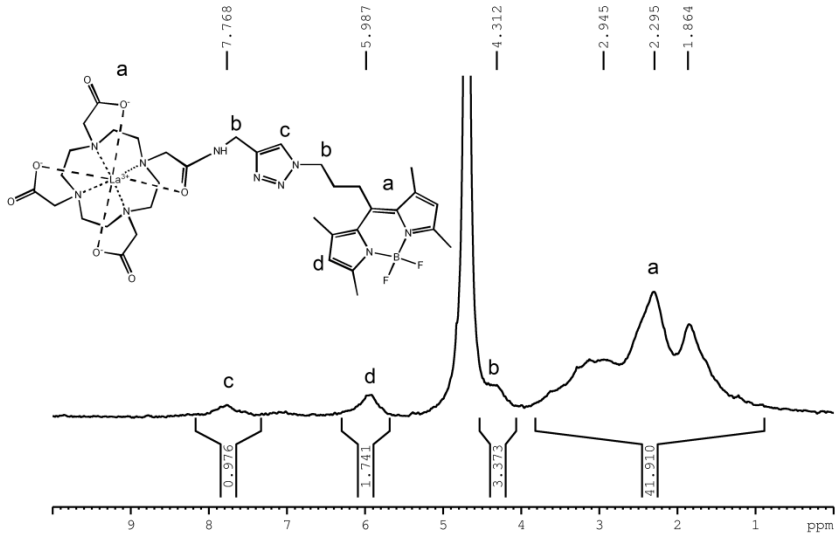

Figure 6.6. ^{1}H NMR spectrum of La-DOTA-BDP5 measured in D_2O.

Photophysical properties

The final BODIPY derivatives are water soluble due to the linkage of the polar La-DOTA complex. The electronic absorption spectra shown in figure 6.7 depict characteristic and rather narrow absorption bands typical for BODIPY dyes. Both absorption patterns are similar which would be expected for the same BODIPY core. The main absorption band with a maximum λ_{abs}(max) at 496 and 499 nm are observed in aqueous solution for La-DOTA-BDP4 and La-DOTA-BDP5 respectively. An additional, considerably weaker broad absorption band is observed in the UV-Vis region around 350 nm. The solutions emit a green fluorescence upon excitation. A shift in the optical properties of the BODIPY dyes can easily be tuned by increasing conjugation by placing different substituents on the BODIPY core. The BODIPY core is very apolar and dissolves well in apolar organic solvents. When altering the BODIPY core, water solubility must be taken into account.

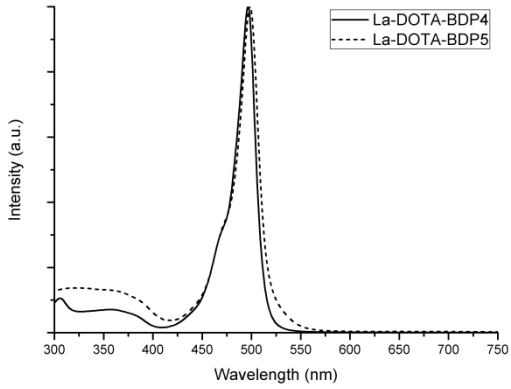

Figure 6.7. The absorption spectra of La-DOTA-BDP4 (full line) and La-DOTA-BDP5 (dashed line).

The emission maxima of La-DOTA-BDP4 and La-DOTA-BDP5 are observed at 508 and 510 nm respectively (Figure 6.8). The excitation maximum, measured at an emission wavelength of 525 nm, shows a maximum at 497 nm and has a similar shape to the absorption maximum.

The fluorescent quantum yields of La-DOTA-BDP4 and La-DOTA-BDP5 were determined upon ligand excitation (490 nm) by a comparative method, using a solution of Rhodamine 6G (Q = 78%)[18] in water as the standard. QY values of 39% and 64% were recorded respectively. The QY of La-DOTA-BDP4 is lower than expected. Energy transfer towards the phenyl ring from the BODIPY core could be an explanation. No relaxometric data was obtained as no gadolinium(III) derivatives were synthesized. The relaxivity of both complexes could be assumed to be in the range of previously reported values for Gd-DOTA complexes, which is 3.5 and 3.1 $s^{-1}mM^{-1}$ at 20 and 60 MHz respectively.[19]

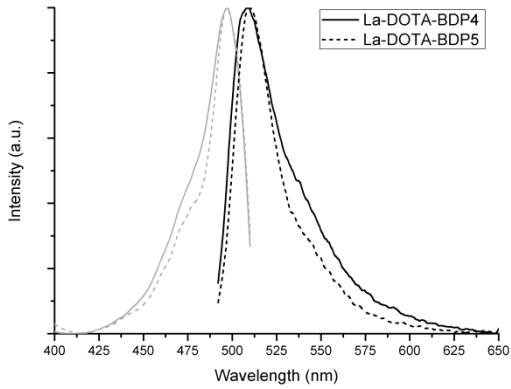

Figure 6.8. Emission (black, λ_{ex} = 490 nm) and excitation (grey, λ_{em} = 525 nm) spectrum of La-DOTA-BDP4 (solid line) and La-DOTA-BDP5 (dashed line).

3 Conclusions

In this chapter an attempt to synthesize a novel Gd-DOTA-BODIPY derivative was described. Unfortunately, the final product could not be obtained as the BODIPY core was destroyed during the deprotection in a final step. The synthesis and characterization of two novel BODIPY derivatives, La-DOTA-BDP4 and La-DOTA-BDP5, is also highlighted in this chapter. The complexes are water-soluble and exhibit good fluorescent properties. Upon ligand excitation in water a bright emission was observed at 508 and 510 nm with an observed quantum yield of 39% and 64% for La-DOTA-BDP4 and La-DOTA-BDP5 respectively. In the future an emission shift to the more optimal red-IR region of the spectrum can be attempted by increasing the electronic resonance of the BODIPY by adding appropriate substituents to the BODIPY core. Gadolinium(III) containing derivatives should be synthesized to measure the relaxometric properties. Due to the similar size, it is expected that the relaxivity of these compounds will be in the range of previously reported values for Gd-DOTA complexes.

4 Experimental section

Synthesis of DO3A-*t*Bu (1)

The synthesis was written in a previous chapter.

Synthesis of tri-*tert*-butyl 2,2',2''-(10-(2-(benzyloxy)-2-oxoethyl)-1,4,7,10-tetraazacyclododecane-1,4,7-triyl)triacetate (2)

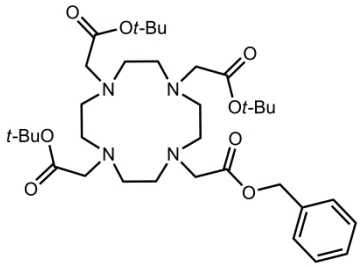

To a suspension of DO3A-*t*Bu **(1)** (1 eq.; 1.0 mmol; 0.535 g) and K_2CO_3 (3 eq.; 3.0 mmol; 0.431 g) in 100 mL acetonitrile was a 50 mL solution dropwise added of benzyl bromoacetate (1.1 eq.; 1.1 mmol; 0.262 g) in ACN. The resulting suspension was refluxed overnight after which the salts were removed *via* filtration over Celite® and the solvent was concentrated *in vacuo*. The oily residue was further purified *via* column chromatography, basic alumina (eluent: DCM:MeOH 98:2), to a colorless oil (yield: 0.398, 60%). ESI-MS: m/z calcd: 663.86 g/mol $[M+H]^+$, found: 686 g/mol $[M+Na]^+$. ^1H NMR ($CDCl_3$, 300 MHz, δ ppm): 1.45 (s, 27H), 2.82 (m, 16H), 3.29 (m, 6H), 3.47 (s, 2H), 5.15 (s, 2H), 7.33 (m, 5H); ^{13}C NMR ($CDCl_3$, 75 MHz, δ ppm): 27.9, 27.9, 28.0, 55.0, 55.2, 55.6, 55.8, 66.9, 67.0, 81.9, 128.4, 128.6, 128.7, 135.1, 173.0, 173.1, 173.6, 173.7.

Synthesis of 2-(4,7,10-tris(2-(*tert*-butoxy)-2-oxoethyl)-1,4,7,10-tetraazacyclododecan-1-yl)acetic acid (3)

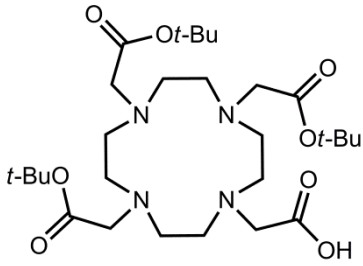

Product **(2)** (1 eq.; 0.53 mmol; 0.350 g) was dissolved in 10 mL MeOH and 10 mol% of palladium (5%) on carbon was added. The suspension was put under hydrogen atmosphere in a Parr shaker for 4 hours. The catalyst was filtered off with a Millipore FH 0.45 µm filter and concentrated and a colorless oil was obtained. (yield: 0.296 g, quantitative). ESI-MS (MeOH, m/z): calcd: 573.73 g/mol $[M+H]^+$, found: 596 g/mol $[M+Na]^+$. ^{1}H NMR ($CDCl_3$, 300 MHz, δ ppm): 1.46 (s, 27H), 1.9-3.58 (very broad, 24H); ^{13}C NMR ($CDCl_3$, 75 MHz, δ ppm): 27.9, 28.1, 55.5, 55.9, 56.1, 82.2, 172.4, 174.7.

Synthesis of BODIPY 8-nitrophenyl (4)

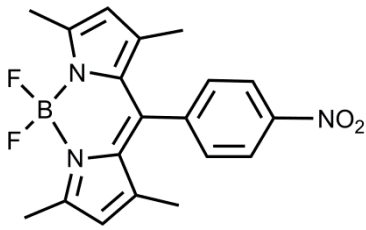

To a solution of 4-nitrobenzaldehyde (1 eq.; 5.0 mmol; 0.756 mg) in 25 mL of DCM was added 2,4-dimethylpyrrole (2 eq.; 10 mmol; 1.04 mL) and two drops of trifluoroacetic acid. The solution was stirred for 1 h and *p*-chloranil (1 eq.; 5 mmol; 1.23 g) was added. The mixture was allowed to stir for an additional 2 hours. The solution was then cooled to 0 °C and triethylamine (10 eq.; 50 mmol; 6.94 mL) was added. After 5 minutes of stirring at 0 °C boron trifluoride diethyl etherate (11 eq.; 55 mmol; 7.56 mL) was slowly added and the solution was stirred

at room temperature overnight. The solution was diluted with diethyl ether (200 mL) and the organic layer was washed with water (3x 75 mL). The organic layer was dried with $MgSO_4$ and concentrated *in vacuo*. The resulting residue was purified using silica column (eluent: DCM/PET 1:1) yielding a red solid (yield: 0.320 g, 17%). ^{1}H NMR (300 MHz, $CDCl_3$, δ ppm): 1.36 (s, 6H), 2.56 (s, 2H), 6.02 (s, 2H), 7.52 (d, J=8.7 Hz, 2H), 8.37 (d, J=8.7 Hz, 2H); ^{13}C NMR (75 MHz, $CDCl_3$, δ ppm): 14.7, 121.9, 124.4, 129.7, 130.6, 138.4, 141.9, 142.5, 148.4, 156.7.

Synthesis of BODIPY 8-aminophenyl (5)

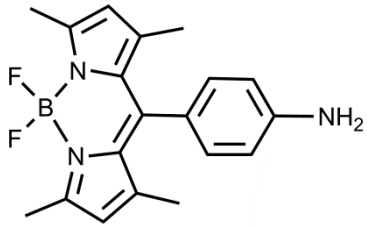

To a solution of BODIPY-Ph-NO_2 (1 eq.; 0.87 mmol; 0.320 g) in 35 mL ethanol was added 10 mg of palladium (5%) on carbon and hydrazine hydrate (5 eq.; 4.30 mmol; 0.210 mL). The mixture was refluxed for 2 h under inert atmosphere. The mixture was allowed to cool and the solids were filterd over a Millipore 0.45 µm filter. The organic layer was concentrated *in vacuo* yielding an orange solid (yield: 0.295 g, quantitative). ESI-MS (MeOH, m/z): calcd: 339.19 g/mol $[M+H]^+$, found: 1040.7 g/mol $[3M+Na]^+$. ^{1}H NMR (300 MHz, $CDCl_3$, δ ppm): 1.49 (s, 6H), 2.55 (s, 2H), 3.84 (broad, 2H), 5.97 (s, 2H), 6.76 (d, J=8.5 Hz, 2H), 7.26 (d, J=8.5 Hz, 2H); ^{13}C NMR (75 MHz, $CDCl_3$, δ ppm): 14.5, 14.6, 115.4, 120.9, 124.6, 128.9, 132.0, 142.7, 143.2, 147.1, 155.0.

Synthesis of BODIPY-Ph-NH-Acyl (6)

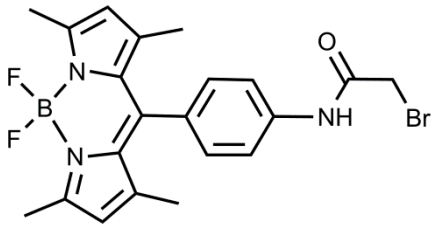

BODIPY-Ph-NH_2 **(5)** (1 eq.; 0.15 mmol; 50 mg) and triethylamine (1.5 eq.; 0.22 mmol, 22.8 mg) were dissolved in 20 mL dry DCM and cooled to 0 °C. Bromoacetyl bromide (1 eq.; 0.15 mmol; 30.3 mg) was added dropwise and the reaction was allowed to stir at 0 °C for 30 minutes and subsequently slowly heated to room temperature and left stirring overnight. The solution was washed with 2 M HCl (20 mL) and water (2x 20 mL). The organic layer was dried and evaporated till a dark red solid (yield: 0.049 g, 71%). EI-MS: calcd: 461.12 g/mol $[M+H]^+$, found: 459 g/mol $[M-H]^+$. ^{1}H NMR (300 MHz, $CDCl_3$, δ ppm): 1.35 (s, 6H), 2.48 (s, 4H), 3.99 (s, 2H), 5.91 (s, 2H), 7.20 (d, J=8.7 Hz, 2H), 7.63 (d, J=8.7 Hz, 2H), 8.20 (s, 1H); ^{13}C NMR (75 MHz, $CDCl_3$, δ ppm): 14.5, 16.6, 26.0, 119.0, 121.9, 124.0, 124.5, 131.5, 140.3, 147.1, 147.6, 154.4, 167.0.

Synthesis of BODIPY 8-chloromethane (7)

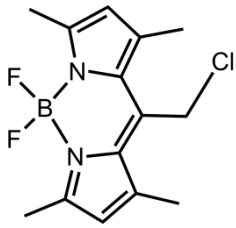

To a solution of 2,4-dimethylpyrrole (2 eq.; 4.86 mmol; 0.462 g) in 25 mL dry DCM was chloroacetyl chloride (1 eq.; 2.43 mmol; 0.193 mL) added dropwise at 0 °C. The solution was allowed to stir for 30 minutes at 0 °C and was then refluxed for 3 h. The solution was subsequently cooled to 0 °C and 40 mL of DCM was added. Triethylamine (10 eq.; 25.3 mmol; 3.53 mL) was added to the

solution. After 5 minutes of stirring at 0 °C, boron trifluoride diethyl etherate (11 eq.; 26.73 mmol; 3.30 mL) was slowly added and the solution was stirred at room temperature overnight. Diethyl ether (100 mL) was added to the solution and the organic layer was washed with water (3x 50 mL). The organic layer was dried with $MgSO_4$ and concentrated *in vacuo*. The resulting residue was purified using silica column (eluent: DCM/PET 1:1) yielding a red solid (yield: 0.441 g, 30%). CI-MS (MeOH, m/z): calcd: 297.55 g/mol $[M+H]^+$, found: 262 g/mol $[M-Cl]^+$. ^1H NMR (300 MHz, $CDCl_3$, δ ppm): 2.53 (s, 12H), 4.77 (s, 2H), 6.09 (s, 2H); ^{13}C NMR (75 MHz, $CDCl_3$, δ ppm): 14.7, 15.5, 37.1, 121.3, 131.4, 135.9, 141.1, 156.6.

Synthesis of BODIPY 8-bromomethane (8)

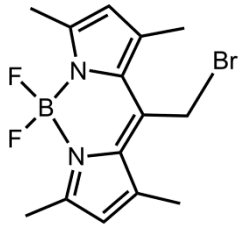

The synthesis is analogous to the synthesis of BODIPY 8-chloromethane. Yield a dark red solid (yield: 0.148 g, 9%). CI-MS (MeOH, m/z): calcd: 342.00 g/mol $[M+H]^+$, found: 261 g/mol $[M-Br]^+$. ^1H NMR (300 MHz, $CDCl_3$, δ ppm): 2.54 (s, 6H), 2.55 (s, 6H), 4.68 (s, 2H), 6.09 (s, 2H); ^{13}C NMR (75 MHz, $CDCl_3$, δ ppm): 14.7, 15.9, 24.5, 121.3, 131.0, 137.3, 140.9, 156.4.

Synthesis of BODIPY-Ph-N_3 (9)

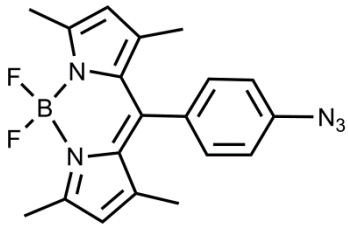

BODIPY-Ph-NH_2 **(5)** (1 eq.; 0.84 mmol; 0.285 g) was dissolved in 15 mL of 1.0 M HCl/MeOH, cooled to 0 °C and stirred for 10 minutes. $NaNO_2$ (2.5 eq.; 2.1 mmol; 0.145 mg) in 1.0 mL of water, was added over 5 minutes and the solution was stirred for 1 h at 0 °C. NaN_3 (5 eq.; 4.2 mmol; 0.273 g) was added and stirred for an additional hour at room temperature. The solvents were evaporated and the residue was redissolved in 25 mL ethyl acetate. The organic layer was washed with water (2x 20 mL) and brine (20 mL). The organic layer was and dried over $MgSO_4$ and evaporated. The product was purified *via* column chromatography (Heptane:EtOAc 7:3) as an orange solid (yield: 0.151 g, 49%). ^{1}H NMR (300 MHz, $CDCl_3$, δ ppm): 1.41 (s, 6H), 2.54 (s, 6H), 5.98 (s, 2H), 7.13 (d, J=8.36 Hz, 2H), 7.26 (d, J=8.36 Hz, 2H); ^{13}C NMR (75 MHz, $CDCl_3$, δ ppm): 14.6, 119.8, 121.4, 129.7, 131.6, 140.6, 141.1, 145.9, 155.8.

Synthesis of BODIPY-$(CH_2)_3$-Cl (10)

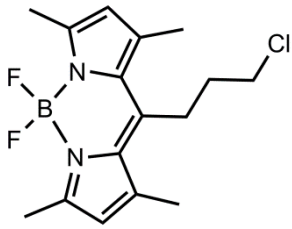

To a solution of 4-chlorobutyryl chloride (1 eq.; 5.0 mmol; 0.56 mL) in 25 mL dry DCM was added 2,4-dimethylpyrrole (2 eq.; 10 mmol; 1.04 mL). The solution was allowed to stir for 30 minutes at room temperature while the solution turned dark red. The solution was subsequently refluxed for 4 h. The solution was then cooled to 0 °C and triethylamine (10 eq.; 50 mmol; 6.94 mL) was added. After 5

minutes of stirring at 0 °C boron trifluoride diethyl etherate (11 eq.; 55 mmol; 7.56 mL) was slowly added and the solution was stirred at room temperature overnight. Diethyl ether (200 mL) was added to the solution and the organic layer was washed with water (3x 75 mL). The organic layer was dried with $MgSO_4$ and concentrated *in vacuo*. The resulting residue was purified using silica column (eluent: DCM/PET 1:1) yielding a red solid (yield: 0.345 g, 21%). ESI-MS (MeOH, m/z): calcd: 325.60 g/mol $[M+H]^+$, found: 349.8 g/mol $[M+Na]^+$. ^{1}H NMR (300 MHz, $CDCl_3$, δ ppm): 2.05 (m, 2H), 2.41 (s, 6H), 2.51 (s, 6H), 3.10 (m, 2H), 3.68 (t, 2H), 6.05 (s, 2H); ^{13}C NMR (75 MHz, $CDCl_3$, δ ppm): 14.5, 16.5, 25.9, 34.0, 44.7, 121.9, 131.4, 140.4, 144.4, 154.3.

Synthesis of BODIPY-$(CH_2)_3$-N_3 (11)

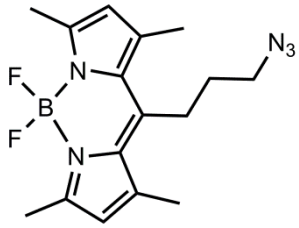

To a solution of BODIPY-$(CH_2)_3$-Cl **(10)** (1 eq.; 1.76 mmol; 0.570 g) in DMF (36 mL) was sodium azide (2 eq.; 3.51 mmol; 0.228 g) added and stirred for 36 h at 40 °C. The reaction was cooled to room temperature and 30 mL of water was added. The mixture was extracted with ethyl acetate (3x 20 mL), the organic layer was washed with water (20 mL), brine (20 mL) and dried with $MgSO_4$. The solvent was evaporated *in vacuo* and the resulting residu was purified via column chromatography (Heptane:EtOAc 7:3) as an orange solid (yield: 0.345 g, 59%). IR (neat): $\tilde{\nu}$ = 2102 cm^{-1} (azide). ^{1}H NMR (300 MHz, $CDCl_3$, δ ppm): 1.87 (m, 2H), 2.43 (s, 6H), 2.52 (s, 6H), 3.04 (m, 2H), 3.49 (t, 2H), 6.06 (s, 2H); ^{13}C NMR (75 MHz, $CDCl_3$, δ ppm): 14.5, 16.4, 25.6, 31.1, 51.5, 121.9, 131.4, 140.3, 144.6, 154.3.

Synthesis of La-DOTA-BDP4 (12)

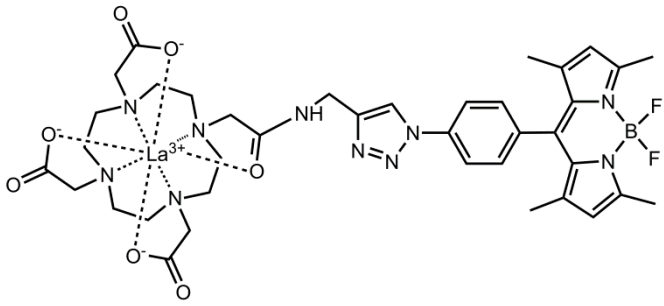

BODIPY-Ph-N_3 **(9)** (1 eq.; 0.03 mmol; 10 mg) and propargylated La-DOTA (1 eq.; 0.03 mmol; 16 mg) were dissolved in 3 mL of a 10:3:3 MeOH/DCM/H_2O mixture. Cu(II)SO_4 (10 mol%) and sodium ascorbate (20 mol%) were added as 0.1 M solutions in water. Three drops of triethylamine are added and the solutions are stirred for 24 h in the dark. The solvents were evaporated and the compound is purified *via* HPLC. ESI-MS (MeOH, m/z): calcd: 941.55 g/mol $[M-H]^-$, found: 941.2 g/mol $[M-H]^-$. Yield: 2 mg, 5%.

Synthesis of La-DOTA-BDP5 (13)

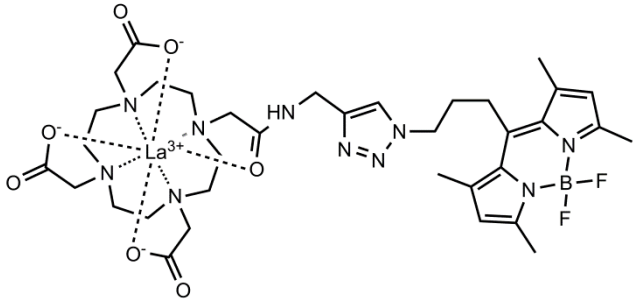

BODIPY-$(CH_2)_3$-Cl **(10)** (1 eq.; 0.1 mmol; 33 mg) and propargylated La-DOTA (1 eq.; 0.1 mmol; 58 mg) was dissolved in 6 mL of a 10:3:3 MeOH/DCM/H_2O mixture. Cu(II)SO_4 (10 mol%) and sodium ascorbate (20 mol%) were added as 0.1 M solutions in water. Three drops of triethylamine are added and the solutions are stirred for 24 h in the dark. The solvents were evaporated and the compound is purified *via* HPLC. ESI-MS (MeOH, m/z): calcd: 909.53 g/mol $[M+H]^+$, found: 909.3 g/mol $[M+H]^+$. Yield: 5 mg, 6%.

NMR: ^{1}H NMR (300 MHz, $CDCl_3$, δ ppm): 0.98-3.81 (broad, 40H); 4.31 (broad, 4H), 5.99 (s, 2H), 7.77 (s, 1H).

HPLC trace La-DOTA-BDP4:

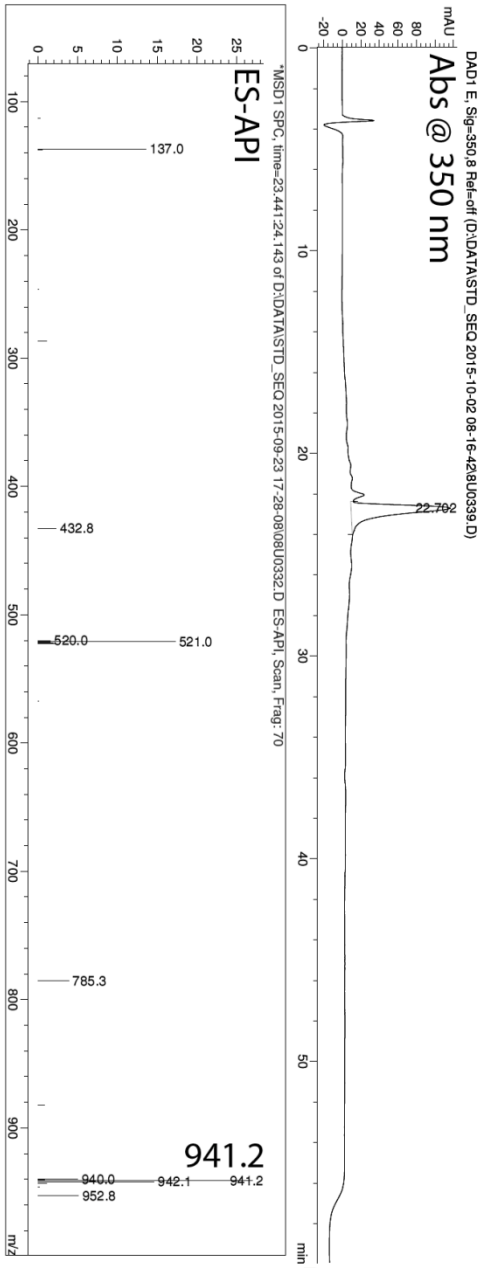

HPLC trace La-DOTA-BDP5:

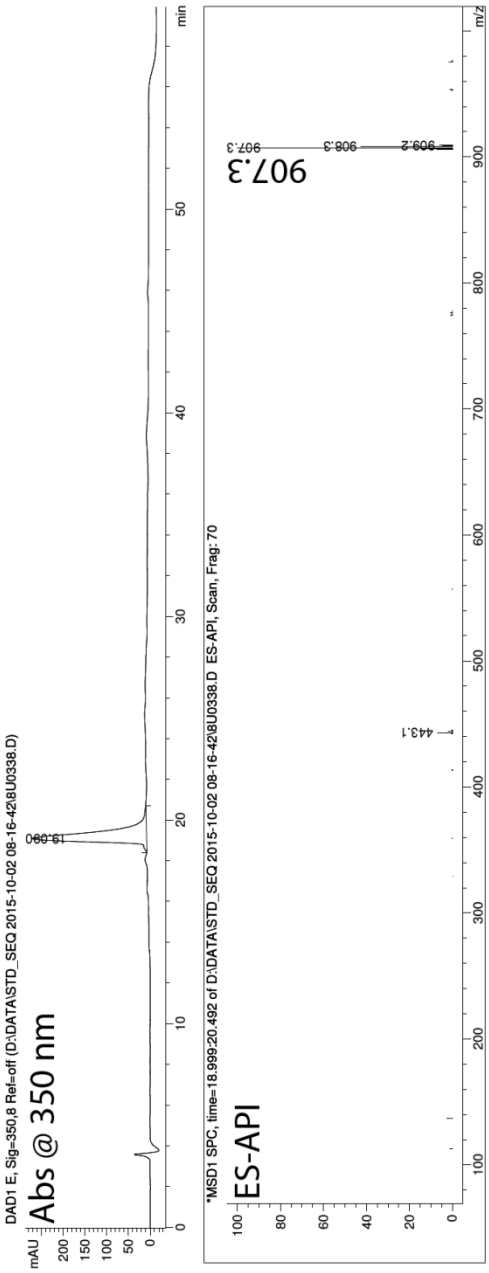

5 References

(1) Hermann, P.; Kotek, J.; Kubíček, V.; Lukeš, I. *Dalt. Trans.* **2008**, *9226* (23), 3027.

(2) Pierre, V. C.; Allen, M. J.; Caravan, P. *J. Biol. Inorg. Chem.* **2014**, *19* (2), 127–131.

(3) Waters, E. A.; Wickline, S. A. *Basic Res. Cardiol.* **2008**, *103* (2), 114–121.

(4) Tóth, É.; Helm, L.; Merbach, A. In *Contrast Agents I*; Krause, W., Ed.; Topics in Current Chemistry; Springer Berlin Heidelberg: Berlin, Heidelberg, 2002; Vol. 221, pp 61–101.

(5) Debroye, E.; Parac-Vogt, T. N. *Chem. Soc. Rev.* **2014**, *43* (23), 8178–8192.

(6) Cacheris, W. P.; Quay, S. C.; Rocklage, S. M. *Magn. Reson. Imaging* **1990**, *8* (4), 467–481.

(7) Accardo, A.; Tesauro, D.; Aloj, L.; Pedone, C.; Morelli, G. *Coord. Chem. Rev.* **2009**, *253* (17-18), 2193–2213.

(8) Caravan, P.; Ellison, J. J.; McMurry, T. J.; Lauffer, R. B. *Chem. Rev.* **1999**, *99* (9), 2293–2352.

(9) L. Villaraza, A. J.; Bumb, A.; Brechbiel, M. W. *Chem. Rev.* **2010**, *110* (5), 2921–2959.

(10) Joshi, B. P.; Wang, T. D. *Cancers* **2010**, *2* (2), 1251–1288.

(11) Ulrich, G.; Ziessel, R.; Harriman, A. *Angew. Chemie Int. Ed.* **2008**, *47* (7), 1184–1201.

(12) Loudet, A.; Burgess, K. *Chem. Rev.* **2007**, *107* (11), 4891–4932.

(13) Bernhard, C.; Goze, C.; Rousselin, Y.; Denat, F. *Chem. Commun.* **2010**, *46* (43), 8267.

(14) Duimstra, J. A.; Femia, F. J.; Meade, T. J. *J. Am. Chem. Soc.* **2005**, *127* (37), 12847–12855.

(15) Toronto Research Chemicals Inc. Chemical Specification of Bodipy 8-Chloromethane http://www.trc-canada.com/detail.php?CatNum=B674700&CAS=208462-25-3&Chemical_Name=Bodipy 8-Chloromethane&Synonym=(T-4)-[2-[2-Chloro-1-(3,5-dimethyl-2H-pyrrol-2-ylidene-?N)ethyl]-3,5-dimethyl-1H-pyrrol ato-?N]difluoro-boron; (accessed Oct 26, 2015).

(16) Jose, J.; Ueno, Y.; Castro, J. C.; Li, L.; Burgess, K. *Tetrahedron Lett.* **2009**, *50* (47), 6442–6445.

(17) Kamkaew, A.; Burgess, K. *J. Med. Chem.* **2013**, *56* (19), 7608–7614.

(18) Olmsted, J. *J. Phys. Chem.* **1979**, *83* (20), 2581–2584.

(19) Laurent, S.; Vander Elst, L.; Muller, R. N. *Contrast Media Mol. Imaging* **2006**, *1* (3), 128–137.

GENERAL CONCLUSIONS & FUTURE OUTLOOK

Four different potential bimodal contrast agents for optical and magnetic resonance imaging have been synthesized and thoroughly investigated. All are different in their design, synthetic approach, and properties.

The first approach is based on metallostar complexes based on dipicolinic acid (DPA) and diethylene triamine pentaacetic acid (DTPA) to produce potential T_1 contrast agents. In these bitopic ligands, two different lanthanides are incorporated. The Gd-DTPA is coupled *via* an amide bond to the DPA moiety, which self-assembles around a luminescent lanthanide. The three types of metallostars differ by the linkage of the phenyl group of the DPA moiety. The luminescent properties of the complexes diverge strongly over the different ligands. For europium(III), terbium(III) and dysprosium(III) characteristic emission could be recorded, but the quantum yield changed greatly depending on the ligand. For example, GdL^1 showed much better luminescent quantum yields for all studied complexes, while GdL^2 was able to sensitize ytterbium(III) in solid state samples. The NMRD measurements of the complexes showed an increase in longitudinal relaxivity values r_1 in comparison to Gd-DTPA. For example the $(GdL^2)_3Ln$ complexes (Ln = Eu(III), Dy(III), Tb(III)) showed values of 24.27, 22.80 and 21.72 $s^{-1}mM^{-1}$ respectively per metallostar complex at 310 K and 20 MHz.

In a second approach small monodisperse multimodal iron oxide nanoparticles were functionalized with three novel boron-dipyrromethene (BODIPY) derivatives as potential T_2/T_2* contrast agents. The dyes are covalently attached onto the nanoparticles surface *via* thiolene click chemistry, after which bright fluorescence is observed for these nanoparticles. Relaxivity studies on agar

phantoms showed an r_2 value of 49 ± 3 and 47 ± 7 $s^{-1}mM^{-1}$ for NP-BDP1 and NP-BDP3 respectively. Cell viability studies showed no significant cytotoxicity at any of the tested concentrations on rat tumor (AR42J) and human ovarian cancer (SKOV3) cells. Human hepatic stellate (GRX) cells were only significantly affected by the NPs at the highest concentrations.

In a third approach another type of potential T_1 contrast agents are developed and investigated. The synthetic approach uses azide diazotransfer chemistry in a copper tube flow reactor, where the formed azide is coupled directly with a Gd-DOTA moiety via copper mediated cycloaddition forming a novel Gd-DOTA complex functionalized with a BODIPY dye. The paramagnetic gadolinium(III) chelate will act as a T_1 contrast agent. This BODIPY dye is a small organic molecule which functions as the optical probe and emits at 523 nm with a high quantum yield. The emission wavelength of the dye should be adjusted by altering the resonance structure of the core so it falls within the optical window. The proton relaxivity of the complex shows a potential use as a bimodal contrast agent for optical and MRI. A lanthanide(III) analogue has been synthesized and the NMR spectrum is fully analyzed.

At first peptide chemistry was used in a fourth approach to synthesize a novel protected DOTA-BODIPY derivative. Unfortunately, the BODIPY core was destroyed during deprotection and a final complex could not be obtained. Azide containing BODIPY derivatives are reproduced from literature and are combined with lanthanum(III)-DOTA chelates *via* a copper mediated cycloaddition reaction. The resulting complexes are water-soluble and exhibit good fluorescent properties. Fairly high quantum yields of 39% and 64% are obtained for La-DOTA-BDP4 and La-DOTA-BDP5 respectively. The emission wavelength of the dye should be adjusted so it falls within the optical window. Gadolinium(III) containing derivatives should also be synthesized to measure the relaxometric properties. Due to the similar size and internal rotation, it is expected that the relaxivity of these compounds will be in the range of previously reported values for Gd(III)-DOTA complexes.

As a general conclusion, the above described chemical compounds exhibited favorable physicochemical properties to act as potential multimodal contrast agents for optical and magnetic resonance imaging. The rotational correlation time has effectively been increased because of the rigid structure and high molecular mass, thus the metallostar complexes gave the best longitudinal relaxivity (r_1). The optical results are promising, as the emission wavelength of terbium(III) and europium(III) are close to the optical window, but suffer from relatively low quantum yields. The opposite is true for compounds containing BODIPY dyes. Very high fluorescent quantum yields can be obtained, but modest values of r_1 which are comparable to clinically used contrast agents, have been obtained.

These designed structures have interesting characteristics and should be tested in cells and/or mice for biocompatibility studies. To circumvent the equilibrium between the bis and tris form of the metallostar complexes, the dipicolinate moieties could be joined together in a macrocyclic ring. The stability constant and the quantum yield of the central ion will be higher. Other chelating derivatives, such as coumarin, could be considered to form metallostar complexes. Coumarin derivatives generally absorb at higher wavelengths which would be better for *in vivo* use.

The iron oxide nanoparticles show good transverse relaxivity and optical properties. Both IO-BDP1 and IO-BDP2 discussed in chapter 4 will have a minimal use in medical imaging as the emission wavelength is to low or the particles are not water dispersible. IO-BDP2 shows to be potentially useful for applications such as in polymer blends or thin film production. IO-BDP3 would be a valuable candidate for medical imaging use, as the emission wavelength is in the optical window and exhibits low cellular toxicity. Further studies could involve *in vivo* experiments to study the biocompatibility. Increasing the stability in solution of nanoparticles by adding longer ethylene glycol chains could be considered. Another interesting approach is the development of bimodal targeted contrast agents by introducing RGD mimetic, folic acid or antibodies to the surface of the nanoparticles. Possible photodynamic therapy could be obtained by an addition of

iodine containing BODIPY derivatives to the surface of the iron oxide nanoparticle. Or a mixture of different emissive BODIPY dyes can also be grafted to the surface which would lead to a MRI and a dual optical imaging probe.
The relaxivity of the Gd-DOTA containing BODIPY dyes should be improved. In a first approach a rigid system should be made to limit the internal motion of the Gd-DOTA moiety. In a second approach to decrease the rotational correlation time, interactions with macromolecules such as human serum albumin can be considered. In previous studies it was shown that a small apolar group can reversible interact with proteins in the bloodstream, increasing the relaxivity of the complex. RGD mimetic molecules can be incorporated to selectively target cells and increase the relaxivity. Multi-component reactions, such as the Ugi reaction, could be considered to easily prepare such complex structures.

The development of new bimodal contrast agents was always considered for the reported compounds, but they could also be a platform for other scientists from different fields such as, biology, engineering, and medicine, in their search for new applications.

SAFETY ASPECTS

All lab experiments were performed in compliance with the Code of practice for Safety in the Lab (KU Leuven) and the Introductory Safety Brochure (Department of Chemistry). Risk assessments were drafted for all experiments. The approved risk assessments are stored on the departmental Risk assessment website. All lab experiments were conducted using the appropriate safety measures such as: lab coat, safety glasses and gloves.

Extra care was taken when working with E4 products such as diethyl ether, dimethylformamide, and methanol or potential carcinogenic materials. Azides are a highly reactive commonly used in both chemical synthesis and biomedical research applications. Azides (inorganic and organic) possess toxic properties and can be potentially explosive and shock sensitive under certain conditions. Therefore, azides require precaution during preparation, storage, handling and disposal. Never add NaN_3 to acidic wastes or small halogenated molecules, as this can produce highly toxic and explosive products. Waste collection was done in the provided waste containers. Since the effects of nanoparticles with the human skin or internal metabolism are not completely understood, extra care was taken when manipulating these products. Waste was collected separately in plastic bags before general disposal. Nanoparticles were always stored as colloidal suspensions in closed vessels.

CONFERENCES

ChemCYS (Blankenberge, Belgium)

Poster presentation Mar 2012

Synthesis of luminescent MRI contrast agents based on pyridine-2,6-dicarboxylic acid

Finelumen (Eindhoven, The Netherlands)

Poster presentation Sept 2012

Gd-DTPA derivatives of BODIPY dyes as potential Bimodal MRI contrast agents

YBMRS-11 (Spa, Belgium)

Poster presentation Nov 2012

BODIPY dye derivatives of Gd-DTPA as potential Bimodal MRI contrast agents

YBMRS-12 (Blankenberge, Belgium)

Poster presentation Nov 2013

Gd-DOTA derivatives of BODIPY dyes as potential bimodal MRI contrast agents

YBMRS-13 (Spa, Belgium)

Poster presentation Nov 2014

Gd-DOTA derivatives of BODIPY dyes as potential bimodal MRI contrast agents

PUBLICATIONS

1. **Ceulemans, M.**, Bloemen, M., Verstraete, C., Manshian, B., Himmelreich, U., Verbiest, T., De Borggraeve, W.M., Parac-Vogt, T.N. (2015), Luminescent and Relaxometric Properties of Bodipy derivatives covalently bond to iron oxide nanoparticles as potential bimodal contrast agents. (Submitted)

2. **Ceulemans, M.**; Nuyts, K.; De Borggraeve, W. M.; Parac-Vogt, T. N. (2015), Gadolinium(III)-DOTA complex functionalized with BODIPY as a potential bimodal contrast agent for MRI and optical imaging. *Inorganics*, 3(4), 516-533.

3. **Ceulemans, M.**; Debroye, E.; Vander Elst, L.; De Borggraeve, W. M.; Parac-Vogt, T. N. (2015), Luminescence and Relaxometric Properties of Heteropolymetallic Metallostar Complexes with Selectively Incorporated Lanthanide(III) Ions. *European Journal of Inorganic Chemistry*, 2015(25), 4207–4216.

4. Nuyts, K.; **Ceulemans, M.**; Parac-Vogt, T. N.; Bultynck, G.; De Borggraeve, W. M. (2015), Facile azide formation via diazotransfer reaction in a copper tube flow reactor. *Tetrahedron Letters*, 56(13), 1687–1690.

5. Bloemen, M.; Vanpraet, L.; **Ceulemans, M.**; Parac-Vogt, T. N.; Clays, K.; Geukens, N.; Gils, A.; Verbiest, T. (2015), Selective protein purification by PEG-IDA-functionalized iron oxide nanoparticles. *RSC Advances*, *5*(82), 66549–66553.

6. Debroye, E.; **Ceulemans, M.**; Vander Elst, L.; Laurent, S.; Muller, R. N.; Parac-Vogt, T. N. (2014), Controlled Synthesis of a Novel Heteropolymetallic Complex with Selectively Incorporated Lanthanide(III) Ions. *Inorganic. Chemistry*, 53(13), 1257–1259.

APPENDIX

Materials Instrumentation and Procedures

1 Materials, Reagents and solvents.

Materials, Reagents and solvents were obtained from Acros Organics (Geel, Belgium), ABCR (Karlsruhe, Germany), Alfa Aesar (Ward Hill, USA), BDH Prolabo (Leuven, Belgium), ChemLab (Zedelgem, Belgium), Fisher Scientific (Loughborough, UK), Iris Biotech GmbH (Marktredwitz, Germany), Polysciences, Inc. (Eppelheim, Germany), Sigma-Aldrich (Bornem, Belgium), VWR chemicals (Leuven, Belgium), and were used without further purification.

2 FT-IR spectroscopy

FT-IR spectra were measured by using a Bruker Vertex 70 FT-IR spectrometer (Bruker, Ettlingen, Germany) equipped with a Platinum ATR accessory. Data was processed with OPUS 6.5 software.

3 Mass spectrometry

Electrospray ionisation mass spectroscopy (ESI-MS) was conducted on a Thermo Electron LCQ Advantage mass spectrometer with an ion trap analyzer, an Agilent 1100 HPLC injection system and the Xcalibur data processing software. LC-MS was performed on an Alltech Prevail RP-C18 5 µm 150 mm x 2,1 mm column

coupled to an Agilent 1100 degasser, quaternary pump, auto sampler, UV-DAD detector and thermostated column module coupled to Agilent 6110 single-quadrupole MS. Use of Agilent LC/MSD Chemstation software.

4 HPLC

Preparative HPLC was performed on a Waters Delta 600 system equipped with a Waters 996 Photo Diode Array detector. An Alltech C18 Prevail (5 µm, 150 mm x 22 mm) was employed.

5 NMR spectroscopy

^{1}H and ^{13}C NMR spectra were recorded by using a Bruker Avance 300 spectrometer, operating at 300 MHz for ^{1}H and 75 MHz for ^{13}C, a Bruker Avance 400 spectrometer, operating at 400 MHz for ^{1}H and 100 MHz for ^{13}C, or a Bruker Avance III 600 spectrometer, operating at 600 MHz for ^{1}H and 150 MHz for ^{13}C (Bruker, Karlsruhe, Germany). Chemical shifts are reported in parts per million (ppm) and are referenced to the internal standard tetramethylsilane. For ^{13}C spectra, residual solvent signals are used as the internal standard. Spectra are taken at room temperature unless otherwise stated.

6 Proton NMRD

Proton nuclear magnetic relaxation dispersion (NMRD) profiles were measured on a Stelar Spinmaster FFC, fast field cycling NMR relaxometer (Stelar, Mede (PV), Italy) over a magnetic field strength range extending from 0.24 mT to 0.7 T. Measurements were performed at 310 K on 0.6 mL samples contained in 10 mm o.d. pyrex tubes. Additional relaxation rates at 20, 60, 300 and 500 MHz were respectively obtained on a Minispec mq-20, a Minispec mq-60, a Bruker Avance-300 and a Bruker Avance 500 (Bruker, Karlsruhe, Germany).

7 TXRF spectrometry

TXRF measurements were performed on a Bruker S2 Picofox (Bruker, Berlin, Germany) with a molybdenum source and a Bruker AXS sample carrier. 100 µm sample solutions were added to 100 µl of a Chem-Lab gallium(III) standard solution (500 µg/mL, 2-5% HNO_3). The resulting solution was drop casted on a hydrophobic quartz plate and dried in an oven at 60 °C to remove the solvent. Three quartz plates were made in the same manner and used to determine the concentrations.

8 Magnetic Resonance Imaging

Phantoms of NPs suspended in Eppendorf tubes containing 1.5% agar gel (microbiology grade, Sigma Aldrich, Bornem, Belgium) were prepared as previously reported.[1,2] Hereby, total iron concentrations in the phantoms varied between 0 to 300 $\mu g \cdot ml^{-1}$. Similarly, phantoms were prepared containing SKOV3 cells that were previously incubated overnight with NPs (50 g iron/ ml medium).[2]

MRI experiments of phantoms were performed as previously described.[1,2] Briefly, a Bruker Biospec 9.4 T small animal MR scanner (Bruker Biospin, Ettlingen, Germany, horizontal bore, 20 cm) equipped with actively shielded gradients (600 $mT \cdot m^{-1}$) was used for all experiments. A quadrature radio-frequency transmit/receive resonator (inner diameter 7 cm, Bruker Biospin) was used for data acquisition. Measurements of the T_2 relaxation times were performed using a multi-echo, spinecho pulse sequence with 24 echo time (TE) increments (first TE = 11 ms, increments of 11 ms; repetition time (TR) = 1500 ms, slice thickness 1 mm, in-plane resolution 117 µm). Measurements of the T_1 relaxation times were performed using a variable TR spin echo sequence with TE = 10 ms, 10 increments of TR ranging from 155 to 5000 ms, slice thickness 1 mm, in-plane resolution 117 µm). Three-dimensional, high-resolution T2*-weighted MR images were acquired from phantoms containing cell suspensions and using a gradient echo sequence (FLASH, TR = 200 ms, TE = 15 ms, 15 excitation pulse of 15°). The field of view was 6.0 × 6.0 × 2 cm, resulting in an isotropic resolution of 117

μm^3. All images were processed with Paravision 5.1 (Bruker Biospin, Ettlingen, Germany).

9 Optical spectroscopy

UV-Vis absorption spectra were measured on a Varian Cary 5000 spectrophotometer on freshly prepared aqua solutions in quartz Suprasil® cells (115F-QS) with an optical path-length of 1.0 cm.

Emission data were recorded on an Edinburgh Instruments FLS980 steady-state spectrofluorimeter. With a continuous xenon lamp (Xe1) and a standard PMT (Hamamatsu type R928P). It is equipped with a double grating monochromator and an automatic filter wheel to remove 2nd order effects. Luminescence decays, excitation, and emission data were recorded on an Edinburgh Instruments FS900 or FS920 steady state spectrofluorimeter. These instruments are equipped with a 450 W xenon arc lamp, a high energy microsecond flash lamp μF900H and an extended red-sensitive photomultiplier (185–1010 nm, Hamamatsu R 2658P). All spectra are corrected for the instrumental functions. Luminescence decays were determined under ligand excitation monitoring emission of the most intense transitions of the luminescent lanthanide. Luminescence decays were analyzed using Edinburgh software and lifetimes were averages of at least three measurements in water and deuterated water. Quantum yields were determined by a comparative method with an estimated experimental error of ± 10% using a solution Rhodamine 101 (Sigma) in ethanol (Q = 100%) and Rhodamine 6G (Q = 76%) in water as standards. The solutions are diluted to get an optical density lower than 0.05 at the excitation wavelength.

The two-photon fluorescence microscopy samples were prepared by drop casting the functionalized nanoparticles in water on microscopy slides, after which the samples were allowed to dry for several hours. Two-photon microscopy experiments were conducted on a commercial Olympus BX61WI-FV1200-M system (Olympus, Münster, Germany). The fundamental wavelength was set to 1100 nm (120 fs pulse width, 80 MHz pulse repetition rate) on the InSight DS+

laser of Spectra Physics. The polarization of the fundamental beam was controlled using a Glan-laser polarizer. For detection at 550 nm, a 560 lpxr dichroic mirror of Chroma was installed in front of the detector. Detection was carried out non-descanned in backward reflection using a photon counter detector of Hamamatsu R3896 (Hamamatsu Photonics Co., Hamamatsu, Japan). The images (640 × 640 pixels) were recorded with a 15× Thorlabs LMV objective (NA of 0.3) and a pixel dwell time of 200 ms.

10 High content image analysis of cell viability

The NPs were tested for cellular interaction and their effect on cellular viability in five primary and immortalized, carcinoma and normal mammalian and rat cell types. These were: the human umbilical vein endothelial (HUVEC), human hepatic stellate (GRX), human ovarian carcinoma (SKOV3), rat exocrine pancreatic tumor (AR42J) and rat insulinoma (INS1) cells. Cells were seeded in 96 well plates at a concentration of 3500 cells per well in 250 µl full cell medium and allowed to settle overnight in a humidified (5% CO_2) incubator set at 37 °C. Next day, each cell type was exposed to the NPs at 0, 5, 10, 25, 50, 100, and 200 µg/ml concentrations in triplicate for 24 h. Following the exposure period the cells were washed twice with phosphate buffered saline (PBS; Gibco, Invitrogen, Belgium) and treated with 2 µM fixable Live-Dead green (Molecular Probes, Life Technologies Europe, BV, Belgium) dead cell stain in 250 µl full cell medium/well for 30 min at 37 °C. The stain was removed by washing once with PBS and fresh medium was added to each well (250 µl/well) and incubated for further 30 min at 37 °C in a 5% CO_2. Finally, cells were fixed with 4% paraformaldehyde for 10 min at room temperature. The fixative was removed and cells were washed once with PBS. The nuclei were counterstained with Hoechst 33342 solution (Life Technologies Europe, BV, Belgium) after which cells were washed twice with PBS and each well was aliquoted with 500 µl of PBS. Plates were analyzed on the InCell analyser2000 (GE Healthcare Life Sciences, Belgium) where fluorescence-based images for the blue (nucleus), green (dead cells) and red (NPs) channels were collected at a minimum of 2000 cells per

replicate. Acquired data was analyzed using the InCell Developer software (GE Healthcare Life Sciences, Belgium).

11 Flow setup

The flow setup was constructed with copper GC tubing (0,065" inner diameter, Restek) and the reagents are pumped using a Chemyx Fusion 200 syringe pump.

12 Determination of q

Luminescence decays of the metallostar complexes have been measured in water and D_2O under ligand excitation (270-315 nm). The transitions $^5D_0 \rightarrow {}^7F_2$, $^5D_4 \rightarrow {}^7F_5$ and $^4F_{9/2} \rightarrow {}^6H_{13/2}$ of Eu(III), Tb(III) and Dy(III) respectively, were monitored and analyzed using the Edinburgh software and lifetimes were averages of at least three measurements. The decrease of the luminescence lifetime in water compared to D_2O is due to the presence of inner sphere high-energy O-H vibrations and can be used for determining the number of coordinated water molecules. The best fit was observed by applying a bi-exponential decay, which suggests the presence of two different species in solution. The following phenomenological equation[3–6] for Ln(III)-polyaminocarboxylate systems have been employed to determine the hydration number q with an accuracy of ± 0.1-0.3:

$$q_{\mathrm{Eu\,(H_2O)}} = 1.11(\Delta k_{obs} - 0.31 + 0.44q^{OH} + 0.99q^{NH} + 0.075q^{CONH}) \quad \text{(eq. 1)}$$

$$q_{\mathrm{Dy\,(H_2O)}} = 21.1 \cdot \Delta k_{obs} - 0.60 \quad \text{(eq. 2)}$$

$$q_{\mathrm{Tb\,(H_2O)}} = 5(\Delta k_{obs} - 0.06) \quad \text{(eq. 3)}$$

Δk_{obs} represents the difference of the decay rate constants $k_{H_2O}(1/\tau_{H_2O})$ and $k_{D_2O}(1/\tau_{D_2O})$, expressed in ms^{-1} for Eu(III) and Tb(III) and μs^{-1} for Dy(III). The q^X, stands for the number of OH, NH or CONH groups directly bound to the lanthanide center.

13 Quantum yield

The luminescent quantum yields Q_L^{Ln} were determined upon ligand excitation by a comparative method, using a solution of Rhodamine 101 in ethanol (Q = 100%) or Rhodamine 6G in water (Q = 78%)[7] as the standard. Solutions were prepared in order to obtain an optical density in the range of 0.02-0.05 at the excitation wavelength. The quantum yield was determined according to the following equation:

$$Q_L = Q_S \cdot \frac{I_X}{I_S} \cdot \frac{A_S(\lambda_{exc})}{A_X(\lambda_{exc})} \cdot \frac{\eta_X^2}{\eta_S^2} \qquad \text{(eq. 4)}$$

In this equation, the s and x refer to the standard and the unknown sample respectively, I represents the corrected total integrated emission intensity, A is the absorbance at the excitation wavelength and η the refractive index of the solution (η_{water} = 1.34 and $\eta_{ethanol}$ = 1.36). Direct excitation into the lanthanides is possible but is very inefficient because the *f-f* transitions are Laporte forbidden. The intrinsic quantum yields Q_{Ln}^{Ln} (Ln = Eu(III), Tb(III)) can however be estimated according to the following equations comprising the ratio between the observed (τ_{obs}) and radiative (τ_{rad}) lifetimes.

$$\frac{1}{\tau_{rad}} = A_{MD,0} \cdot n^3 \cdot \left(\frac{I_{tot}}{I_{MD}}\right) \qquad \text{(eq. 5)}$$

$$Q_{Ln}^{Ln} = \frac{\tau_{obs}}{\tau_{rad}} \qquad \text{(eq. 6)}$$

The Einstein coefficient $A_{MD,0}$ equals 14.65 s^{-1}, n is the refractive index set to $n_{H_2O} = 1.34$, which is equal to that of the neat solvent, and (I_{tot}/I_{MD}) represents the ratio of the total integrated intensity of the transitions to the transition of the magnetic dipole (MD). Sensitization efficiency of europium complexes (η_{sens}) gives an idea about the efficiency of energy transfer from the ligand to the lanthanide ion and is defined by the ratio between the quantum yield under ligand excitation and the intrinsic quantum yield:

$$\eta_{sens} = \frac{Q_L^{Eu}}{Q_{Eu}^{Eu}} \quad \text{(eq. 7)}$$

14 References

(1) Atre-Ketkar, A.; Struys, T.; Soenen, S. J.; Lambrichts, I.; Verfaillie, C.; De Cuyper, M.; Himmelreich, U. *Int. J. Nanomedicine* **2013**, *8* (1), 4577.

(2) Trekker, J.; Leten, C.; Struys, T.; Lazenka, V. V.; Argibay, B.; Micholt, L.; Lambrichts, I.; Van Roy, W.; Lagae, L.; Himmelreich, U. *Biomaterials* **2014**, *35* (5), 1627–1635.

(3) Beeby, A.; Clarkson, I. M.; Dickins, R. S.; Faulkner, S.; Parker, D.; Royle, L.; de Sousa, A. S.; Williams, J. A. G.; Woods, M. *J. Chem. Soc. Perkin Trans. 2* **1999**, No. 3, 493–504.

(4) Supkowski, R. M.; Horrocks, W. D. *Inorganica Chim. Acta* **2002**, *340*, 44–48.

(5) Kimura, T.; Kato, Y. *J. Alloys Compd.* **1998**, *275-277*, 806–810.

(6) Horrocks, W. D.; Sudnick, D. R. *J. Am. Chem. Soc.* **1979**, *101* (2), 334–340.

(7) Olmsted, J. *J. Phys. Chem.* **1979**, *83* (20), 2581–2584.